Understanding and Controlling the Degradation of Nickel-rich Lithium-ion Layered Cathodes

James David Steiner

Thesis submitted to the faculty of the Virginia Polytechnic Institute and State University in partial fulfillment of the requirements for the degree of

Master of Science
In
Chemistry

Feng Lin, Chair
Amanda J. Morris
Zheng Li

September 4, 2018
Blacksburg, VA

Keywords: Nickel-rich, surface chemistry, layered oxide cathode, titanium, doping, phase transformation,

Understanding and Controlling the Degradation and Stabilization of Nickel-rich Lithium-ion Layered Cathodes

James David Steiner

ABSTRACT (Academic)

Consumers use batteries daily, and the lithium-ion battery has undergone a lot of engineering advances in the last few decades. There is a need to understand and improve the cathode chemistry to adapt to the rapidly growing electronics and electric vehicle market that is continually demanding more energy from batteries. Nickel-rich layered $LiNi_{1-x-y}Mn_xCo_yO_2$ ($1-x-y \geq 0.6$, NMC) cathodes could potentially provide the necessary energy to meet the demand of the high energy applications.

Overcoming the stability issues from oxygen activation in nickel-rich materials is one of the largest challenges facing the commercial incorporation of NMCs. This thesis focuses on, $LiNi_{0.8}Mn_{0.1}Co_{0.1}$ (NMC811). Using surface sensitive techniques, such as X-ray Absorption (XAS), our research reveals that degradation of NMC811 occurs during cycling, regardless of temperature, and that oxygen activation plays a role in the overall surface changes and degradation observed in NMC811. The thesis then explores the role of substituting a transition metal in the NMC811.

Then we used a gradient addition of titanium to the NMC811 material to stabilize the battery performance. Theoretical techniques, such as Finite Difference Method Near Edge Structure, and experimental techniques, such as XAS, revealed how transition metal substitution, specifically titanium, stabilized the lattice. The results indicated that titanium deactivates oxygen by limiting the nickel and oxygen covalency that typically

leads to oxygen activation upon charging. We observed that the titanium substitution increases cycling reversibility after hundreds of cycles.

Overall, the work indicates that a more stable nickel-rich material is possible. It identifies the reasons why substitution can work in cathode materials. Additionally, the methods described can provide a guideline to further studies of stabilization of the cathode.

Understanding and Controlling the Degradation and Stabilization of Nickel-rich Lithium-ion Layered Cathodes

James David Steiner

ABSTRACT (Public)

Consumers across the world use lithium-ion batteries in some fashion in their everyday life. The growing demand for energy has led to batteries dying quicker than consumers want. Thus, there are calls for researchers to develop batteries that are longer lasting. However, the initial increase in battery life over the years has been from better engineering and not necessarily from making a better material for a battery.

This thesis focuses on the understanding of the chemistry of the materials of a battery. Throughout the chapters, the research delves into the how and why materials with extra nickel degrade quickly. Then, it investigates a method of making these nickel-rich materials last longer and how the chemistry within these materials are affected by the addition of a different metal. Overall, the findings indicate that the addition of titanium creates a more stable material because it mitigates the release of oxygen and prevents irreversible changes within the structure of the material.

It determines that the chemistry behind the failings of nickel-rich lithium-ion batteries and a potential method for allowing the batteries to last longer. It also provides insight and guidance for potential future research of stabilization of lithium-ion materials

Dedication

This thesis is dedicated to
My beautiful wife, Elizabeth Steiner
Our first wonderful daughter, Madeleine
And our child on the way

Acknowledgements

First, I want to acknowledge my advisor Dr. Feng Lin. Without his guidance and support none of this would be possible. In the two years in his group I have learned more about science than I ever thought possible. I feel more confident and prepared for a career than I did when he accepted me into his new group, and he has always been available for support and advice on anything I have brought to him. Additionally, I want to thank my lab mates in our group. Specifically, I want to mention Dr. Linqin Mu, Muhammad Mominur Rahman, David Kautz, and Crystal Waters. We started this group together and worked through all the bumps of a new group. Without their input and advice as I worked through my projects, I may never have finished this quickly.

Second, my wife Elizabeth has been by my side first through law school and now through graduate school. She has provided endless encouragement as I have toiled through the extra schooling. Without her I know law school and passing the bar may never have happened, and then her support as I have worked through graduate school has allowed me to get where I am today. Additionally, my in-laws Steve and Cindy Dam have encouraged us both as we have made several decisions since the start of our marriage and provided the support and love we have needed.

Finally, my parents, Marc and Deanna Steiner have always supported any decisions I have made and listened as I have discussed topics about law and chemistry endlessly over the last five years. Having them as parents made me who I am today and have allowed me to achieve my dreams.

Table of Contents

Attributions

Chapter 2 was submitted and accepted for publication in *ACS Applied Materials and Interfaces* **DOI:** 10.1021/acsami.8b06399. The manuscript is formatted for this publication. James Steiner analyzed the data and wrote the manuscript. Dr. Feng Lin directed the project and provided guidance on the data and manuscript. James Steiner additionally performed the synthesis, performance testing, and data characterization. Undergraduates Julia Walsh and Benjamin Zydlewski assisted with the synthesis. Muhammad Mominur Rahman and Dennis Nordlund collected the soft XAS data at SLAC National Accelerator Laboratory. Dr. Linqin Mu assisted with TEM acquisition. F. Marc Michel assisted with XRD acquisition. Finally, Huolin L. Xin collected the STEM-EELS data.

Chapter 3 is being prepared as a communication to be submitted to a journal, likely a chemistry journal. James Steiner developed the synthesis method, analyzed the data, and wrote the manuscript. He additionally performed the synthesis, sample preparations for all characterization methods, performance testing, and data characterization. Dr. Feng Lin directed the project and provided guidance on the data and manuscript. Hao Cheng and Dr. Jincheng Zheng performed all theoretical calculations for this work. Undergraduates Julia Walsh and Benjamin Zydlewski assisted with the synthesis. Yan Zhang and Dennis Nordlund collected the soft XAS data at SLAC National Accelerator Laboratory. Dr. Linqin Mu, Zhengrui Xu, and Dr. Cheng-Jun Sun collected the hard XAS data at Argonne National Laboratory. F. Marc Michel assisted with XRD acquisition. Finally, Huolin L. Xin collected the STEM-EELS and STEM-EDS data.

Abbreviations

DFT, Density function theory

EDS, Energy-dispersive Spectroscopy

EELS, Electron Energy Loss Spectroscopy

EXAFS, Extended X-ray absorption fine structure

FDMNES, Finite Difference Method Near Edge Structure

FFT, Fast Fourier Transformation

FWHM, Full Width Half Maximum

FY, Fluorescence Yield

HOMO, Highest Occupied Molecular Orbital

LCO, Lithium Cobalt Oxide

LIB, Lithium-ion Batteries

LMR, Lithium Manganese Rich

LNO, Lithium Nickel Oxide

LUMO, Lowest Unoccupied Molecular Orbital

NMC, $LiNi_{1-x-y}Mn_xCo_yO_2$

NMC811, $LiNi_{0.8}Mn_{0.1}Co_{0.1}O_2$

SEI, Solid Electrolyte Interphase

SEM, Scanning Electron Microscopy

STEM, Scanning Transmission Electron Microscopy

TEM, Transmission Electron Microscopy

TEY, Total Electron Yield

XAS, X-ray Absorption Spectroscopy

XANES, X-ray absorption near edge structure

XRD, X-ray Diffraction

Chapter 1. Introduction

Since 1991, commercial electronics have used lithium ion batteries (LIBs), which has caused consumers to become more energy hungry and to want to add these batteries to cars, phones, cameras, computers, and grid storage.[1–3] Now LIBs hold twice as much energy, and cost ten times less, but for electric cars they are not close to providing the range of petroleum cars.[2,3] Industry desires batteries with higher energy density that are safe, affordable, and have good cycle life.[4] LIBs have been studied extensively since their inception and it is important to study the chemical degradation of the cathode, including oxygen oxidation (i.e., oxygen activity), side reactions with the electrolyte, and how it affects cell performance.[4] Oxygen evolution is one of the key issues facing most LIBs since it raises safety concerns and structural changes within the cathode that limit the cycle life of batteries.

LIBs continue to move towards nickel-rich layered cathodes, especially lithium nickel manganese cobalt layered oxide materials ($LiNi_{1-x-y}Mn_xCo_yO_2$, NMC).[1] Nickel-rich cathodes (1-x-y >= 0.6) have clear advantages, such as higher practical capacity and lower cost, but there are also consequences, for example, structural degradation and thermal instability. Our work focuses on stabilizing a nickel-rich cathode, specifically $LiNi_{0.8}Mn_{0.1}Co_{0.1}O_2$ (NMC811). This chapter focuses on the background of layered metal oxide cathodes, their potential oxygen activation and release (primarily participating in electrolyte oxidation), the degradation caused by the release, and the potential for transition metal doping.

1.1. Layered Transition Metal Oxides

When developing efficient LIBs, the cathode crystal structure plays a key role in conductivity, voltage, cyclability, and rates of charge and discharge.[5–7] Layered metal

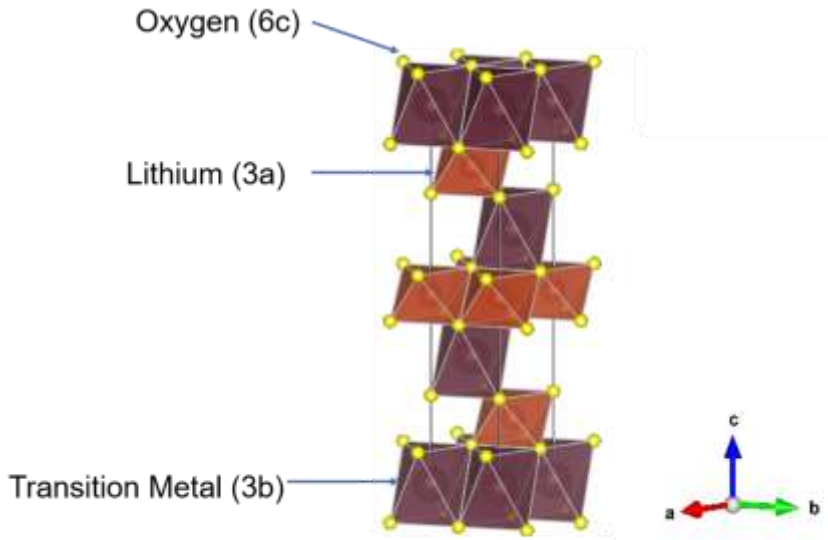

Figure 1-1. Schematic representation of a layered oxide structure with the individual sites labeled for clarity.

oxides represent a common structure used for cathode materials, where the transition metal, oxygen, and lithium form alternating layers, and there are three transition metal layers per unit cell forming an O3 arrangement, or an R$\bar{3}$m space group (**Figure 1-1**).[5,8] In the layered structure, the transition metals are in 3b sites, while lithium is in the 3a site.[5,8] The layered structure allows for better mobility of the lithium ions during migration across a two-dimensional interstitial space .[8] With its more compact design, it allows for more energy storage and more efficient lithium migration.[6,9] Batteries are created with a lithiated cathode paired with an anode, then upon charging, lithium ions migrate from the lattice of the cathode and deposit on (or intercalate into) the anode, then upon discharge the lithium ions return to their site in the cathode lattice.[6,8,9]

For cathode chemistry, ideally, there would not be any side reactions or surface reconstruction of the cathode particles during cycling.[5,6,9] However, each known cathode material has flaws. Lithium cobalt oxide ($LiCoO_2$, LCO) materials are currently the most successful cathodes as they are used in the majority of commercial devices.[10,11] LCO batteries have been widely used due to their high conductivity, low chance of self-discharge, and good cycle life.[10–12]

LCO batteries still have several hurdles that limit their long-term usage. When charging an LCO material, the delithiation is reversible upon discharge; however, if more than 50-60% of the lithium is removed, the cycle life of the battery decreases.[5,13] Thus, to mitigate this problem, the charging voltage of commercial electronics is usually limited to 4.2 V versus a graphite anode to prevent excessive delithiation.[5,13] The cycle loss has been attributed to possible side reactions with the electrolyte forming a passive surface layer resistance, as well as cell degradation from the LCO losing its characteristic O3 phase.[5,13] During delithiation, the cathode particles undergo phase transformation as the O3 layered structure, CBA packing, starts to transition into H1-3 and O1 packing. In H1-3 there are O-Co-O layers, where only every other layer has the CBA stacking of O3.[13–16] At higher delithiation levels, the phase transformations become more prominent, causing the chemical diffusion coefficient of lithium to drop, meaning it is more difficult for lithium migration.[13,15] These phase changes cause more problems at voltages around 4.6V, so LCO materials are limited to lower voltages, which limits applications of the material.[13,15] Additionally, of the first row transition metals used in cathode materials, cobalt is the least abundant, which drastically raises its cost.[11] There have been attempts at higher voltage LCO materials, but it does not completely mitigate the other

consequences of the cathode.[17,18] Thus, a change in cathode materials could create cheaper, more efficient batteries, but finding a similar working material is challenging.

Research turned to lithium nickel oxides ($LiNiO_2$, LNOs), since LNOs have the same layered structure as LCO, however, pure LNOs pose several different problems.[11] Nickel-rich materials have a higher energy density due to its redox potential that can result in a higher practical capacity than LCO materials, but nickel cathodes are not as safe as cobalt. Nickel ions, especially 2+, have a similar size to the lithium ion, and

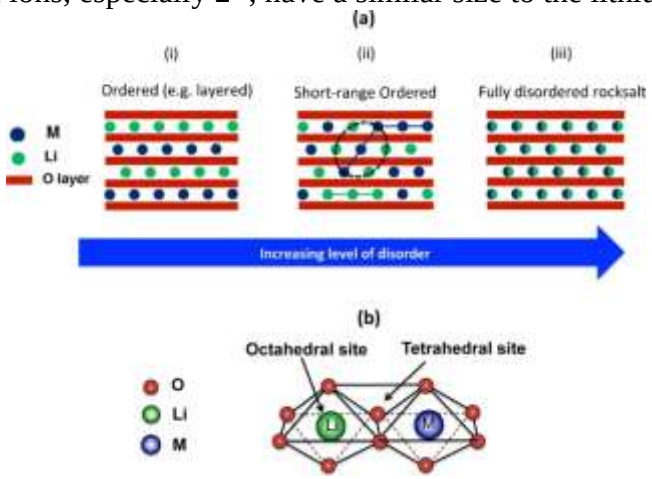

Figure 1-2. Schematic representation of degrees of disorder of a layered structure as a transition metal (nickel) exchanges lattice places with lithium. (a) represents (i) completely ordered system, (ii) some cation disorder occurring, and (iii) a disordered rock-salt structure that tends to occur on the surface of nickel-rich materials. (b) demonstrates the rock-salt formation and how the ions are coordinated. Reprinted with permission from Abdellahi, A.; Urban, A.; Dacek, S.; Ceder, G. Understanding the Effect of Cation Disorder on the Voltage Profile of Lithium Transition-Metal Oxides. Chem. Mater. **2016**, 28 (15), 5373–5383,[54] which can be found at *https://pubs.acs.org/doi/abs/10.1021/acs.chemmater.6b01438*. Any requests for future uses should be directed to the American Chemical Society.

during delithiation, the nickel ion can migrate into lithium sites, hindering lithium migration during discharge.[11,19] The migration of nickel causes the layered structure to lose its stability, causing spinel ($Fd\bar{3}m$) or rock salt structure ($Fm\bar{3}m$) formation and limiting lithium diffusion, which hinders cycle life (**Figure 1-2**).[11,20–22]

Furthermore, the Ni^{3+} and Ni^{4+} are more easily reduced than their cobalt counterpart, which causes the LNO to be more thermally unstable than LCO.[11,23] Additionally, as oxygen is released as a result of delithiation, more nickel reduces and forms spinel and rock salt structures, which makes batteries containing pure LNOs almost impossible to operate at the conditions used in LCO.[11,24,25]

To deal with LCO's cost and LNO's instability, research has shifted to using multiple transition metals in cathodes. Substitution of nickel with small amounts of cobalt helps limit disorder of the layered structure, which prevents as much nickel migration.[5,11,23] The development of mixed materials such as $LiNi_{0.8}Co_{0.15}Al_{0.5}O_2$ (NCA) cathodes has helped limit migration and increase thermal stability and cell performance,[5,11,26,27] This has allowed consumers, such as Tesla Motors, to buy NCAs for use in applications such as electric vehicles. NCA materials are just one of the many attempts at mixing cations to help create better batteries.

The current commercial NMC uses nickel, manganese and cobalt in equal proportions ($LiNi_{0.33}Mn_{0.33}Co_{0.33}O_2$) so they are in the +2, +4, and +3 oxidation states, respectively.[28] Cobalt limits the anti-site mixing, while manganese helps the thermal stability, creating a more stable and structurally sound battery. Additionally, during cycling, only the nickel oxidizes during the beginning of cycling, then cobalt will oxidize at higher voltages (although this is still under debate),[29] while manganese remains

inactive, increasing the thermal stability of the particles and overcoming some of the deficiencies seen in LCO batteries.[30,31]

While equal proportion NMC cathodes have better electrochemical performance, thermal stability, and structural performance, they still have a lot of the issues of LCO batteries, including a lot of costly cobalt. Thus, there is a push to study the effects of nickel-rich NMC materials, but it requires overcoming the problems of LNO cathodes, including the surface reconstruction layer, oxygen loss from the lattice, and thermal stability of the particles.[21] To stabilize nickel-rich NMC cathodes, it is necessary to understand the mechanisms behind their degradation, specifically oxygen activation.

1.2. Oxygen Bonding and Activation

Oxygen and heat evolution from the lattice of nickel-rich NMC cathodes pose a problem to capacity and cycle life.[32–34] In NMC materials, the effect of oxygen can vary based on where it is in the cathode. As nickel content in the materials increases, more oxygen will be lost from the surface because more Ni^{4+} will reduce while oxidizing O^{2-}.[32,34] Generally, irreversible oxidation and oxygen loss occurs on the surface, while the bulk oxygen oxidation is reversible.[32] Two theories could possibly apply to oxygen activation of nickel-rich materials. One has been applied mostly to Lithium Manganese Rich (LMR) NMC materials, while the other is a theory for nickel rich materials. Both deal with the role of oxygen bonds in the lattice.

1.2.1. Oxygen Activation with Li-O-Li Bonds

A key theory of oxygen activation concerns the idea of surface reconstruction seen in lithium rich materials, but could apply to nickel-rich materials.[35] In lithium-rich

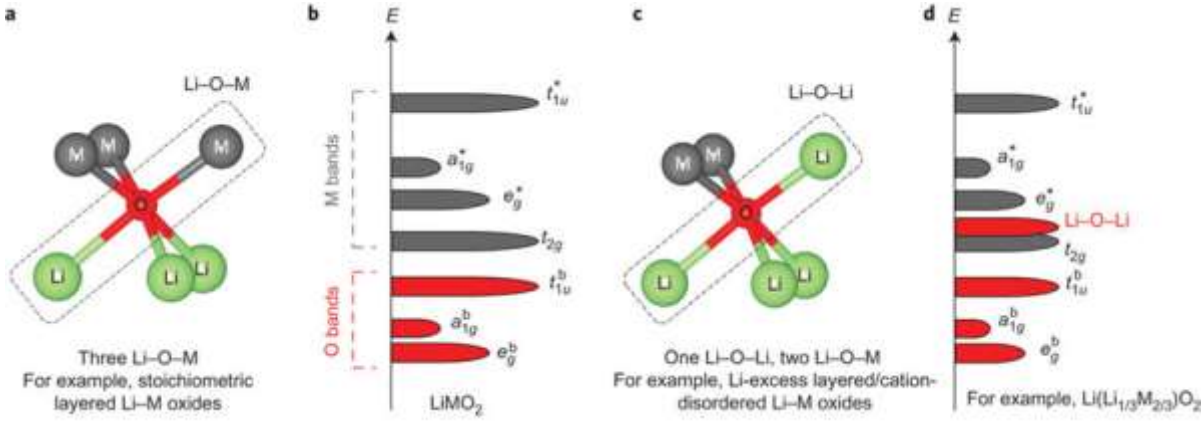

Figure 1-3. Represents the difference in hybridization bands and energy between (a) an rdered and (c) adisordered system. (b) and (d) schematically demonstrate the band structures of the systems. The Li-O-Li bond has been shown to be the location of oxygen oxidation in its O2p orbitals. As shown, the disorder causes an unhybridized Li-O-Li to become higher energy than the hybridized 2p orbitals, so it is more easily oxidized. Reprinted with permission from Springer Nature: Seo, D.; Lee, J.; Urban, A.; Malik, R.; Kang, S.; Ceder, G. The Structural and Chemical Origin of the Oxygen Redox Activity in Layered and Cation-Disordered Li-Excess Cathode Materials. Nat. Chem. **2016**, 8 (July), 692–697,[41] Copyright 2016. This is a one-time permission for use, any other uses must request permission from Springer Nature.

materials anti-site mixing can result in rock-salt formation. This theoretically alters the bonding of oxygen to be linearly connected to two lithium ions (**Figure 1-3**),[35] and the cation disorder in nickel-rich materials provides an environment that could allow a similar result. The cation mixing creates a lithium rich environment with some Li-O-Li bonds rather than a typical ordered Li-O-TM bond.[35] The new configuration creates

oxygen orbitals that are closer to in energy to a 2p orbital, which have higher energies than the hybridized orbitals of oxygen for the Li-O-TM bonds.[35]

Holes along this Li-O-Li bond show that oxygen oxidation occurs in this region of the lattice during delithiation,[35–37] which results in oxygen loss or formation of peroxide like structure, which will be discussed in detail later.[35,38] In ordered layered oxides, there is overlap between the oxygen 2p orbitals and the transition metal d orbitals that causes hybridization, with bonding orbitals exhibiting oxygen dominant characteristics, while any anti-bonding and non-bonding orbitals have transition metal dominant characteristics. Thus, in a perfect layered structure, the oxidation will initially occur on the transition metal sites because the Fermi level is between t_{2g} and e_g^* (**Figure 1-3b**), thus the highest occupied orbitals would be in metal orbitals.[35–37] However, the Li-O-Li bonds have oxygen 2p orbitals that are between the orbitals allowing for oxygen to oxidize. Theoretically, in nickel-rich materials, the structural changes could also isolate a 2p orbital that could become higher energy than the other orbitals, which would allow for oxygen oxidation and loss from the cathode.[22]

1.2.2. Nickel-Oxygen Bond Covalency

A theoretical study has researched the effects of high nickel contents in NMC materials on the stability of the nickel and oxygen bond.[39] Increasing the nickel content of an NMC material will increase the starting oxidation state of nickel. This in turn can lead to nickel reaching the unstable Ni^{+4} oxidation that helps provide higher initial capacities, but leads to quicker cell degradation.[40] Understanding the reasons for the instability with high nickel-oxidation can in turn lead to development of more stable nickel-rich cathodes to mitigate these problems.

As nickel content increases, up to especially $LiNi_{0.8}Mn_{0.1}Co_{0.1}O_2$, the concentration of Ni^{4+} will increase, which correlates to typical observations of high nickel content having higher initial capacities with lower capacity retention. Based on theoretical calculations, the Ni^{4+} lowest unoccupied molecular orbital (LUMO) has a lower energy than other nickel oxidation states and approaches the highest occupied molecular orbital (HOMO) of oxygen, and is much more covalent in character; thus it is likely to be reduced by either the oxygens in the lattice or even the electrolyte due to electron delocalization (**Figure 1-4)**.[39]

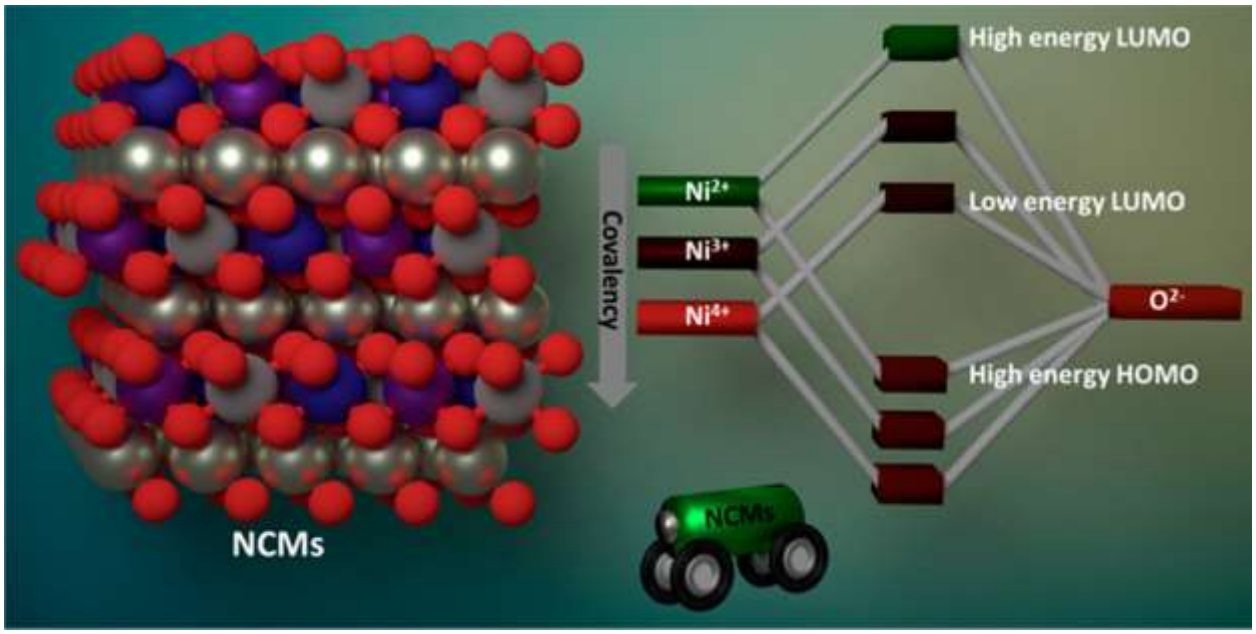

Figure 1-4. Schematic representation of molecular orbitals demonstrating the lowering energy as nickel oxidizes. Reprinted with permission from Dixit, M.; Markovsky, B.; Schipper, F.; Aurbach, D.; Major, D. T. Origin of Structural Degradation during Cycling and Low Thermal Stability of Ni-Rich Layered Transition Metal-Based Electrode Materials. J. Phys. Chem. C **2017**, 121 (41), 22628–22636.[39] Copyright 2017 American Chemical Society. This is a one-time permission. Any other use must get permission directly from the American Chemical Society.

Notably, one of the keys to a stable cathode is the M-O bond due to the layered structure. Delocalization of the electrons occurs as the bonds become more covalent, this leads to a weakened Ni-O bond, which degrades the cathode.[39] Limiting the covalency between the nickel and oxygen in the lattice can help prevent the oxygen loss. This theory appears to be the most applicable to our research.

1.2.3. Electrolyte Reactions

Typical electrolytes in lithium ion batteries are 1M of lithium salts (i.e. $LiPF_6$) dissolved in an organic solvent mixture, such as ethylene carbonate (EC) and ethyl methyl carbonate (EMC), with a typical ratio of 3:7 EC/EMC.[41] Oxygen within the lattice can react with the electrolyte, which can trigger several further side reactions in the cathode.[35,42,43] Hypothetically, as the lithium is removed from the cathode, then the electrolyte oxidizes in the presence of lattice oxygen.[37,43] Upon the oxidation of transition metals, the transition metals with high oxidation state, such as Ni^{4+}, will reduce as the electrolyte oxidizes. The electrolyte will oxidize to an aldehyde, water, and carbon dioxide, and then the aldehyde could oxidize further in the presence of the transition metal to carboxylic acid.[43]. The side reactions can cause initial capacity increase as more lithium is removed, but at the cost of oxygen loss, electrolyte decomposition, and structural reformation of the cathode, which hinder the cell's lifetime due to continued decomposition of the electrolyte.[37,43,44]

Alternatively, oxygen loss can occur in the particles on its own without the electrolyte due to cycling and ion migration, as discussed earlier, and the oxygen gas can react with the electrolyte.[37,43] The alternative reaction may not decompose the electrolyte, but it can lead to nonuniform particles that can crack and change during cycling, leading

to more particle exposure to the electrolyte and the side reactions,[42,43] which causes more side reactions, structure degradation, and electrolyte decomposition.

1.3. Potential Cathode Degradation

It is believed that the surface and bulk of the cathode have different reactions that affect the oxygen and transition metal oxidation.[45] Research of LMR materials have revealed two models for possible oxygen reactions, that could apply to nickel-rich materials as we attempt to understand how changes on the surface affect the overall chemistry of the bulk. One model suggests that as oxygen oxidizes on the surface, the surface oxygen is lost, and the bulk oxygen migrates to the surface, which leaves vacancies in the crystal structure.[46] However, the other suggests that as the structure loses the surface oxygen, the transition metals, especially nickel, migrate into vacated lithium sites on the surface, which causes surface reconstruction and fewer sites for the lithium to return to upon discharge.[46]

Dual phased materials are common during delithiation of layered oxides as structural changes occur to stabilize the lattice upon loss of lithium. With proposed oxygen loss phases, there are two phases that form during cycling. The first phase occurs in the bulk and maintains the pristine materials structure as the oxidation of oxygen remains reversible and structural changes are limited.[46] The second phase occurs on the surface, as the transition metals, especially nickel, oxidize to high states and will reduce at the cost of oxygen loss and leading to a more dense surface layer.[46,47] The separate phases are similar to surface reconstruction of nickel-rich materials, and could help us understand oxygen oxidation in nickel-rich materials, and could lead to strain and microcracking.

1.3.1 Microcracking

Microcracks occurring in cathode particles are known to be a key contributor to cell degradation.[48,49] Microcracks begin to form within the particles, either within the individual NMC particles (primary particles) or along the grain boundaries, where primary particles aggregate to form larger secondary particles.[8] These cracks can be a direct result of oxygen evolution that occurs as a result of the activated oxygen.[50] Cracks occur where the primary particles come together because the primary particles constrain each other when they form secondary particles, and thus volume changes can cause stress between the primary particles and lead to cracks during cycling.[8] These microcracks form on the surface as a result of cycling because as lithium leaves the cathode, the lattice in the c direction expands, but the a and b directions contract, causing volume changes in the particles.[8,51,52] In nickel-rich materials, the previously discussed surface reconstruction causes a different surface when compared to the bulk layered structure as the nickel ions migrate into lithium sites..[46,53,54] Due to the mismatch of the bulk and surface crystal structures, lithium migration during cycling causes different volume changes on the surface and bulk, which leads to strain on the particles and more cracks to form and oxygen to be evolved, in a similar way as the phase boundary volume differences causes cracks to form.[8,46,47,52]

As microcracks worsen, more of the particles are exposed to the electrolyte, which results in side reactions, oxygen loss, and degradation of the cycle life. As the electrolyte penetrates deeper it forms a thick cathode electrolyte interphase (CEI) with thicker surface reconstruction that limits ion transport channels and the battery degrades.[8,53] In nickel-rich materials, as the cracks form, more of the cathode has an interaction layer with the electrolyte, causing more surface reconstruction.[8] Since

microcracking results from similar circumstances as oxygen oxidation, controlling surface changes and reactions with the electrolyte can help limit microcracking as well as oxygen loss.

1.3.2. Transition Metal Dissolution

The oxidation of the electrolyte can alter cell performance and the distribution of the transition metals, which can lead to metal dissolution.[55,56] The changes seen in nickel-rich cathodes can cause the perfect environment for transition metal dissolution and further surface reduction.[57] The vacancies from oxygen loss weaken the bonds between transition metal, such as cobalt, and oxygen, which changes the surface to allow it to oxidize the organic solvents in the cell and accompanies the transition metal dissolution.[55,56] A proposed idea for metal dissolution is that the electrolyte reacts with the transition metal through coordination.[57] The coordination creates complexes between the organic compounds and the transition metal which, as cycling continues, can be removed from the cathode structure, and travel through the electrolyte.[55,57] Then the metals travel across the cell, and deposit on the SEI on the anode, which will cause deterioration of cell performance.[57]

$LiPF_6$, a common component of lithium ion electrolytes, appears to be a main culprit of metal dissolution.[58] The salt has been shown to cause dissolution and pores on the cathode surface. This allows the electrolyte to penetrate deeper, which compounds the problems observed with surface reconstruction, oxygen evolution, and metal dissolution.[58,59] The issue posed is as the salt decomposes, it causes reactions with the surface, perpetuating redox reactions that cause the transition metals to react with lost fluorine and HF, which are soluble in the electrolyte and can then dissolve from the

cathode and move across the cell.[58,60] Changing the salt to $LiBF_4$ has resulted in less dissolution, but it limits SEI formation causing an increase in reactions with the electrolyte and heat generation. On the anode, SEI formation limits anode reactions with the electrolyte and with $LiBF_4$ resulting in additional oxidation of the electrolyte releasing additional gas that increases heat from the cell.[58] Therefore, limiting dissolution with $LiBF_4$ may hinder overall safety of the cell.[58,59] Thus, the use of $LiPF_6$ would be preferred over additional heat evolution of the cell, but finding alternatives could help cycle life and safety of the cell. Our work currently uses a different approach. Rather than changing the salt used, we provide additional additive in a small weight percentage of vinylene carbonate. Additives such as this can help mitigate some of the issues discussed here.

1.4. Transition Metal Doping

As seen previously, there have been attempts to change ratios of transition metals to mitigate the consequences of excess nickel.[21] Doping or substitution of the cathode with various elements may work without sacrificing too much practical capacity.[61–63] The use of different metals is a key point of research in cathode materials. The ideas include substituting the lattice with a new metal, coating the outside of the cathode material, or substitution with different transition metals.[61,62,64] Substitution of metals, such as aluminum or titanium, can be used to help prevent surface reconstruction, and prevent metal dissolution.[61,62] Titanium (IV) is a known dopant that has been shown to stabilize cathode materials, and help limit surface changes, even in nickel-rich materials.[61,65] The Ti^{4+} is thought to replace some Co^{3+} in the lattice with manganese reduction to compensate and maintain charge neutrality.[66] The incorporation of titanium

increases the slab distance in the lattice and allows for more efficient lithium diffusion that can allow for better reversibility and high capacities.[67] However, as with most metals, adding too much can act as an impurity, hurting the cell performance because Ti^{4+} is electrically inactive.[61,62] The addition of a small amount of titanium could allow for more lithium to be removed from the NMC particles while maintaining lattice stability.[61,68]

Doping or substitution involves incorporating the additional metal into the bulk or surface of the cathode without substituting for another metal.[62,64] However, what has been seen is that in small amounts, less than 5%, adding an additional metal as a dopant can help the cathode.[61,62,64,69] The effects on cathodes have been monitored but the surface and bulk differences are not fully understood.[62]

1.5. Research Goals

Nickel-rich NMC materials can provide a strong replacement to LCO materials that are cheaper and longer lasting. The main holdback is overcoming the stability problems known with nickel-based cathodes. The main concept of our research focuses on understanding and possibly limiting oxygen activation in the lattice. The ability to deactivate oxygen can limit the cathode degradation discussed in this chapter. Chapter 2 will investigate the surface and bulk changes during cycling of nickel-rich cathodes. We used varied surface analysis techniques to understand oxidation state changes in the cathode and the degradation of the cathode. Chapter 3 then focuses on the gradient substitution of transition metal into our nickel-rich materials and the experimental and theoretical results for how titanium stabilizes the cathode material.

1.6. References

References

(1) Manthiram, A.; Song, B.; Li, W. A Perspective on Nickel-Rich Layered Oxide Cathodes for Lithium-Ion Batteries. *Energy Storage Mater.* **2017**, *6* (August 2016), 125–139.

(2) Armand, M.; Tarascon, J.-M. Building Better Batteries. *Nature* **2008**, *451* (7179), 652–657.

(3) Noorden, R. Van. The Rechargeable Revolution: A Better Battery. *Nature* **2014**, *507*, 26–28.

(4) Goodenough, J. B.; Park, K. S. The Li-Ion Rechargeable Battery: A Perspective. *J. Am. Chem. Soc.* **2013**, *135* (4), 1167–1176.

(5) Doeff, M. *Encyclopedia of Sustainability Science and Technology*; 2012.

(6) Whittingham, M. S. Lithium Batteries and Cathode Materials. *Chem. Rev.* **2004**, *104* (10), 4271–4301.

(7) Lin, F.; Nordlund, D.; Markus, I.; Weng, T.-C.; Xin, H. L.; Doeff, M. Profiling the Nanoscale Gradient in Stoichiometric Layered Cathode Particles for Lithium-Ion Batteries. *Energy Environ. Sci.* **2014**, 3077–3085.

(8) Liu, W.; Oh, P.; Liu, X.; Lee, M. J.; Cho, W.; Chae, S.; Kim, Y.; Cho, J. Nickel-Rich Layered Lithium Transition-Metal Oxide for High-Energy Lithium-Ion Batteries. *Angew. Chemie - Int. Ed.* **2015**, *54* (15), 4440–4457.

(9) Choi, N. S.; Chen, Z.; Freunberger, S. A.; Ji, X.; Sun, Y. K.; Amine, K.; Yushin, G.; Nazar, L. F.; Cho, J.; Bruce, P. G. Challenges Facing Lithium Batteries and Electrical Double-Layer Capacitors. *Angew. Chemie - Int. Ed.* **2012**, *51* (40), 9994–10024.

(10) Mizushima, K.; Jones, P. C.; Wiseman, P. J.; Goodenough, J. B. Li_xCoO_2 ($0<x<1$): A New Cathode Material for Batteries of High Energy Density. *Mater. Res. Bull.* **1980**, *15*, 783–789.

(11) Nitta, N.; Wu, F.; Lee, J. T.; Yushin, G. Li-Ion Battery Materials: Present and Future. *Mater. Today* **2015**, *18* (5), 252–264.

(12) Du Pasquier, A.; Plitz, I.; Menocal, S.; Amatucci, G. A Comparative Study of Li-Ion Battery, Supercapacitor and Nonaqueous Asymmetric Hybrid Devices for Automotive Applications. *J. Power Sources* **2003**, *115* (1), 171–178.

(13) Chen, Z.; Dahn, J. R. Methods to Obtain Excellent Capacity Retention in LiCoO2 Cycled to 4.5 V. *Electrochim. Acta* **2004**, *49* (7), 1079–1090.

(14) Van der Ven, A.; Aydinol, M. K.; Ceder, G.; Kresse, G.; Hafner, J. First-Principles Investigation of Phase Stability in Li_xCoO_2. *Phys. Rev. B* **1998**, *58* (6), 2975–2987.

(15) Xia, H.; Lu, L.; Meng, Y. S.; Ceder, G. Phase Transitions and High-Voltage Electrochemical Behavior of $LiCoO_2$ Thin Films Grown by Pulsed Laser Deposition. *J. Electrochem. Soc.* **2007**, *154* (4), A337.

(16) Gabrisch, H.; Yazami, R.; Fultz, B. The Character of Dislocations in $LiCoO_2$. *Electrochem. Solid-State Lett.* **2002**, *5* (6), A111.

(17) Li, B.; Wang, Y.; Lin, H.; Liu, J.; Xing, L.; Xu, M.; Li, W. Improving High Voltage Stability of Lithium Cobalt Oxide/Graphite Battery via Forming Protective Films Simultaneously on Anode and Cathode by Using Electrolyte Additive. *Electrochim. Acta* **2014**, *141*, 263–270.

(18) Liu, Y.; Wang, K.; Lin, Y.; Zhu, Y.; Tu, W.; Xu, M.; Liu, X.; Li, B.; Li, W.

Tetrafluoroterephthalonitrile: A Novel Electrolyte Additive for High-Voltage Lithium Cobalt Oxide/Graphite Battery. *Electrochim. Acta* **2017**, *256*, 307–315.
(19) Rougier, A.; Gravereau, P.; Delmas, C. Optimization of the Composition of the $Li_{1-Z}Ni_{1+z}O_2$ Electrode Materials: Structural, Magnetic, and Electrochemical Studies. *J. Electrochem. Soc.* **1996**, *143* (4), 1168–1175.
(20) Lin, F.; Markus, I. M.; Nordlund, D.; Weng, T.-C.; Asta, M. D.; Xin, H. L.; Doeff, M. M. Surface Reconstruction and Chemical Evolution of Stoichiometric Layered Cathode Materials for Lithium-Ion Batteries. *Nat. Commun.* **2014**, *5*, 3529.
(21) Zheng, J.; Kan, W. H.; Manthiram, A. Role of Mn Content on the Electrochemical Properties of Nickel-Rich Layered $LiNi_{0.8-X}Co_{0.1}Mn_{0.1+xO2}$ (0.0<X< 0.08) Cathodes for Lithium-Ion Batteries. *ACS Appl. Mater. Interfaces* **2015**, *7* (12), 6926–6934.
(22) Hwang, S.; Chang, W.; Kim, S. M.; Su, D.; Kim, D. H.; Lee, J. Y.; Chung, K. Y.; Stach, E. A. Investigation of Changes in the Surface Structure of $Li_xNi_{0.8}Co_{0.15}Al_{0.05}O_2$ Cathode Materials Induced by the Initial Charge. *Chem. Mater.* **2014**, *26* (2), 1084–1092.
(23) Kalyani, P.; Kalaiselvi, N. Various Aspects of $LiNiO_2$ Chemistry: A Review. *Sci. Technol. Adv. Mater.* **2005**, *6* (6), 689–703.
(24) Kanno, R.; Kubo, H.; Kawamoto, Y.; Kamiyama, T.; Izumi, F.; Takeda, Y.; Takano, M. Phase Relationship and Lithium Deintercalation in Lithium Nickel Oxides. *Journal of Solid State Chemistry*. 1994, pp 216–225.
(25) Thomas, M.G.S.R., David, W.I.F., and Goodenough, J. B. Synthesis and Structural Characterization of the Normal Spinel $LiNi_2O_4$. *Mater. Res. Bull.* **1985**, *20* (10), 1137–1146.
(26) Guilmard, M.; Pouillerie, C.; Croguennec, L.; Delmas, C. Structural and Electrochemical Properties of $LiNi_{0.70}Co_{0.15}Al_{0.15}O_2$. *Solid State Ionics* **2003**, *160* (1–2), 39–50.
(27) Dahn, J. R.; Fuller, E. W.; Obrovac, M.; von Sacken, U. Thermal Stability of Li_xCoO_2, Li_xNiO_2 and λ-MnO_2 and Consequences for the Safety of Li-Ion Cells. *Solid State Ionics* **1994**, *69* (3–4), 265–270.
(28) Koyama, Y.; Tanaka, I.; Adachi, H.; Makimura, Y.; Ohzuku, T. Crystal and Electronic Structures of Superstructural $Li_{1-x}[Co_{1/3}Ni_{1/3}Mn_{1/3}]O_2$ ($0 \leq x \leq 1$). *J. Power Sources* **2003**, *119–121*, 644–648.
(29) Petersburg, C. F.; Li, Z.; Chernova, N. A.; Whittingham, M. S.; Alamgir, F. M. Oxygen and Transition Metal Involvement in the Charge Compensation Mechanism of $LiNi_{1/3}Mn_{1/3}Co_{1/3}O_2$ Cathodes. *J. Mater. Chem.* **2012**, *22*, 19993–20000.
(30) Kobayashi, H.; Arachi, Y.; Emura, S.; Tatsumi, K. Investigation on Lithium De-Intercalation Mechanism for $LiNi_{0.45}Mn_{0.45}Al_{0.1}O_2$. *Solid State Ionics* **2007**, *178* (15–18), 1101–1105.
(31) Hwang, B. J.; Tsai, Y. W.; Carlier, D.; Ceder, G. A Combined Computational/Experimental Study on $LiNi_{1/3}Co_{1/3}Mn_{1/3}O_2$. *Chem. Mater.* **2003**, *15* (19), 3676–3682.
(32) Manthiram, A.; Knight, J. C.; Myung, S. T.; Oh, S. M.; Sun, Y. K. Nickel-Rich and Lithium-Rich Layered Oxide Cathodes: Progress and Perspectives. *Adv. Energy Mater.* **2016**, *6* (1).
(33) Bang, H. J.; Joachin, H.; Yang, H.; Amine, K.; Prakash, J. Contribution of the

Structural Changes of $LiNi_{0.8}Co_{0.15}Al_{0.05}O_2$ Cathodes on the Exothermic Reactions in Li-Ion Cells. *J. Electrochem. Soc.* **2006**, *153* (4), A731.

(34) Xu, J.; Hu, E.; Nordlund, D.; Mehta, A.; Ehrlich, S. N.; Yang, X. Q.; Tong, W. Understanding the Degradation Mechanism of Lithium Nickel Oxide Cathodes for Li-Ion Batteries. *ACS Appl. Mater. Interfaces* **2016**, *8* (46), 31677–31683.

(35) Seo, D.; Lee, J.; Urban, A.; Malik, R.; Kang, S.; Ceder, G. The Structural and Chemical Origin of the Oxygen Redox Activity in Layered and Cation-Disordered Li-Excess Cathode Materials. *Nat. Chem.* **2016**, *8* (July), 692–697.

(36) Streich, D.; Erk, C.; Gueguen, A.; Muller, P.; Chesneau, F.-F.; Berg, E. J. Operando Monitoring of Early Ni-Mediated Surface Reconstruction in Layered Lithiated Ni-Co-Mn Oxides. *J. Phys. Chem. C* **2017**, *121* (25), 13481–13486.

(37) Ma, C.; Alvarado, J.; Xu, J.; Clément, R. J.; Kodur, M.; Tong, W.; Grey, C. P.; Meng, Y. S. Exploring Oxygen Activity in the High Energy P2-Type $Na_{0.78}Ni_{0.23}Mn_{0.69}O_2$ Cathode Material for Na-Ion Batteries. *J. Am. Chem. Soc.* **2017**, *139* (13), 4835–4845.

(38) Sathiya, M.; Rousse, G.; Ramesha, K.; Laisa, C. P.; Vezin, H.; Sougrati, M. T.; Doublet, M.-L.; Foix, D.; Gonbeau, D.; Walker, W.; et al. Reversible Anionic Redox Chemistry in High-Capacity Layered-Oxide Electrodes. *Nat. Mater.* **2013**, *12* (9), 827–835.

(39) Dixit, M.; Markovsky, B.; Schipper, F.; Aurbach, D.; Major, D. T. Origin of Structural Degradation during Cycling and Low Thermal Stability of Ni-Rich Layered Transition Metal-Based Electrode Materials. *J. Phys. Chem. C* **2017**, *121* (41), 22628–22636.

(40) Noh, H.-J.; Youn, S.; Yoon, C. S.; Sun, Y.-K. Comparison of the Structural and Electrochemical Properties of Layered $Li[Ni_xCo_yMn_z]O_2$ (x = 1/3, 0.5, 0.6, 0.7, 0.8 and 0.85) Cathode Material for Lithium-Ion Batteries. *J. Power Sources* **2013**, *233*, 121–130.

(41) Zhang, S. S.; Jow, T. R.; Amine, K.; Henriksen, G. L. $LiPF_6$-EC-EMC Electrolyte for Li-Ion Battery. *J. Power Sources* **2002**, *107* (1), 18–23.

(42) Koga, H.; Croguennec, L.; Menetrier, M.; Douhil, K.; Belin, S.; Bourgeois, L.; Suard, E.; Weill, F.; Delmas, C. Reversible Oxygen Participation to the Redox Processes Revealed for $Li_{1.20}Mn_{0.54}Co_{0.13}Ni_{0.13}O_2$. *J. Electrochem. Soc.* **2013**, *160* (6), A786–A792.

(43) Jiang, M.; Key, B.; Meng, Y. S.; Grey, C. P. Electrochemical and Structural Study of the Layered, "Li-Excess" Lithium-Ion Battery Electrode Material $Li[Li_{1/9}Ni_{1/3}Mn_{5/9}]O_2$. *Chem. Mater.* **2009**, *21* (13), 2733–2745.

(44) La Mantia, F.; Rosciano, F.; Tran, N.; Novák, P. Direct Evidence of Oxygen Evolution from $Li_{1+x}(Ni_{1/3}Mn_{1/3}Co_{1/3})_{1-x}O_2$ at High Potentials. *J. Appl. Electrochem.* **2008**, *38* (7), 893–896.

(45) Armstrong, A. R.; Holzapfel, M.; Novak, P.; Johnson, C. S.; Sun-Ho, K.; Thackeray, M. M.; Bruce, P. G. Demonstrating Oxygen Loss and Associated Structural Reorganization in the Lithium Battery Cathode $Li[Ni_{0.2}Li_{0.2}Mn_{0.6}]O_2$ Demonstrating Oxygen Loss and Associated Structural Reorganization in the Lithium Battery Cathode. *J. Am. Chem. Soc.* **2006**, *128*, 8694–8698.

(46) Koga, H.; Croguennec, L.; Ménétrier, M.; Mannessiez, P.; Weill, F.; Delmas, C. Different Oxygen Redox Participation for Bulk and Surface: A Possible Global

Explanation for the Cycling Mechanism of $Li_{1.20}Mn_{0.54}Co_{0.13}Ni_{0.13}O_2$. *J. Power Sources* **2013**, *236*, 250–258.
(47) Koga, H.; Croguennec, L.; Ménétrier, M.; Mannessiez, P.; Weill, F.; Delmas, C.; Belin, S. Operando X-Ray Absorption Study of the Redox Processes Involved upon Cycling of the Li-Rich Layered Oxide $Li_{1.20}Mn_{0.54}Co_{0.13}Ni_{0.13}O_2$ in Li Ion Batteries. *J. Phys. Chem. C* **2014**, *118*, 5700–5709.
(48) Wu, L.; Nam, K. W.; Wang, X.; Zhou, Y.; Zheng, J. C.; Yang, X. Q.; Zhu, Y. Structural Origin of Overcharge-Induced Thermal Instability of Ni-Containing Layered-Cathodes for High-Energy-Density Lithium Batteries. *Chem. Mater.* **2011**, *23* (17), 3953–3960.
(49) Gabrisch, H.; Wilcox, J.; Doeff, M. M. TEM Study of Fracturing in Spherical and Plate-like $LiFePO_4$ Particles. *Electrochem. Solid-State Lett.* **2008**, *11* (3), A25–A29.
(50) Mu, L.; Lin, R.; Xu, R.; Han, L.; Xia, S.; Sokaras, D.; Steiner, J. D.; Weng, T.-C.; Nordlund, D.; Doeff, M. M.; et al. Oxygen Release Induced Chemomechanical Breakdown of Layered Cathode Materials. *Nano Lett.* **2018**, *18* (5), 3241–3249.
(51) Shin, Y.; Manthiram, A. Microstrain and Capacity Fade in Spinel Manganese Oxides. *Electrochem. Solid-State Lett.* **2002**, *5* (3), A55–A58.
(52) Yan, P.; Zheng, J.; Gu, M.; Xiao, J.; Zhang, J.-G.; Wang, C.-M. Intragranular Cracking as a Critical Barrier for High-Voltage Usage of Layer-Structured Cathode for Lithium-Ion Batteries. *Nat. Commun.* **2017**, *8*, 14101–14109.
(53) Watanabe, S.; Kinoshita, M.; Hosokawa, T.; Morigaki, K.; Nakura, K. Capacity Fade of $LiAl_yNi_{1-x-y}Co_xO_2$ Cathode for Lithium-Ion Batteries during Accelerated Calendar and Cycle Life Tests (Surface Analysis of $LiAl_yNi_{1-x-y}Co_xO_2$ Cathode Af. *J. Power Sources* **2014**, *258*, 210–217.
(54) Abdellahi, A.; Urban, A.; Dacek, S.; Ceder, G. Understanding the Effect of Cation Disorder on the Voltage Profile of Lithium Transition-Metal Oxides. *Chem. Mater.* **2016**, *28* (15), 5373–5383.
(55) Gilbert, J. A.; Shkrob, I. A.; Abraham, D. P. Transition Metal Dissolution, Ion Migration, Electrocatalytic Reduction and Capacity Loss in Lithium-Ion Full Cells. *J. Electrochem. Soc.* **2017**, *164* (2), A389–A399.
(56) Garcia, J. C.; Bareño, J.; Yan, J.; Chen, G.; Hauser, A.; Croy, J. R.; Iddir, H. Surface Structure, Morphology, and Stability of $Li(Ni_{1/3}Mn_{1/3}Co_{1/3})O_2$ Cathode Material. *J. Phys. Chem. C* **2017**, *121* (15), 8290–8299.
(57) Jarry, A.; Gottis, S.; Yu, Y. S.; Roque-Rosell, J.; Kim, C.; Cabana, J.; Kerr, J.; Kostecki, R. The Formation Mechanism of Fluorescent Metal Complexes at the $Li_xNi_{0.5}Mn_{1.5}O^{4-}\delta$/Carbonate Ester Electrolyte Interface. *J. Am. Chem. Soc.* **2015**, *137* (10), 3533–3539.
(58) Faenza, N. V.; Lebens-Higgins, Z. W.; Mukherjee, P.; Sallis, S.; Pereira, N.; Badway, F.; Halajko, A.; Ceder, G.; Cosandey, F.; Piper, L. F. J.; et al. Electrolyte-Induced Surface Transformation and Transition-Metal Dissolution of Fully Delithiated $LiNi_{0.8}Co_{0.15}Al_{0.05}O_2$. *Langmuir* **2017**, *33* (37), 9333–9353.
(59) Ellis, L. D.; Xia, J.; Louli, A. J.; Dahn, J. R. Effect of Substituting LiBF 4 for LiPF 6 in High Voltage Lithium-Ion Cells Containing Electrolyte Additives. *J. Electrochem. Soc.* **2016**, *163* (8), 1686–1692.
(60) Imhof, R.; Novak, P. Oxidative Electrolyte Solvent Degradation in Lithium-Ion

Batteries: An In Situ Differential Electrochemical Mass Spectrometry Investigation. *J. Electrochem. Soc.* **1999**, *146* (5), 1702–1706.

(61) Markus, I. M.; Lin, F.; Kam, K. C.; Asta, M.; Doeff, M. M. Computational and Experimental Investigation of Ti Substitution in Li1($Ni_xMn_xCo_{1-2x-Y}Ti_y$)O_2 for Lithium Ion Batteries. *J. Phys. Chem. Lett.* **2014**, *5* (21), 3649–3655.

(62) Dogan, F.; Vaughey, J. T.; Iddir, H.; Key, B. Direct Observation of Lattice Aluminum Environments in Li Ion Cathodes $LiNi_{1-y-Z}Co_yAl_zO_2$ and Al-Doped $LiNi_xMn_yCo_zO_2$ via ^{27}Al MAS NMR Spectroscopy. *ACS Appl. Mater. Interfaces* **2016**, *8* (26), 16708–16717.

(63) Kong, F.; Liang, C.; Longo, R. C.; Yeon, D. H.; Zheng, Y.; Park, J. H.; Doo, S. G.; Cho, K. Conflicting Roles of Anion Doping on the Electrochemical Performance of Li-Ion Battery Cathode Materials. *Chem. Mater.* **2016**, *28* (19), 6942–6952.

(64) Wang, Y. X.; Shang, K. H.; He, W.; Ai, X. P.; Cao, Y. L.; Yang, H. X. Magnesium-Doped $Li_{1.2}[Co_{0.13}Ni_{0.13}Mn_{0.54}]O_2$ for Lithium-Ion Battery Cathode with Enhanced Cycling Stability and Rate Capability. *ACS Appl. Mater. Interfaces* **2015**, *7* (23), 13014–13021.

(65) Kam, K. C.; Mehta, A.; Heron, J. T.; Doeff, M. M. Electrochemical and Physical Properties of Ti Substituted Layered Nickel Manganese Cobalt Oxide (NMC) Cathode Materials. *J. Electrochem. Soc.* **2012**, *159* (8), A1383–A1392.

(66) Kam, K. C.; Mehta, A.; Heron, J. T.; Doeff, M. M. Electrochemical and Physical Properties of Ti-Substituted Layered Nickel Manganese Cobalt Oxide (NMC) Cathode Materials. *J. Electrochem. Soc.* **2012**, *159* (8), A1383–A1392.

(67) Wilcox, J.; Patoux, S.; Doeff, M. Structure and Electrochemistry of $LiNi_{1/3}Co_{1/3-y}M_yMn_{1/3}O_2$ (M=Ti, Al, Fe) Positive Electrode Materials. *J. Electrochem. Soc.* **2009**, *156* (3), A192.

(68) Meng, Y. S.; Wu, Y. W.; Hwang, B. J.; Li, Y.; Ceder, G. Combining Ab Initio Computation with Experiments for Designing New Electrode Materials for Advanced Lithium Batteries: $LiNi_{1/3}Fe_{1/6}Co_{1/6}Mn_{1/3}O_2$. *J. Electrochem. Soc.* **2004**, *151* (8), A1134–A1140.

(69) Jiao, L. F.; Zhang, M.; Yuan, H. T.; Zhao, M.; Guo, H.; Wang, W.; Di Zhou, X.; Wang, Y. M. Effect of Cr Doping on the Structural, Electrochemical Properties of $LiLi_{0.2}Ni_{0.2-x/2}Mn_{0.6-x/2}Cr_xO^{-2}$ (X=0, 0.02, 0.04, 0.06, 0.08) as Cathode Materials for Lithium Secondary Batteries. *J. Power Sources* **2007**, *167* (1), 178–184.

Chapter 2. Accelerated Evolution of Surface Chemistry Determined by Temperature and Cycling History in Nickel-Rich Layered Cathode Materials

James D. Steiner,[1] Linqin Mu,[1] Julia Walsh,[1] Muhammad Mominur Rahman,[1] Benjamin Zydlewski,[1] F. Marc Michel,[2] Huolin L. Xin,[3] Dennis Nordlund,[4] Feng Lin[1].*

1. Department of Chemistry, Virginia Tech, Blacksburg, VA 24061, USA
2. Department of Geosciences, Virginia Tech, Blacksburg, VA 24061, USA
3. Center for Functional Nanomaterials, Brookhaven National Laboratory, Upton, NY 11973, USA
4. Stanford Synchrotron Radiation Lightsource, SLAC National Accelerator Laboratory, Menlo Park, CA 94035, USA

This chapter was submitted and accepted for publication in *ACS Applied Materials and Interfaces* **DOI:** 10.1021/acsami.8b06399.[1] The manuscript is formatted for this publication.

James Steiner analyzed the data and wrote the manuscript. Dr. Feng Lin directed the project and provided guidance on the data and manuscript. James Steiner additionally performed the synthesis, performance testing, and data characterization. Undergraduates Julia Walsh and Benjamin Zydlewski assisted with the synthesis. Muhammad Mominur Rahman and Dennis Nordlund collected the soft XAS data at SLAC National Accelerator

Laboratory. Dr. Linqin Mu assisted with TEM acquisition. F. Marc Michel assisted with XRD acquisition. Finally, Huolin L. Xin collected the STEM-EELS data.

2.1. Abstract

Nickel-rich layered cathode materials have the potential to enable cheaper and higher energy lithium ion batteries. However, these materials face major challenges (*e.g.,* surface reconstruction, micro-cracking, potential oxygen evolution) that can hinder the safety and cycle life of lithium ion batteries. Many studies of nickel-rich materials have focused on ways to improve performance. Understanding the effects of temperature and cycling on the chemical and structural transformations is essential to assess the performance and suitability of these materials for practical battery applications. The present study is focused on the spectroscopic analysis of surface changes within a strong performing $LiNi_{0.8}Mn_{0.1}Co_{0.1}O_2$ (NMC811) cathode material. We found that surface chemical and structural transformations (*e.g.,* gradient metal reduction, oxygen loss, reconstruction, dissolution) occurred quicker and deeper than expected at higher temperatures. Even at lower temperatures, the degradation occurred rapidly and eventually matched the degradation at high temperatures. Despite these transformations, our performance results showed that a better performing nickel-rich NMC is possible. Establishing relationships between the atomic, structural, chemical, and physical properties of cathode materials and their behavior during cycling, as we have done here for NMC811, opens the possibility of developing lithium ion batteries with higher performance and longer life. Finally, our study also suggests that a separate, systematic and elaborate study of surface chemistry is necessary for each NMC composition and electrolyte environment.

2.2. Introduction

Electrochemical energy storage has revolutionized consumer electronics and penetrated into transportation and stationary electricity storage.[2] The lithium ion battery technology remains the top practical choice for these applications, although beyond lithium ion concepts have also received considerable attention.[3,4] In a lithium ion battery cell, a cathode and an anode work concurrently as lithium ions and electrons travel in between the two electrodes, where the dynamic evolution of electronic and crystal structures takes place.[3,5] The reversible ionic and electronic interaction with electrode materials creates an electrochemical potential for the cell that can be used to power electrical devices.[6] While the lithium ion battery technology has experienced rapid growth, especially with high-capacity silicon/graphite composite anodes,[7–9] there are still challenges associated with the cathode chemistry, such as lower practical energy density.

One of the most practically viable cathodes involves intercalating metal oxide materials.[5] These materials include olivine $LiFePO_4$,[10,11] variants of spinel $LiMn_2O_4$,[12,13] and variants of layered $LiCoO_2$,[14] and usually exhibit well defined lithium hosting sites in crystal lattices, which allows for efficient lithium diffusion. Nickel-rich layered $LiNi_{1-x-y}Mn_xCo_yO_2$ ($1-x-y \geq 0.5$, NMC) cathode materials represent the most promising class of low-cost and high gravimetric energy cathode materials for both conventional lithium ion batteries and solid-state batteries.[15,16] Compared with their "nickel-poor" counterparts, such as $LiNi_{0.4}Mn_{0.4}Co_{0.2}O_2$,[17,18] nickel-rich NMC materials can deliver higher discharge capacities at lower voltages because of the improved accessibility of cationic redox activity.[15,19] Consequently, one can lower the upper cutoff voltages for cells containing

nickel-rich layered cathode materials to avoid undesired electrolyte decomposition while not sacrificing energy density.[20,21]

Pristine nickel-rich NMC materials contain nickel cations with formal oxidation states higher than Ni^{2+}, which introduces a high concentration of hole states in the transition metal (TM)–oxygen (O) octahedral unit.[22,23] Due to the hybridization between TM*3d* and O*2p* orbitals in NMC materials, hole states in the TMO_6 octahedral unit partly reside on the O*2p* orbitals, which activates oxygen anions and can potentially lead to drastic TM–O reactivity during material storage and electrochemical cycling.[22] A thin layer of rock-salt structured metal oxide (surface reconstruction) can rapidly form at the surfaces of nickel-rich NMC materials upon storage in air or inert atmosphere, which is attributable to lithium and oxygen loss (Li_2CO_3 is a common side product because of the Lewis basicity of NMC surfaces). Upon charging and discharging, the surface reconstruction becomes increasingly severe, particularly at high voltages, where extensive oxidation of nickel cations and oxygen anions takes place.[20] Along with other side reactions (*e.g.*, metal dissolution,[24] electrolyte decomposition[25–27]), surface reconstruction leads to rapid impedance buildup and capacity fading.[20,28] Furthermore, extensive oxygen loss introduces local stress in cathode particles and results in the formation of microcracks in primary and secondary particles.[19,29] Collectively, these phenomena lead to, not only predictable battery failure (*e.g.*, energy fading, shortening cycle life), but also catastrophic random events such as battery fire and explosion.

On the other hand, the promise of lithium solid-state batteries delivering volumetric energy density higher than conventional lithium ion batteries carries a few caveats.[30] For example, the areal mass loading of cathode materials must be increased

(preferably above 6 mAh/cm^2), nickel-rich NMC cathodes should be favored over other cathode materials, and the thickness of solid electrolyte must be significantly reduced (preferably below 20 μm). These requirements impose enormous challenges on the cathode chemistry. Charging and discharging these solid-state batteries becomes inefficient and problematic at high current densities and low temperature because of the internal polarization of a thick cathode and poor interfacial charge transfer between a cathode and a solid electrolyte.[31,32] To circumvent these barriers, one can elevate the operating temperature of solid state batteries and/or maintain a small reservoir of liquid electrolyte on the cathode side.[32] However, this inevitably introduces complexities to the cathode–electrolyte interfacial chemistry, particularly at elevated operating temperatures. Therefore, it is critical to understand and improve the surface chemistry of cathode materials operated at different temperatures.

In this study, we first synthesized a nickel-rich NMC material (*i.e.*, $LiNi_{0.8}Mn_{0.1}Co_{0.1}O_2$, NMC811) that outperformed the reported NMC811 materials in major performance metrics, including practical discharge capacity, voltage stability, rate capability, and cycle life. We also conducted a thorough investigation on the cathode–electrolyte interfacial chemistry for cells cycled at different temperatures, various states of charge (SOCs), and different cycle numbers. We observed that the surface of NMC811 materials undergo significant reconstruction upon cycling and becomes exponentially severe during later cycles and at elevated temperatures. Our results indicated that transition metal dissolution likely takes place already during initial cycles, which also deteriorates at elevated temperatures. Furthermore, our results showed that cycling at lower temperatures delays the surface reconstruction to later cycles but cannot eliminate

the phenomena. This suggests that nickel-rich cathode materials require more delicate controls of electrolyte additives (beyond single additive systems) and cathode–electrolyte interfacial engineering.

2.3. Results and Discussion

The knowledge of nickel-rich NMC materials centers along the understanding that the increase in nickel content causes more reactions with the electrolyte,[25] surface reconstruction,[20] microcracking,[29] and low thermal stability.[33] However, nickel provides the cathode with a higher usable capacity that could allow for more efficient and powerful batteries, if the cycle life and safety of the battery could be improved. We are focused on improving and understanding NMC811, which includes monitoring the effects of varying SOCs and cycling temperatures on the chemical and structural transformations at the surface and in the bulk of active particles and ultimately on the battery performance. Other groups have studied the degradation of NMC811 theoretically and experimentally through microcrack generation,[34,35] and degradation of the cathode through electrolyte reactions with the delithiated cathode.[36] In comparison, our research uses ensemble-averaged surface sensitive techniques to probe different depths of the particles as a result of temperature and cycling history.

2.3.1. Characterization of Pristine NMC811

Scanning electron microscopy (SEM) imaging of the pristine NMC811 showed irregular secondary particle morphologies (**Figure 2-1a**). Irregular and relatively high surface area NMC particles were chosen over larger secondary particles to maximize signals associated with surface chemical and structural changes during earlier cycles.

Energy dispersive spectroscopy (EDS) showed that the resulting NMC811 material had an average composition of $Ni_{0.8}Mn_{0.09}Co_{0.11}$, close to the nominal stoichiometry (**Figure A-1**). Transmission electron microscopy (TEM) imaging and X-ray diffraction (XRD) showed that the pristine NMC811 material had the expected O3 layered structure with a $R\bar{3}m$ space group (**Figures 2-1b** and **1c**). Fast Fourier Transformation (FFT) of the TEM image further indicates the layered structure of the particle (**Figure A-2**). According to the surface sensitive TM L-edge soft XAS (**Figure 2-1d**), the manganese had an oxidation state of Mn^{4+} and the cobalt was Co^{3+}.[37] Nickel, however, was a mixture of Ni^{2+} and Ni^{3+}.[37,38] We expected nickel to have an oxidation state closer to Ni^{3+} for NMC811 according to typical charge balance; however, the preparation of the electrodes resulted in some nickel reduction on the surface. The pre-edge peak, at around 530 eV, in the O K-edge soft XAS was associated with the TM3d–O2p hybridization. The intensity of this peak was weaker than what would be expected for NMC811 because of the surface Ni reduction during the electrode processing.

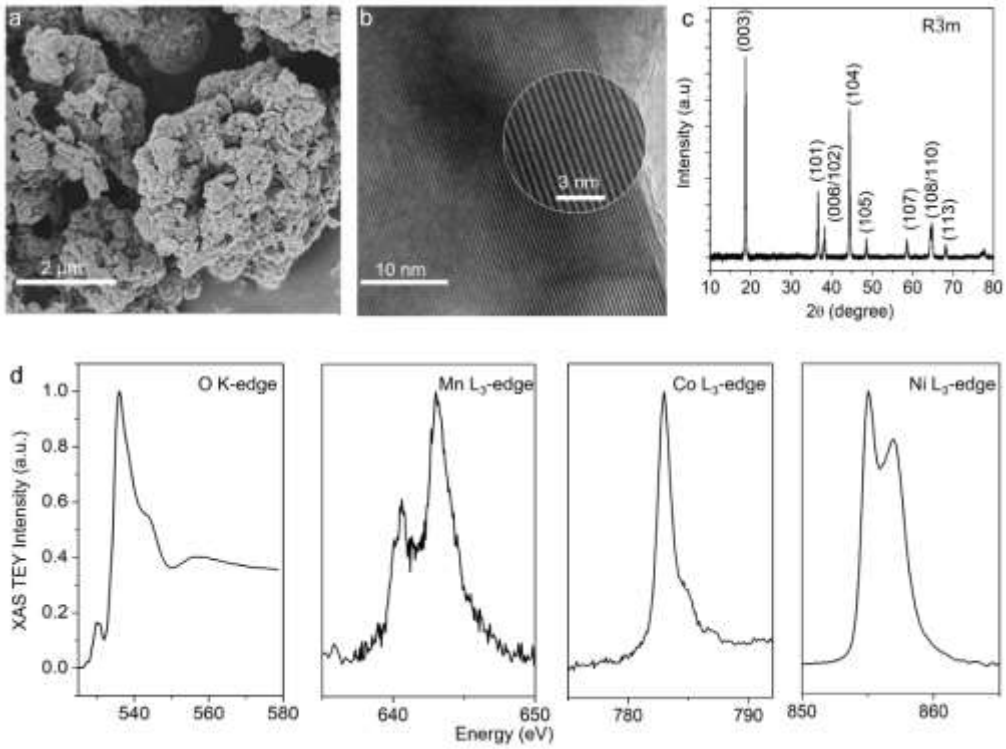

Figure 2-1. (a) SEM image of pristine NMC811 powder, (b) TEM image of pristine NMC811, (c) XRD pattern of pristine NMC811 powder, and (d) surface sensitive soft XAS spectra of pristine NMC811 electrode in the TEY mode (O K-edge, Mn L_3-edge, Co L_3-edge, and Ni L_3-edge).

2.3.2. Electrochemical Performance of NMC811

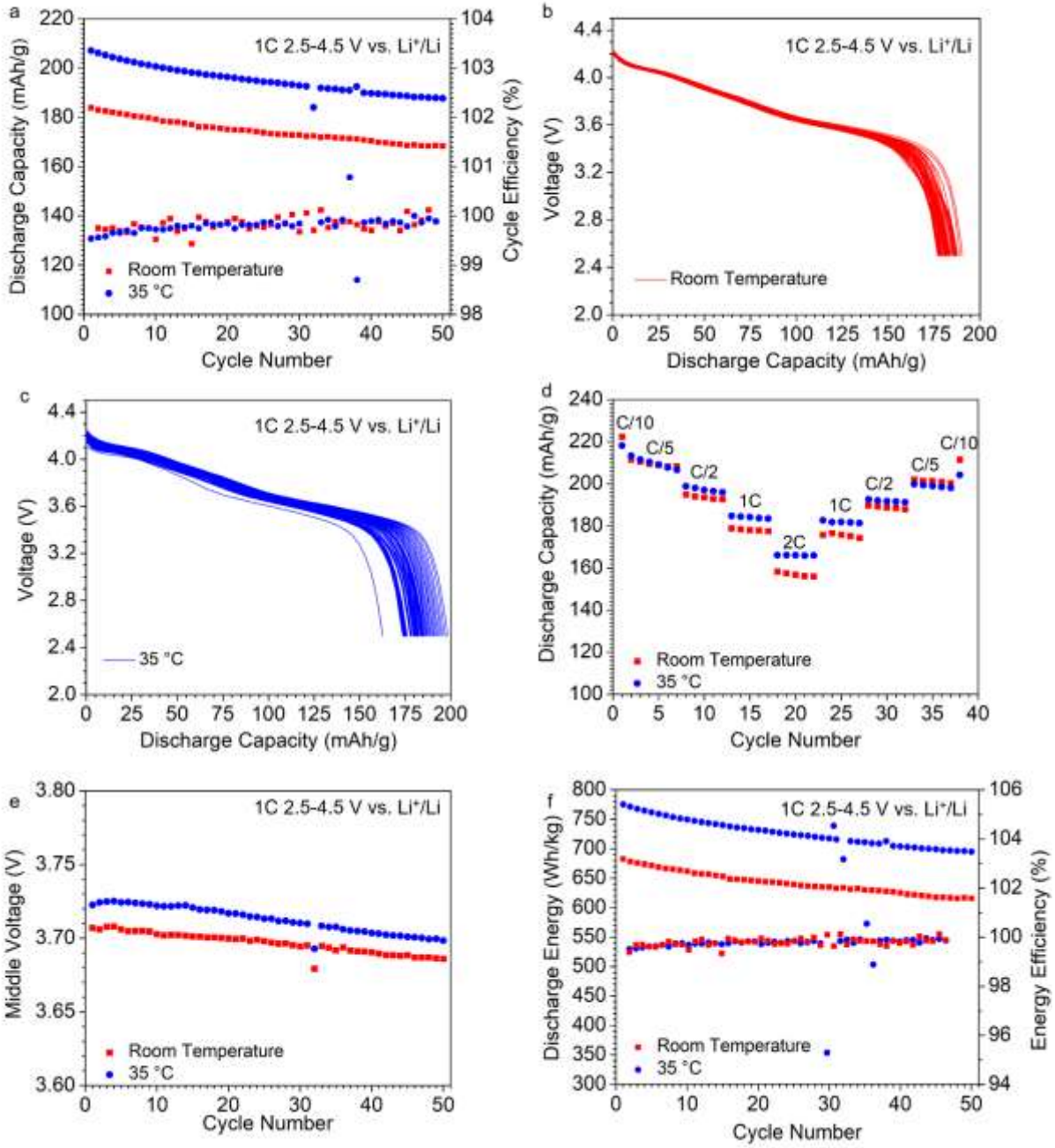

Figure 2-2. Electrochemical performance of cells containing NMC 811. (a) Discharge capacities and Cycle efficiencies for 50 cycles at 1C between 2.5-4.5 V vs. Li^+/Li at room temperature and 35 °C, (b) discharge curves for 50 cycles at 1C at room temperature, (c) discharge curves for 50 cycles at 1C at 35 °C, (d) discharge capacities at various C rates at room temperature and 35 °C, (e) The voltage for 50% of the discharge capacity

(middle voltage) for 50 cycles at 1C at room temperature and 35 °C, and (f) specific energy and energy efficiency for 50 cycles at 1C at room temperature and 35 °C. The discharge capacity in this figure refers to specific discharge capacity. Cycle efficiency refers to the percentage of the discharge capacity retained from cycle to cycle. The active mass loading for electrodes was 4.3 ± 0.1 mg/cm^2.

We first investigated the electrochemical performance of cells containing the NMC811 material to verify that we had a strong cathode material for studying chemical and structural transformations at the surface. Thus, we cycled the cells at room temperature and 35 °C for 50 cycles at 1C between 2.5-4.5V *versus* Li^+/Li. As shown in **Figure 2-2a**, the higher temperature yielded initially higher average discharge capacity (207.1 mAh/g at 35 ºC and 183.5 mAh/g at room temperature), but also led to slightly faster capacity fading. After 50 cycles, the capacity retentions were 91.5% and 87.6% at room temperature and 35 °C, respectively. The overall specific discharge capacities and capacity retentions at high voltage were superior to values reported in the literature,[16,36,39] and represented a strong performing cathode. The areal specific loading here was comparable to those used for NMC811 in the literature.[16] Representative discharge curves showed that the cell cycled at 35 °C exhibited a larger voltage drop due to more extensive buildup of cell polarization (compare **Figures 2-2b** and **c**). Lithium diffusion was accelerated at higher temperature, which allowed for higher initial capacities. However, the increased temperature caused other issues (*e.g.*, quicker surface nickel reduction) that prevented diffusion over time, causing a shorter cycle life than at room temperature. Furthermore, we cycled the cells at varying charging rates (rate capability test) and at different temperatures to understand the effects of extreme cycling and

temperatures. After the 38 cycles of the rate capability test, the C/10 capacity at room temperature surpassed that at 35 °C (**Figure 2-2d**). It is likely that the high temperature and drastic change of charging rates caused more cathode–electrolyte side reactions and surface changes that degraded the cathode faster than room temperature. For instance, after the rate capability test, the cell cycled at room temperature had maintained 95.1% of the initial capacity, while the one cycled at 35 °C had maintained 93.6% (**Figure 2-2d**). These retentions were much higher than those reported in the literature at lower voltages and temperatures.[36,39] Furthermore, we included a 5C charging/discharging rate during the rate capability test and observed that the discharge capacity still remained reversible after the full test protocol (**Figure A-3d**). The 5C cycling using the regular extended cycling resulted in a discharge capacity of 145 mAh/g (**Figure A-3e**).

Finally, a comparison of the middle voltages and specific energy were analyzed at room temperature and 35 °C (**Figures 2-4e** and **f**). The middle voltage, defined as the voltage when half of the discharge capacity is achieved, allowed us to monitor voltage drops due to the growth of cell polarization. There was a negligible difference in voltage retention after 50 cycles (99.43% at 35 °C and 99.35% at room temperature). In addition, the specific discharge energy showed that the energy density decreased more over time at 35 °C, although Coulombic and energy efficiencies stayed nearly identical between the cells cycled at two temperatures throughout the cycles (**Figures 2-4a** and **f**). We also performed performance evaluation at 45 °C (**Figure A-3**). The cells cycled at 45 °C showed similar deterioration as the ones cycled at 35 °C with an overall specific discharge capacity retention of 86.7% after 50 cycles at 1C.

2.3.3. Chemical and Structural Evolution of NMC811 Materials after Cycling

Next, we evaluated the chemical and structural evolution of the battery electrodes to identify the origin of capacity fading at different temperatures. Failures can originate from various components of the cell at different length scales including, but not limited to, electrode, electrolyte, and active particles. Temperature plays a significant role in battery performance and fading.[40] To observe the most salient differences in chemical and structural evolution at different temperatures, the subsequent spectroscopic and imaging investigation were based on the direct comparison between electrodes cycled at room temperature and 45 °C. The capacity fading in **Figure 2-2a** showed a nearly linear behavior, with no sudden "diving" phenomenon. Thus, the fading can be attributed to the cumulative effects of side reactions in the cell. The SEM images showed a low and high magnification of the electrodes before and after cycling (**Figure 2-3**). SEM can provide insight into the morphology and overall packing of particles in the electrodes. The first cycles did not drastically alter the morphology or distribution of active particles and carbon additive in the electrodes, regardless of the applied temperature. To probe the nanometric surface changes for electrodes as functions of SOC and temperature, we applied spatially resolved and ensemble-averaged analytical techniques.

The element specific nature of soft XAS, along with its varying probing depth by tuning the detection mode, allows for probing electronic structures at the surface and in the bulk of each element in NMC materials.[22,41] Given the experimental configuration used in the present study, the probing depths of the soft XAS were: total electron yield (TEY) for 5-10 nm, and fluorescence yield (FY) for 50-100 nm.[20,22,42] Thus TEY allowed for probing any changes directly at the surface, which helped observe surface reconstruction as well as TM reduction and re-deposition. FY helped analyze changes

from the surface into the bulk of the material. In soft XAS the TM L-edge represents when 2p electrons are excited into unoccupied 3d states, while the oxygen K-edge is when 1s electrons are excited into the higher states.[22,43]

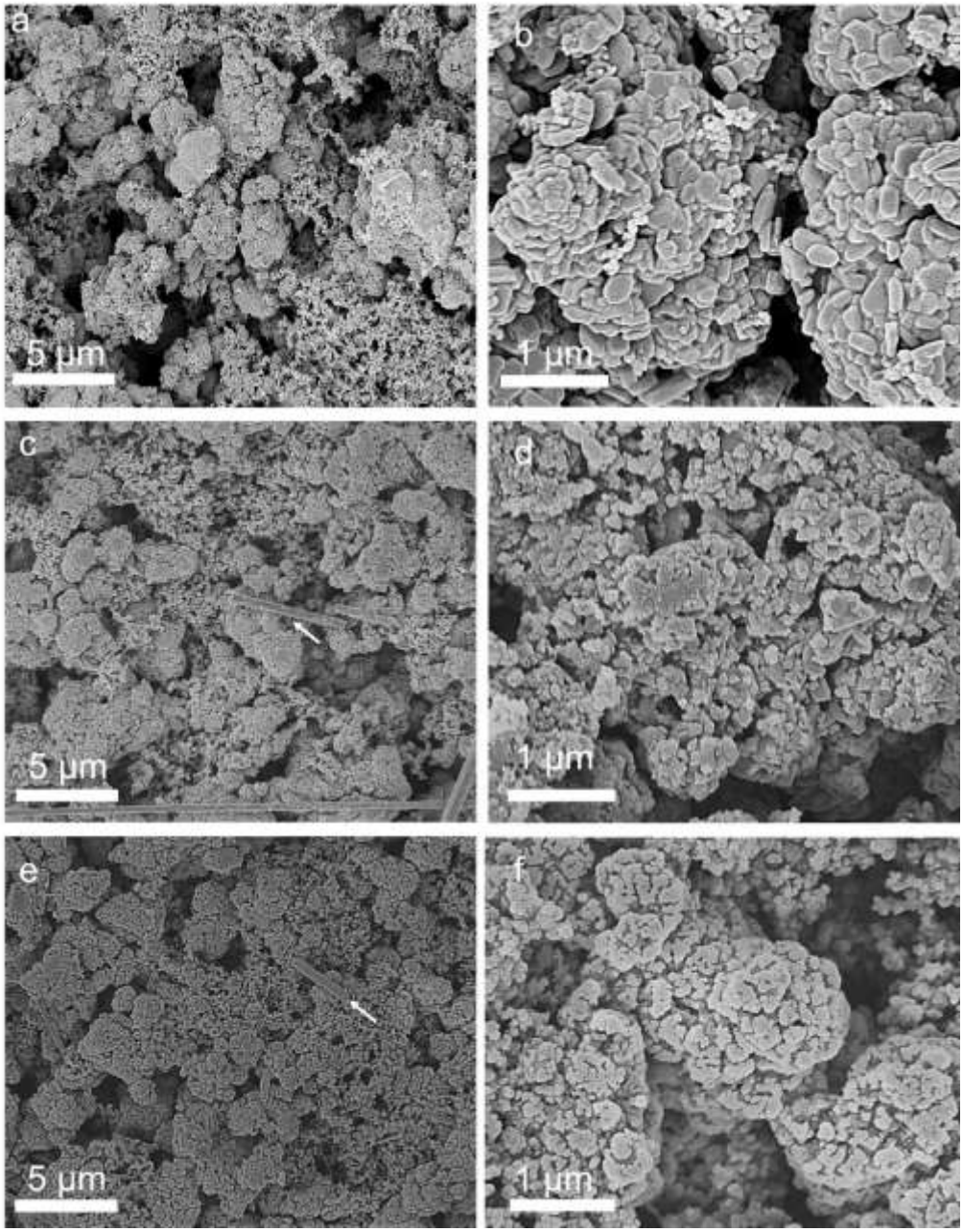

Figure 2-3. SEM images of (a-b) the pristine electrode, (c-d) the electrode after the second cycle at C/10 at room temperature. (e-f) the electrode after the second cycle at

C/10 at 45 ºC. Note that the electrodes were not calendared in this study. The arrows in (c) and (e) point to glass fibers located in the cycled electrodes that originated from the glass fiber separators in the cells.

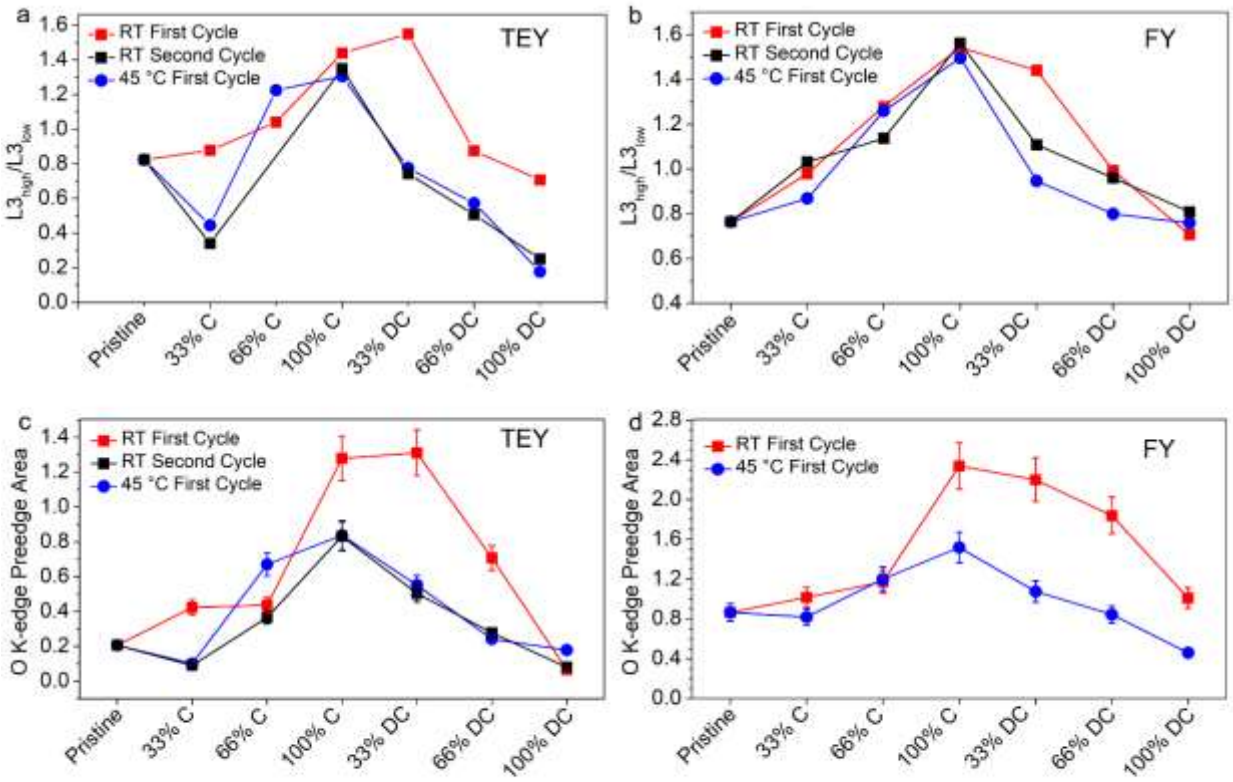

Figure 2-4. Soft XAS quantification of nickel L_3 edge and the oxygen K-edge at varying states of charge where (a) represents the TEY of nickel showing the ratio of the L_3 peaks, (b) represents the FY data of nickel showing the ratio of the L_3 peaks, (c) represents the TEY of the oxygen K-edge with the integrated area of the pre-edge TM3d–O2p peak, and (d) represents the FY data of the oxygen K-edge with integrated area of the pre-edge TM3d–O2p peak. The XAS spectra and description of quantification method are shown in the Supporting Information **Figures A-4** and **A-5**. Due to the technical limitation, the

ex situ measurements could lead to some degree of cell-to-cell variation. Because of taking the area of the O K-edge pre-edge peak, there is a potential error of ± 10%.

We chose to study surface chemistry during the initial cycles so that the soft XAS signal was less contaminated by the electrolyte decomposition products (organic–inorganic composites) and predominantly originated from cathode particles. We compared the ratio of heights in the two peaks in the Ni L_3-edge, where the ratio was the higher energy peak intensity divided by the lower energy peak intensity (defined as γ), and a larger γ represents a higher nickel oxidation state. Such a data reduction process allowed for semi-quantitative analysis of metal oxidation states. We compared the surface and bulk using TEY and the FY (**Figures 2-4a-b**). According to the charge compensation mechanism, nickel should have oxidized during charging and reduced during discharging. However, the TEY data showed that this only applied to room temperature cycling during the first cycle (**Figure 2-4a**). At 45 °C and the second cycle at room temperature, the initial charging caused a drop in the γ value (33% charged in **Figures 2-4a**), indicating that the nickel was reduced rather than oxidized at the surface. When nickel moves from a layered structure into a rock-salt structure it reduces to the Ni^{2+} oxidation state.[20] Thus, we interpreted the observed chemical changes in NMC811 as an indication of surface reconstruction. The results also showed that these changes became more severe with increased temperature and cycle numbers.

As charging continued, the nickel was oxidized in all three samples, which is consistent with the charge compensation during delithiation. Then, as discharging occurred, nickel reduction began. This was quicker at high temperature as the lithium diffusion was faster. Furthermore, after the first complete cycle at 45 °C and the second

complete cycle at room temperature, nickel was more reduced compared to the pristine state (**Figure 2-4a**), indicating a permanent reduction due to the reconstruction from the layered structure to a spinel/rock-salt structure. This permanent reduction could cause impedance growth and capacity fading. The trends showed that the surface changed quickly at high temperature, likely from the greater rate of side reactions with the electrolyte. However, the second cycle at room temperature showed that even at the lower temperature, the side reactions caught up to the level of deterioration observed at high temperature as more cycles were applied. In NMC materials with lower nickel concentrations (e.g., NMC442), the surface reconstruction from a layered structure to a mixed rock-salt/spinel structure only occurs at the surface, in particular when the cycle number is within tens of cycles.[20] This rule also applied to the NMC811 material as the γ values were consistently smaller in TEY than those in FY for all SOCs (compare **Figures 2-4a** and **b**).

In addition to the changes observed with the nickel L-edge we found similar trends in the pre-edge intensity of the oxygen K-edge, namely, TM3d–O2p hybridization (**Figure 2-4c**). The TM3d–O2p intensity changed concurrently as the nickel oxidation state evolved. We conjecture that the activated TM3d–O2p hybridization accelerated the oxygen loss from the surface of NMC811 particles. The initial reduction observed by the TEY mode became less obvious than the FY mode, which implied that the reduction indeed only occurred at the surface, and that only the surface lost the layered characteristics. Notably, the FY of the 45 °C for the oxygen K-edge had a lower final area than its pristine peak, which showed that oxygen is lost deeper than expected at the

higher temperature, likely due to deeper and quicker side reactions of the electrolyte with the cathode particles.

Surface changes occurred as the electrolyte reacted with the surface more rapidly at high temperatures and after prolonged cycling. The nickel and oxygen in the lattice were concurrently oxidized mainly due to orbital hybridization and were different from oxygen redox activity in lithium rich materials. Oxidized oxygen causes oxidation of the electrolyte, which results in the transfer of oxygen to the electrolyte, followed by the nickel reduction to compensate for the oxygen loss. Increasing the temperature accelerated the kinetics of the changes and the rate of rock-salt/spinel formation on the cathodes surface. Changing the temperature is not an ultimate solution to mitigate the surface reconstruction, it just delays the degradation for a short time. This suggests that future work aimed at limiting degradation and surface reconstruction should focus on optimizing the surface chemistry of the pristine cathode.

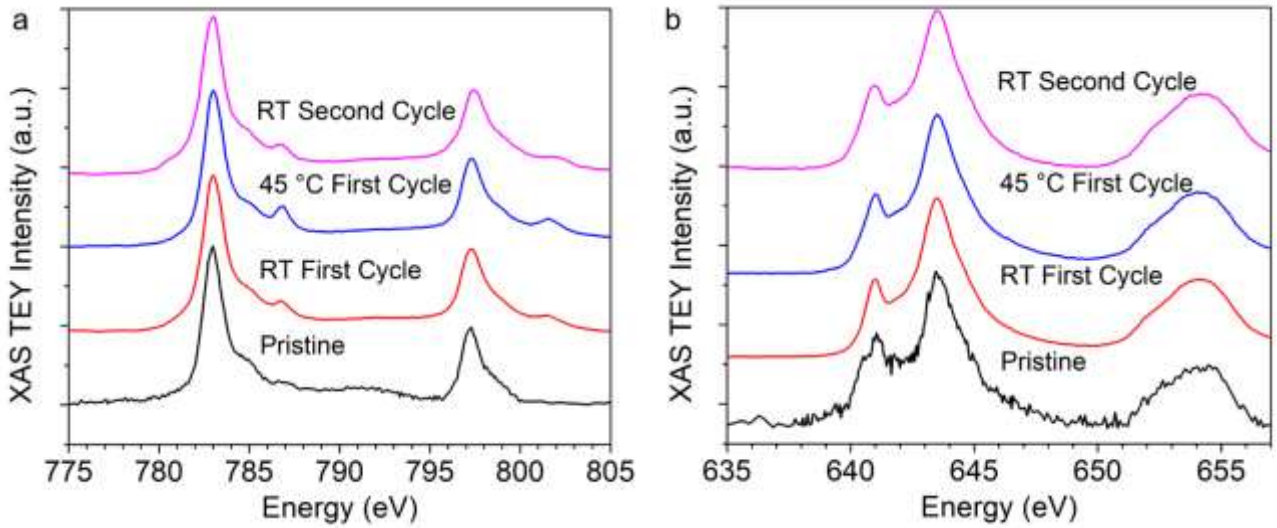

Figure 2-5. Soft XAS showing the TEY data for (a) Co L-edge (b) Mn L-edge at the 66% discharged state, where the pristine Co L-edge and Mn L-edge are shown for direct comparison.

Cobalt at the surfaces of NMC811 were also susceptible to changes during cycling. We compared the TEY data of the 66% discharge state for all three samples with the pristine sample.

The cobalt did not undergo significant oxidation state changes. However, at around 786 eV, a new peak formed in the cobalt L-edge XAS (**Figure 2-5a**). This peak was attributed to individual cobalt cations that are bonded to organic functional groups,[44] although it is still under debate. In our system, this peak is likely attributed to the cobalt dissolution from the cathode lattice to the cathode–electrolyte interphase. The cobalt dissolution was more prominent at the higher temperature, which coincided with the changes observed in nickel and oxygen. The metal dissolution happened earlier than expected and could pose additional unseen problems in NMC811 cathode materials. Direct comparison between 66% discharged and 100% charged (**Figure A-6**), we found that the potential Co dissolution likely took place more during the discharging process.

Thus, future work may include limiting dissolution to stabilize the cathode particles. Manganese, on the other hand, did not show discernible oxidation state change at this SOC from the pristine oxidation states observed in **Figure 2-1**.

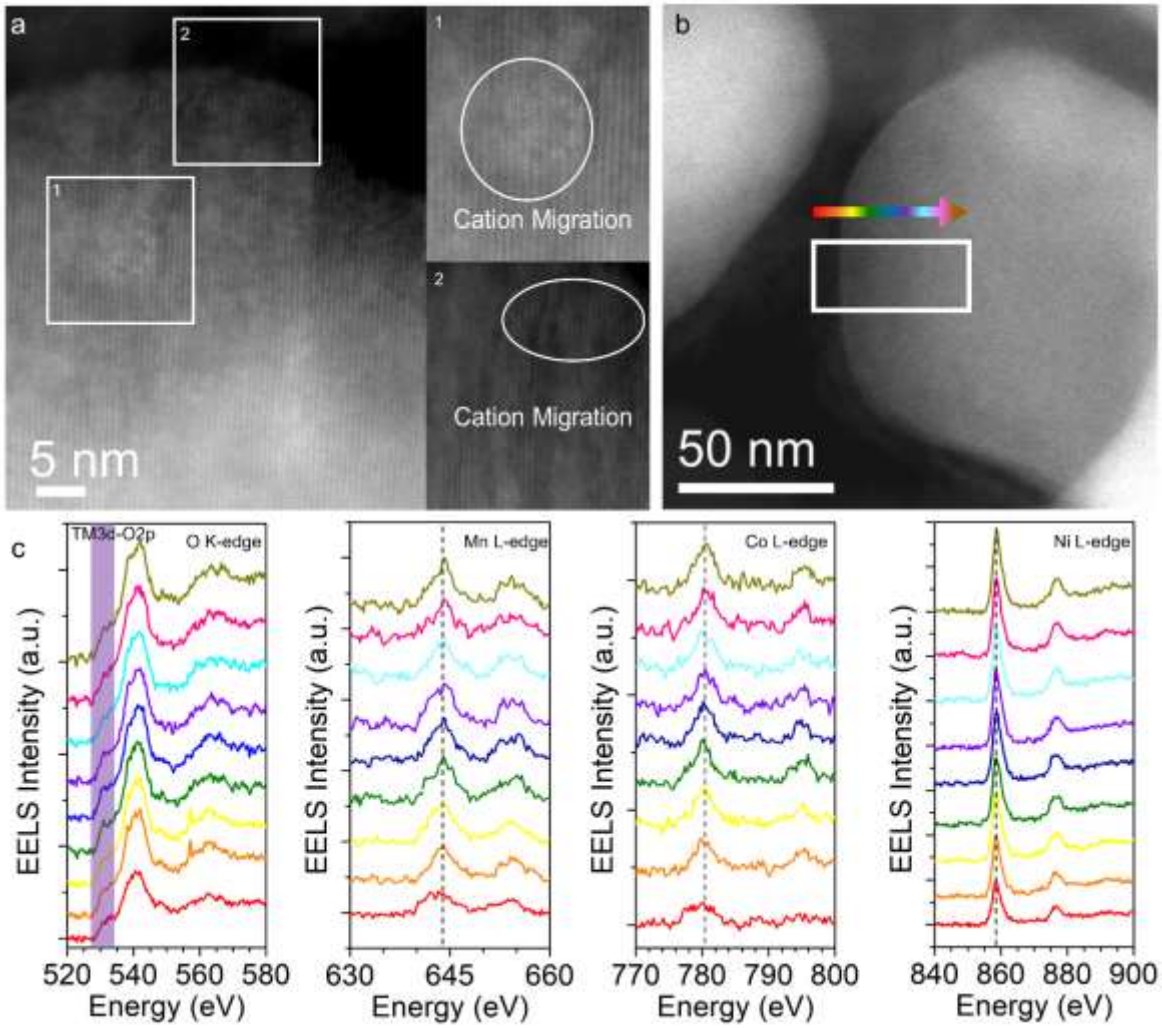

Figure 2-6. (a) STEM image of a fully discharged 45 °C NMC811 particle after one cycle that shows surface reconstruction, (b) the area of the particle that was analyzed for EELS, and (c) the EELS spectra of the transition metal L-edges and oxygen K-edge, where the TM3d–O2p hybridization is labeled in (c). The EELS probed gradually deeper from the bottom to the top in (c).

To better understand the surface changes, we performed STEM-EELS on a fully discharged cathode after one cycle (**Figure 2-6**). STEM allowed for observing any surface reconstruction that could affect the cycle life such as rock-salt/spinel formation or

pores. (**Figure 2-6a**). FFT of the STEM image showed the presence of layered and rock salt structure in the lattice (**Figures A-7 and A-8)**.

We then performed EELS for cathode particles from surface to bulk to understand the electronic structure of the individual particle (the representative results are shown in **Figures 2-6b** and **c**). The oxygen K-edge had no obvious pre-edge peak related to the TM3d–O2p hybridization (**Figure 2-6b**). If there were still NMC811 layered structure at the surface, there would be a strong pre-edge peak. In addition, the intensity did not increase as the probing got deeper into the bulk. The EELS L-edges for all three TMs did not experience peak shift from the surface to the bulk (**Figure 2-6c**). These results suggested that there was no longer perfect NMC811 layered structure in the probed area. Therefore, the surface change in NMC811 occurred much deeper than expected and earlier than NMC442 materials.[20] This deeper surface change coincided with the results seen in soft XAS for 45 °C.

2.4. Conclusion

The nickel-rich NMC material $LiNi_{0.8}Mn_{0.1}Co_{0.1}O_2$ is susceptible to surface chemical and structural changes during cycling. The reduction of nickel during cycling correlated with oxygen loss to the electrolyte. Cobalt dissolution to the electrolyte solution also corresponded with oxygen loss. These chemical changes coincided with reconstruction of the particle surfaces to a rock salt/spinel type structure. Higher temperatures and longer cycling compounded the amount of surface change, which caused cell performance to deteriorate. Thus, varying temperatures and cycling conditions are unlikely to fully stabilize cells using a nickel-rich NMC material. The

surface changes may also compound with other fading mechanisms such as electrolyte decomposition and formation of microcracks, which collectively lead to battery failure. This study suggests that nickel-rich materials could provide longer-lasting batteries, but further research into methods of limiting surface oxygen loss are required. The future research should investigate the compatibility of the electrolyte with various engineered surfaces.

2.5. Experimental Methods

2.5.1. Synthesis method

$LiNi_{0.8}Mn_{0.1}Co_{0.1}O_2$ was synthesized through a coprecipitation method in the three-necked round bottom flask. A metal solution of 100 mL with a concentration of 1M was mixed into a 0.8M $NiSO_4 \cdot 6H_2O$ (Sigma Aldrich, 99.99%), 0.1M $MnSO_4 \cdot H_2O$ (Sigma Aldrich, 99%) and 0.1M $CoSO_4 \cdot 7H_2O$ (Sigma Aldrich, 99%). The transition metal solution (dissolved in 100 mL H_2O) and base solution (2M NaOH and 1.67 M $NH_3 \cdot H_2O$, total 100 mL aqueous solution) were separately stored in Kimble bottles. The base solution was stored under N_2 protection. The starting solution (1M NaOH and 0.83M $NH_3 \cdot H_2O$, total 160 mL aqueous solution) was placed into a round bottom flask, heated to 50 °C, stirred constantly at approximately 800 rpm, and the pH value was adjusted to 10.5 using H_2SO_4. The solution was continuously stirred at constant temperature as the transition metal and base solutions were pumped into the starting solution at approximately 2 mL/min. The pH was held constantly at 10.5±0.1 by tuning the base solution frequently. The precipitate was collected, washed with 400 mL DI water and then 400 mL of isopropanol, and finally filtrated and then dried in a vacuum oven overnight at 95 °C. The dried precursor was then mixed with LiOH (3% extra was added

to compensate for Li loss) thoroughly and calcined under pure oxygen flow at 0.5 L/min. The sample was heated at 5 °C/min to 460 °C and held there for 1 hour. Then the sample was heated at 5 °C/min to 725 °C and remained there for 6 hours. Finally, the furnace was cooled at 5 °C/min to 25 °C still under constant oxygen flow to obtain the final $LiNi_{0.8}Mn_{0.1}Co_{0.1}O_2$ powder.

2.5.2. Electrode Preparation:

Electrodes were prepared using 90% active material, 5% polyvinylidene fluoride, and 5% acetylene carbon black in N-methyl-2-pyrrolidone and then cast onto carbon coated aluminum foil current collectors. The electrodes were dried under vacuum at 120 °C. The electrodes have a loading capacity of 4.3 ± 0.1 mg/cm^2. CR2032-type coin cells were assembled in an argon-filled glovebox using the electrode as the cathode and lithium metal as the anode. The cathode and anode were separated with a glass fiber separator which was soaked with an electrolyte of 1 M $LiPF_6$ dissolved in a 3:7 ratio of EC/EMC with 2wt% VC. All the electrochemical testing was performed using a LAND battery testing system. 1C was defined as fully charging the cathode in one hour, with a specific capacity of 200 mAh/g. The same rate was used for discharging the cathode.

2.5.3. Materials characterization:

Powder XRD was performed in reflection geometry using a PANalytical Empyrean X-ray diffractometer with a Cu K_α (λ=1.54 Å) x-ray source and Bragg-Brentano HD divergent beam optic with an energy resolution of about 450 eV. The incident beam path included a 0.02 rad Soller slit, 10 mm beam mask, fixed antiscatter slit (1/2°) and fixed divergence slit (1/8°). Dry samples were loaded individually onto 32 mm low-background Si wafer samples holders with 0.2 mm wells (Panalytical) and

rotated in place during the analysis. Diffracted intensities were collected from 10 to 80° 2θ in approximately 0.0018° increments using a GaliPIX^{3D} area detector system operating in line mode (501 active channels). The exposure time was approximately 28 sec/point. A 0.02 rad Soller slit was used in the diffracted beam path. A LEO (Zeiss) 1500 with an Oxford INCA Energy E2H X-ray Energy Dispersive Spectrometer (EDS) system with Silicon Drifted detector was used to perform scanning electron microscopy (SEM). A FEI Quanta 600 FEG with Bruker EDX with a Silicon Drifted Detector was used to perform EDS. Soft XAS measurements were performed on the 31-pole wiggler beamline 10-1 at Stanford Synchrotron Radiation Lightsource (SSRL) using a ring current of 350 mA and a 1000 l·mm^{-1} spherical grating monochromator with 20 μm entrance and exit slits, providing ~10^{11} ph·s-1 at 0.2 eV resolution in a 1 mm^2 beam spot. A single load at room temperature in an ultrahigh vacuum (10^{-9} Torr) was used to acquire data using total electron yield (TEY), where the sample drain current was collected, and fluorescence yield (FY), where a silicon diode (IRD AXUV-100) was used to collect the FY positioned near the sample surface. We quantified our nickel XAS data by taking the two L_3 edge peaks and making a ratio of the height of the high energy peak over the height of the low energy peak. We then graphed the ratio vs. the SOC of the battery. For oxygen K-edge we took the area of the pre-edge peak at around 530 eV. We then graphed the areas according to the SOC of the cell. Our scanning transmission microscopy (STEM) and electron energy loss spectroscopy (EELS) were acquired on a JEOL 2100 S/TEM operated at 200 keV.

2.6. References

References

(1) Steiner, J. D.; Mu, L.; Walsh, J.; Rahman, M. M.; Michel, F. M.; Xin, H. L.; Nordlund, D.; Lin, F. Accelerated Evolution of Surface Chemistry Determined by Temperature and Cycling History in Nickel-Rich Layered Cathode Materials. *ACS Appl. Mater. Interfaces* **2018**, *10*(28), 23842–23850.
(2) Dunn, B.; Kamath, H.; Tarascon, J.-M. Electrical Energy Storage for the Grid: A Battery of Choices. *Science* **2011**, *334* (6058), 928–935.
(3) Goodenough, J. B.; Park, K. S. The Li-Ion Rechargeable Battery: A Perspective. *J. Am. Chem. Soc.* **2013**, *135* (4), 1167–1176.
(4) Noorden, R. Van. The Rechargeable Revolution: A Better Battery. *Nature* **2014**, *507*, 26–28.
(5) Whittingham, M. S. Ultimate Limits to Intercalation Reactions for Lithium Batteries. *Chem. Rev.* **2014**, *114* (23), 11414–11443.
(6) Liu, C.; Neale, Z. G.; Cao, G. Understanding Electrochemical Potentials of Cathode Materials in Rechargeable Batteries. *Mater. Today* **2016**, *19* (2), 109–123.
(7) Niu, J.; Lee, J. Y. Improvement of Usable Capacity and Cyclability of Silicon-Based Anode Materials for Lithium Batteries by Sol-Gel Graphite Matrix. *Electrochem. Solid-State Lett.* **2002**, *5* (6), A107–A110.
(8) Chen, P. C.; Xu, J.; Chen, H.; Zhou, C. Hybrid Silicon-Carbon Nanostructured Composites as Superior Anodes for Lithium Ion Batteries. *Nano Res.* **2011**, *4* (3), 290–296.
(9) Yim, C.-H.; Courtel, F. M.; Abu-Lebdeh, Y. A High Capacity Silicon–graphite Composite as Anode for Lithium-Ion Batteries Using Low Content Amorphous Silicon and Compatible Binders. *J. Mater. Chem. A* **2013**, *1* (5), 8234–8243.
(10) Wang, J.; Sun, X. Olivine $LiFePO_4$: The Remaining Challenges for Future Energy Storage. *Energy Environ. Sci.* **2015**, *8* (4), 1110–1138.
(11) Padhi, A. K.; Nanjundaswamy, K. S.; Goodenough, J. B. Phospho-Olivines as Positive-Electrode Materials for Rechargeable Lithium Batteries. *J. Electrochem. Soc.* **1997**, *144* (4), 1188–1194.
(12) Pistoia, G.; Panero, M.; Tocci, M.; Moshtev, R. V. An Investigation of Lithium Ion Insertion into Spinel Structure Li-Mn-O Compounds. *J. Electrochem. Soc.* **1996**, *143* (3), 825–833.
(13) Kanamura, K.; Naito, H.; Yao, T.; Takehara, Z. Structural Change of the $LiMn_2O_4$ Spinel Structure Induced by Extraction of Lithium. *J. Mater. Chem.* **1996**, *6* (1), 33–36.
(14) Mizushima, K.; Jones, P. C.; Wiseman, P. J.; Goodenough, J. B. Li_xCoO_2 ($0<x<1$): A New Cathode Material for Batteries of High Energy Density. *Mater. Res. Bull.* **1980**, *15*, 783–789.
(15) Myung, S.-T.; Maglia, F.; Park, K.-J.; Yoon, C. S.; Lamp, P.; Kim, S.-J.; Sun, Y.-K. Nickel-Rich Layered Cathode Materials for Automotive Lithium-Ion Batteries: Achievements and Perspectives. *ACS Energy Lett.* **2017**, *2* (1), 196–223.
(16) Zheng, J.; Kan, W. H.; Manthiram, A. Role of Mn Content on the Electrochemical Properties of Nickel-Rich Layered $LiNi_{0.8-x}Co_{0.1}Mn_{0.1+x}O_2$ ($0.0 < x < 0.08$) Cathodes for Lithium-Ion Batteries. *ACS Appl. Mater. Interfaces* **2015**, *7* (12), 6926–6934.
(17) Martha, S. K.; Sclar, H.; Szmuk Framowitz, Z.; Kovacheva, D.; Saliyski, N.; Gofer, Y.; Sharon, P.; Golik, E.; Markovsky, B.; Aurbach, D. A Comparative

Study of Electrodes Comprising Nanometric and Submicron Particles of $LiNi_{0.50}Mn_{0.50}O_2$, $LiNi_{0.33}Mn_{0.33}Co_{0.33}O_2$, and $LiNi_{0.40}Mn_{0.40}Co$<sub>0.20</. *J. Power Sources* **2009**, *189* (1), 248–255.

(18) Luo, X.; Wang, X.; Liao, L.; Wang, X.; Gamboa, S.; Sebastian, P. J. Effects of Synthesis Conditions on the Structural and Electrochemical Properties of Layered $Li[Ni_{1/3}Co_{1/3}Mn_{1/3}]O_2$ Cathode Material via the Hydroxide Co-Precipitation Method LIB SCITECH. *J. Power Sources* **2006**, *161*, 601–605.

(19) Liu, W.; Oh, P.; Liu, X.; Lee, M. J.; Cho, W.; Chae, S.; Kim, Y.; Cho, J. Nickel-Rich Layered Lithium Transition-Metal Oxide for High-Energy Lithium-Ion Batteries. *Angew. Chemie - Int. Ed.* **2015**, *54* (15), 4440–4457.

(20) Lin, F.; Markus, I. M.; Nordlund, D.; Weng, T.-C.; Asta, M. D.; Xin, H. L.; Doeff, M. M. Surface Reconstruction and Chemical Evolution of Stoichiometric Layered Cathode Materials for Lithium-Ion Batteries. *Nat. Commun.* **2014**, *5*, 3529.

(21) Jung, S.; Gwon, H.; Hong, J.; Park, K.; Seo, D.; Kim, H.; Hyun, J.; Yang, W.; Kang, K. Understanding the Degradation Mechanisms of $LiNi_{0.5}Co_{0.2}Mn_{0.3}O_2$ Cathode Material in Lithium Ion Batteries. *Adv. Energy Mater.* **2014**, *4* (1), 1300787–1300793.

(22) Lin, F.; Nordlund, D.; Markus, I. M.; Weng, T.-C.; Xin, H. L.; Doeff, M. M. Profiling the Nanoscale Gradient in Stoichiometric Layered Cathode Particles for Lithium-Ion Batteries. *Energy Environ. Sci.* **2014**, *7*, 3077–3085.

(23) Yoon, W. S.; Balasubramanian, M.; Chung, K. Y.; Yang, X. Q.; McBreen, J.; Grey, C. P.; Fischer, D. A. Investigation of the Charge Compensation Mechanism on the Electrochemically Li-Ion Deintercalated $Li_{1-x}Co_{1/3}Ni_{1/3}Mn_{1/3}O_2$ Electrode System by Combination of Soft and Hard X-Ray Absorption Spectroscopy. *J. Am. Chem. Soc.* **2005**, *127* (49), 17479–17487.

(24) Gilbert, J. A.; Shkrob, I. A.; Abraham, D. P. Transition Metal Dissolution, Ion Migration, Electrocatalytic Reduction and Capacity Loss in Lithium-Ion Full Cells. *J. Electrochem. Soc.* **2017**, *164* (2), A389–A399.

(25) Seo, D.; Lee, J.; Urban, A.; Malik, R.; Kang, S.; Ceder, G. The Structural and Chemical Origin of the Oxygen Redox Activity in Layered and Cation-Disordered Li-Excess Cathode Materials. *Nat. Chem.* **2016**, *8* (7), 692–697.

(26) La Mantia, F.; Rosciano, F.; Tran, N.; Novák, P. Direct Evidence of Oxygen Evolution from $Li_{1+x}(Ni_{1/3}Mn_{1/3}Co_{1/3})_{1-x}O_2$ at High Potentials. *J. Appl. Electrochem.* **2008**, *38* (7), 893–896.

(27) Xu, S.; Luo, G.; Jacobs, R.; Fang, S.; Mahanthappa, M. K.; Hamers, R. J.; Morgan, D. Ab Initio Modeling of Electrolyte Molecule Ethylene Carbonate Decomposition Reaction on $Li(Ni,Mn,Co)O_2$ Cathode Surface. *ACS Appl. Mater. Interfaces* **2017**, *9* (24), 20545–20553.

(28) Wu, F.; Tian, J.; Liu, N.; Lu, Y.; Su, Y.; Wang, J.; Chen, R.; Ma, X.; Bao, L.; Chen, S. Alleviating Structural Degradation of Nickel-Rich Cathode Material by Eliminating the Surface $Fm\bar{3}m$ Phase. *Energy Storage Mater.* **2017**, *8*, 134–140.

(29) Yan, P.; Zheng, J.; Gu, M.; Xiao, J.; Zhang, J.-G.; Wang, C.-M. Intragranular Cracking as a Critical Barrier for High-Voltage Usage of Layer-Structured Cathode for Lithium-Ion Batteries. *Nat. Commun.* **2017**, *8*, 14101–14109.

(30) Luntz, A. C.; Voss, J.; Reuter, K. Interfacial Challenges in Solid-State Li Ion Batteries. *J. Phys. Chem. Lett.* **2015**, *6* (22), 4599–4604.

(31) Abraham, D. P.; Twesten, R. D.; Balasubramanian, M.; Petrov, I.; McBreen, J.; Amine, K. Surface Changes on $LiNi_{0.8}Co_{0.2}O_2$ Particles during Testing of High-Power Lithium-Ion Cells. *Electrochem. commun.* **2002**, *4* (8), 620–625.
(32) Han, X.; Gong, Y.; Fu, K.; He, X.; Hitz, G. T.; Dai, J.; Pearse, A.; Liu, B.; Wang, H.; Rubloff, G.; et al. Negating Interfacial Impedance in Garnet-Based Solid-State Li Metal Batteries. *Nat. Mater.* **2017**, *16* (5), 572–579.
(33) Wu, L.; Nam, K. W.; Wang, X.; Zhou, Y.; Zheng, J. C.; Yang, X. Q.; Zhu, Y. Structural Origin of Overcharge-Induced Thermal Instability of Ni-Containing Layered-Cathodes for High-Energy-Density Lithium Batteries. *Chem. Mater.* **2011**, *23* (17), 3953–3960.
(34) Kondrakov, A. O.; Schmidt, A.; Xu, J.; Geßwein, H.; Mönig, R.; Hartmann, P.; Sommer, H.; Brezesinski, T.; Janek, J. Anisotropic Lattice Strain and Mechanical Degradation of High- and Low-Nickel NCM Cathode Materials for Li-Ion Batteries. *J. Phys. Chem. C* **2017**, *121* (6), 3286–3294.
(35) Lim, J.-M.; Hwang, T.; Kim, D.; Park, M.-S.; Cho, K.; Cho, M. Intrinsic Origins of Crack Generation in Ni-Rich LiNi0.8Co0.1Mn0.1O2 Layered Oxide Cathode Material. *Sci. Rep.* **2017**, *7*, 39669.
(36) Li, J.; Downie, L. E.; Ma, L.; Qiu, W.; Dahn, J. R. Study of the Failure Mechanisms of $LiNi_{0.8}Mn_{0.1}Co_{0.1}O_2$ Cathode Material for Lithium Ion Batteries. *J. Electrochem. Soc.* **2015**, *162* (7), A1401–A1408.
(37) Lin, F.; Nordlund, D.; Pan, T.; Markus, I. M.; Weng, T.-C.; Xin, H. L.; Doeff, M. M. Influence of Synthesis Conditions on the Surface Passivation and Electrochemical Behavior of Layered Cathode Materials. *J. Mater. Chem. A* **2014**, *2* (46), 19833–19840.
(38) Wang, H.; Butorin, S. M.; Young, A. T.; Guo, J. Nickel Oxidation States and Spin States of Bioinorganic Complexes from Nickel L-Edge X-Ray Absorption and Resonant Inelastic X-Ray Scattering. *J. Phys. Chem. C* **2013**, *117* (47), 24767–24772.
(39) Zhao, E.; Chen, M.; Hu, Z.; Chen, D.; Yang, L.; Xiao, X. Improved Cycle Stability of High-Capacity Ni-Rich $LiNi_{0.8}Mn_{0.1}Co_{0.1}O_2$ at High Cut-off Voltage by Li_2SiO_3 Coating. *J. Power Sources* **2017**, *343*, 345–353.
(40) Noh, H.-J.; Youn, S.; Yoon, C. S.; Sun, Y.-K. Comparison of the Structural and Electrochemical Properties of Layered Li[NixCoyMnz]O2 (x = 1/3, 0.5, 0.6, 0.7, 0.8 and 0.85) Cathode Material for Lithium-Ion Batteries. *J. Power Sources* **2013**, *233*, 121–130.
(41) Yoon, W.-S.; Haas, O.; Muhammad, S.; Kim, H.; Lee, W.; Kim, D.; Fischer, D. A.; Jaye, C.; Yang, X.-Q.; Balasubramanian, M.; et al. In Situ Soft XAS Study on Nickel-Based Layered Cathode Material at Elevated Temperatures: A Novel Approach to Study Thermal Stability. *Sci. Rep.* **2015**, *4* (1), 6827.
(42) Abbate, M.; Goedkoop, J. B.; de Groot, F. M. F.; Grioni, M.; Fuggle, J. C.; Hofmann, S.; Petersen, H.; Sacchi, M. Probing Depth of Soft X-ray Absorption Spectroscopy Measured in Total-electron-yield Mode. *Surf. Interface Anal.* **1992**, *18* (1), 65–69.
(43) De Groot, F. M. F.; Grioni, M.; Fuggle, J. C.; Ghijsen, J.; Sawatzky, G. A.; Petersen, H. Oxygen 1s X-Ray-Absorption Edges of Transition-Metal Oxides. *Phys. Rev. B* **1989**, *40* (8), 5715–5723.

(44) Liu, H.; Guo, J.; Yin, Y.; Augustsson, A.; Dong, C.; Ogletree, D. F.; Requejo, F. G.; de Groot, F. M. F.; Salmeron, M. Electronic Structure of Cobalt Nanocry Stals Suspended in Liquid. *Nano Lett.* **2007**, *7* (7), 1919–1922.

Chapter 3. Three-Dimensional Substitution of Nickel-rich Cathode Materials Stabilizes Electrochemical Interfaces

James D. Steiner,[1] Hao Cheng, [2,3] Julia Walsh,[1] Yan Zhang,[4] Benjamin Zydlewski,[1] Linqin Mu,[1] Zhengrui Xu,[1] Muhammad Mominur Rahman,[1] F. Marc Michel,[5] Cheng-Jun Sun,[6] Dennis Nordlund,[4] Huolin L. Xin,[7] Feng Lin[1,]*

1. Department of Chemistry, Virginia Tech, Blacksburg, VA 24061, USA
2. Department of Physics and the Collaborative Innovation Center for Optoelectronic Semiconductors and Efficient Devices, Xiamen University, Xiamen 361005, China
3. Xiamen University Malaysia 439000, Sepang, Selangor, Malaysia
4. Stanford Synchrotron Radiation Lightsource, SLAC National Accelerator Laboratory, Menlo Park, CA 94035, USA
5. Department of Geosciences, Virginia Tech, Blacksburg, VA 24061, USA
6. Advanced Photon Source, Argonne National Laboratory, Argonne, Illinois 60439, USA
7. Center for Functional Nanomaterials, Brookhaven National Laboratory, Upton, NY 11973, USA

This chapter is being prepared as a communication to be submitted to a journal, likely a chemistry journal. James Steiner developed the synthesis method, analyzed the data, and wrote the manuscript. He additionally performed the synthesis, sample preparations for all characterization methods, performance testing, and data characterization. Dr. Feng Lin directed the project and provided guidance on the data and manuscript. Hao Cheng and Dr. Jincheng Zheng performed all theoretical calculations for this work. Undergraduates Julia Walsh and Benjamin Zydlewski assisted with the synthesis. Yan Zhang and Dennis Nordlund collected the soft XAS data at SLAC National Accelerator Laboratory. Dr. Linqin Mu, Zhengrui Xu, and Dr. Cheng-Jun Sun collected the hard XAS data at Argonne

National Laboratory. F. Marc Michel assisted with XRD acquisition. Finally, Huolin L. Xin collected the STEM-EELS and STEM-EDS data.

3.1. Abstract.

Stabilization of nickel-rich lithium-ion cathodes presents an important goal within the battery community. Transition metal substitution has been considered as a possible avenue for synthesizing stable, long-lasting cathode materials. Many studies of substitution have focused on the increase in performance and not the actual causes of stability. Understanding the root cause of stabilization is essential to further understanding the best methods to synthesize nickel-rich materials. The current study expands on our degradation knowledge of $LiNi_{0.8}Mn_{0.1}Co_{0.1}O_2$ (NMC811) from our previous work. Here we have substituted 3% titanium into the lattice of the NMC811 through a gradient addition method. We found that the substitution increased capacity retention from 57.81% to 70.27% over 500 cycles. Our novel analysis of the bonding through XAS methods and theoretical analysis demonstrates that the titanium deactivates the oxygen within the lattice due to variation of the Ti-O bond length during cycling and the limitation of surface changes. The experimental and theoretical demonstration of the chemical causes of the titanium stabilization provides important knowledge about transition metal substitution of nickel-rich NMC materials. It additionally demonstrates that a stable and safe nickel-rich material is possible and can lead to further understanding of the chemical environment found in cathode lattices.

3.2. Introduction

Lithium-ion batteries provide the top choice for most practical electrochemical storage, including in consumer electronics and transportation.[1,2] Due to their ability to

provide better discharge capacities at lower voltages than typical cathodes, nickel-rich layered $LiNi_{1-x-y}Mn_xCo_yO_2$ ($1-x-y \geq 0.5$, NMC) provide an interesting option for potential cathode materials.[3,4] With increasing amounts of nickel in NMC materials, nickel's oxidation state goes beyond +2, and leads to interesting roles of the hybridization between the TM3d-O2p of NMC materials, which plays a crucial role as nickel oxidizes[5,6]. As nickel oxidizes, the Ni-O bond becomes more covalent, leading to oxygen oxidation and potential release.[7] Additionally, upon cycling, the activation of oxygen can lead to surface reconstruction that becomes compounded at higher voltages, longer cycles, and higher temperatures.[8] Either result of oxygen activation can degrade the cathode through various mechanisms.[9] Limiting oxygen activation can increase cycle life and stability as preventing surface reconstruction will limit impedance build up from the rock salt on the surface of the particles.

Elemental substitution represents one of the most prominent strategies for developing inorganic battery materials in fundamental and practical studies. However, there is lack of knowledge about manipulating the spatial distribution of substituting elements and understanding their reversible evolution at the orbital and atomic scales. Specifically, titanium, due to its stable +4 oxidation state, has been shown potential as a substituent. Titanium is suspected to replace Co^{3+} in NMC materials, but since it is a 4+ ion, there must be charge compensation, likely from manganese reduction.[10]

Research has shown that substituting an element increases cycle life and other mechanical properties of different cathodes. One theory believes that titanium increases slab spacing in the layered structure allowing for more efficient lithium diffusion upon cycling.[11] Additionally, titanium has been theorized to stabilize cycling of nickel-rich

materials. One reason for this has to do with the limitation of the free energy of formation of rock-salt on the surface.[12]

In this work, we segregate Ti^{4+} through a gradient addition to the top few nanometers of primary nickel-rich $LiNi_{0.8}Mn_{0.1}Co_{0.1}O_2$ particles. The surface substituting Ti^{4+} is fully incorporated into the TMO_6 octahedral coordination and exhibits highly reversible chemical environment upon repeated cycling. Our studies suggest that Ti^{4+} in the TMO_6 octahedral coordination increases the bond length and reduce the covalency between transition metals and oxygen. The resulting materials show superior oxygen reversibility at the cathode–electrolyte interphase, leading to significantly improved cycle life, including stable specific capacity and voltage. Our work offers atomic insights into the roles of substituting elements with spatial resolution and rationalizing the substitution strategy that the battery field have been implementing for a long time.

3.3. Results and Discussion

3.3.1. Pristine Material Characterization

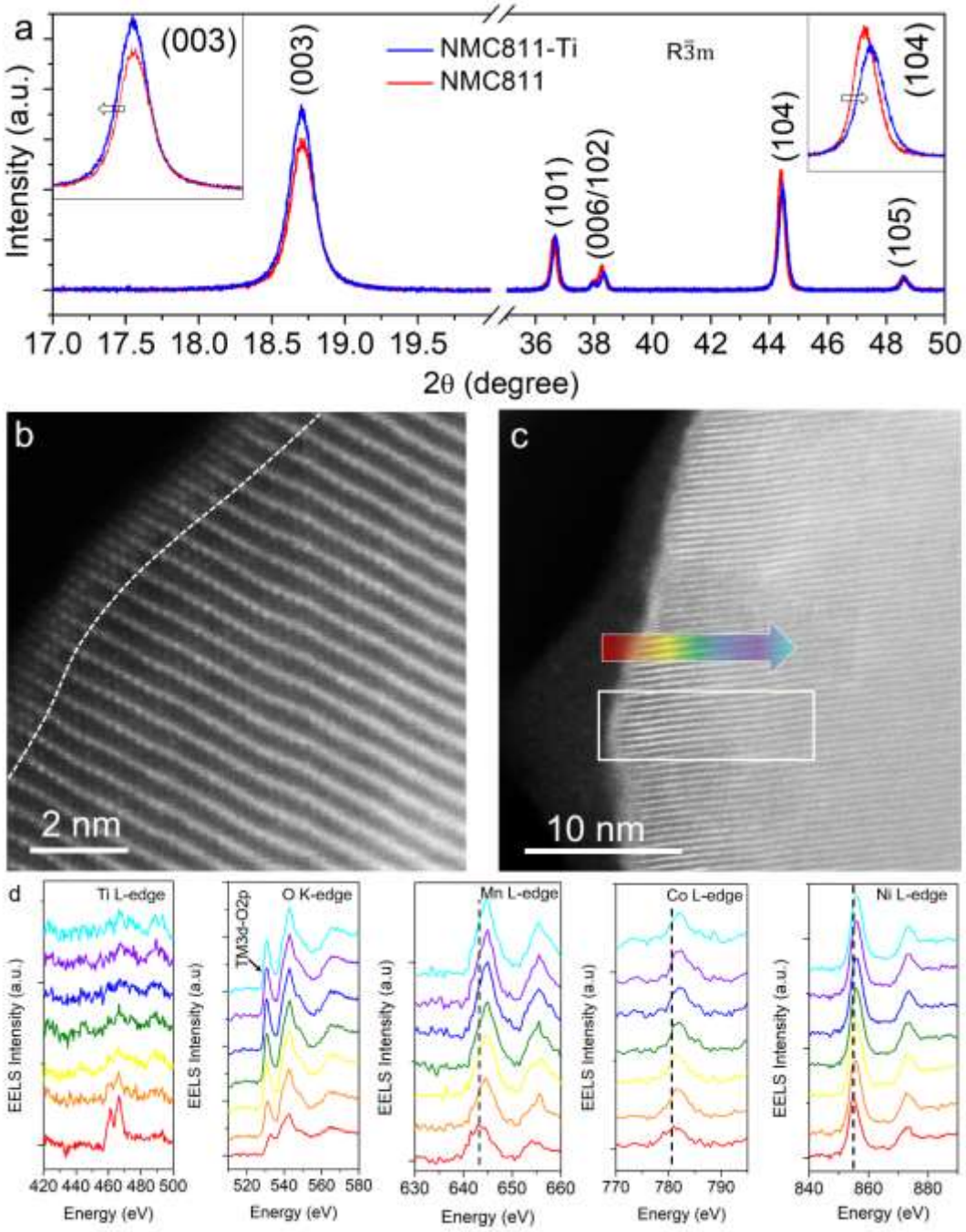

Figure 3-1. (a) XRD patterns of pristine NMC811 and titanium doped NMC 811. The insets show the 003 peaks and 104 peaks. (b) STEM image of pristine titanium doped NMC811 powder. (c) the area of the particle that was analyzed by EELS. (d) EELS

spectra of the transition metal L-edges and the oxygen K-edge, with the TM3d-2p hybridization labeled. The dashed line in (b) represents the transition line to typical surface changes seen in NMC811 materials. The EELS spectra probed deeper from bottom to top, as indicated by the arrow in (c).

We investigated the effect of 3% titanium substitution into the NMC811 crystal structure (NMC811-Ti) on the nickel and oxygen stability within the lattice. Our X-ray Diffraction (XRD) patterns (**Figure 3-1a)** indicated the initial effects of titanium substitution. The 003 shift showed an increase in the c parameter and the 104 shift showed a decrease in the a and b lattice parameters. Thus, the titanium resulted in a c direction expansion coupled with an a and b direction contraction, which increased the bond length and limited oxygen activation due to the change in the lattice dimensions. The separated XRD patterns were provided to observe the layered structure peaks separately (**Figure 3-2a-b**).

Generally, when the I_{003}/I_{104} ratio gets closer to 1, it is caused by an increase in cation mixing within the layered structure. Nickel-rich materials tend to have more cation mixing as the nickel ions can enter the lithium-ion sites, especially after surface reconstruction. In our study, our NMC811 had a ratio of 1.35 while NMC811-Ti had a ratio of 1.74. Thus, the addition of titanium provided stability to our pristine material by limiting initial cation mixing that would also limit surface reconstruction

We also performed STEM-EELS analysis on our pristine NMC811-Ti powder to understand the elemental chemistry (**Figure 3-1b-d**). Our STEM image (**Figure 3-1b**) confirmed a layered structure in the particle but with a slight surface reconstruction that was expected in nickel-rich cathodes (indicated with the white dashed line). Our EELS

data probed the pristine particle from surface to bulk (**Figure 3-1c**) for all our transition metals and oxygen. It demonstrated that most of our titanium was segregated to the surface (**Figure 3-1d**). This information was essential to confirming that titanium was successfully integrated into the lattice in increasing amounts from bulk to surface. The lack of TiO_2 peaks in soft XAS of the pristine powder further proved that the titanium was in the lattice rather than forming separate TiO_2 molecules (**Figure 3-2c)**.

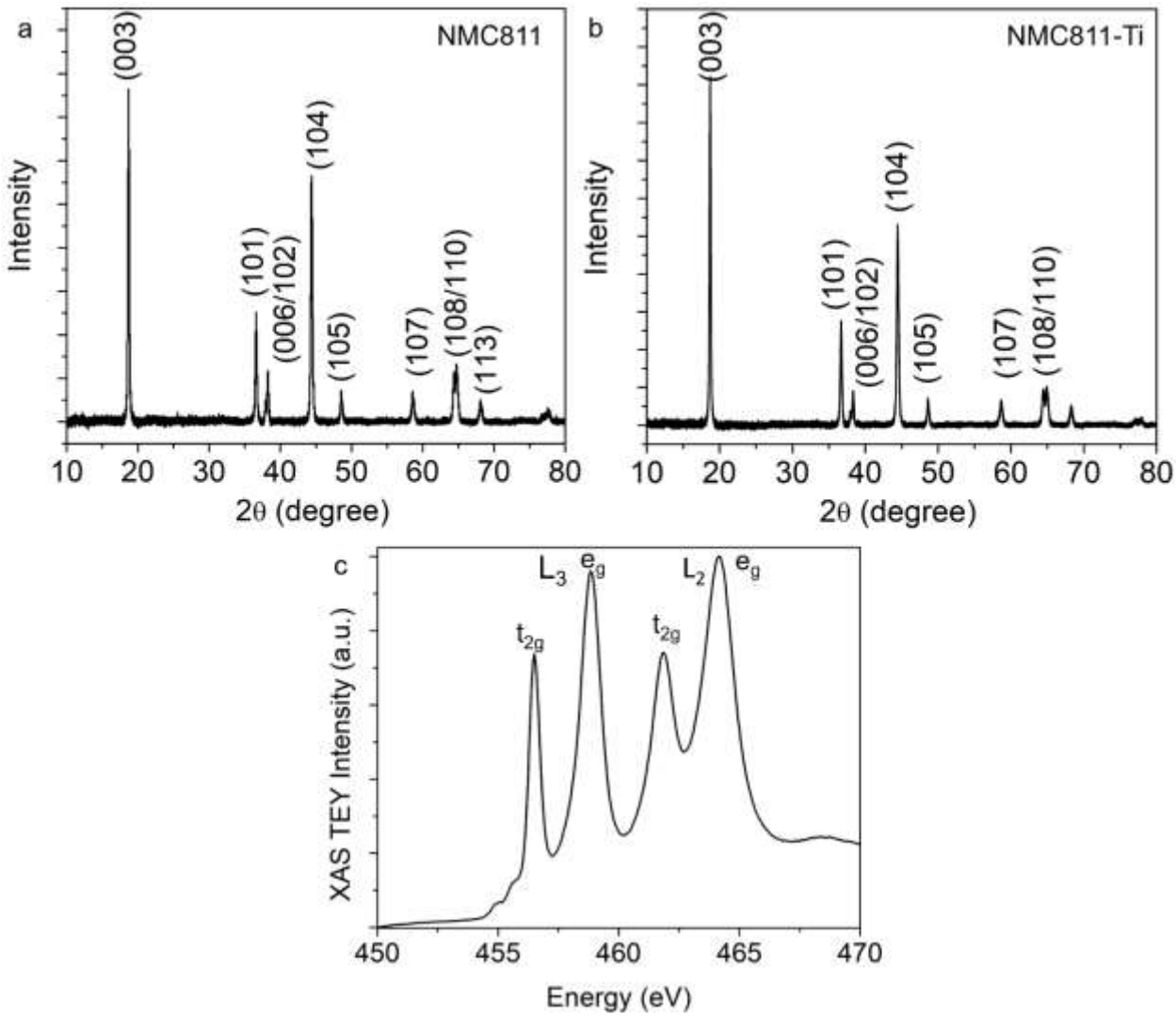

Figure 3-2. a. Powder XRD spectrum of NMC811. b. Powder XRD of NMC811-Ti and c. TEY of Ti L-edge of pristine NMC811-Ti.

Additionally, the Tm3d-O2p peak in our O K-edge increased as we probed deeper, which coincided with the oxidation shift of all our transition metals. These oxidation changes demonstrated that the layered material was maintained deeper in the particle, which confirmed our observation of minimal surface reconstruction.

3.3.2. Electrochemical Performance

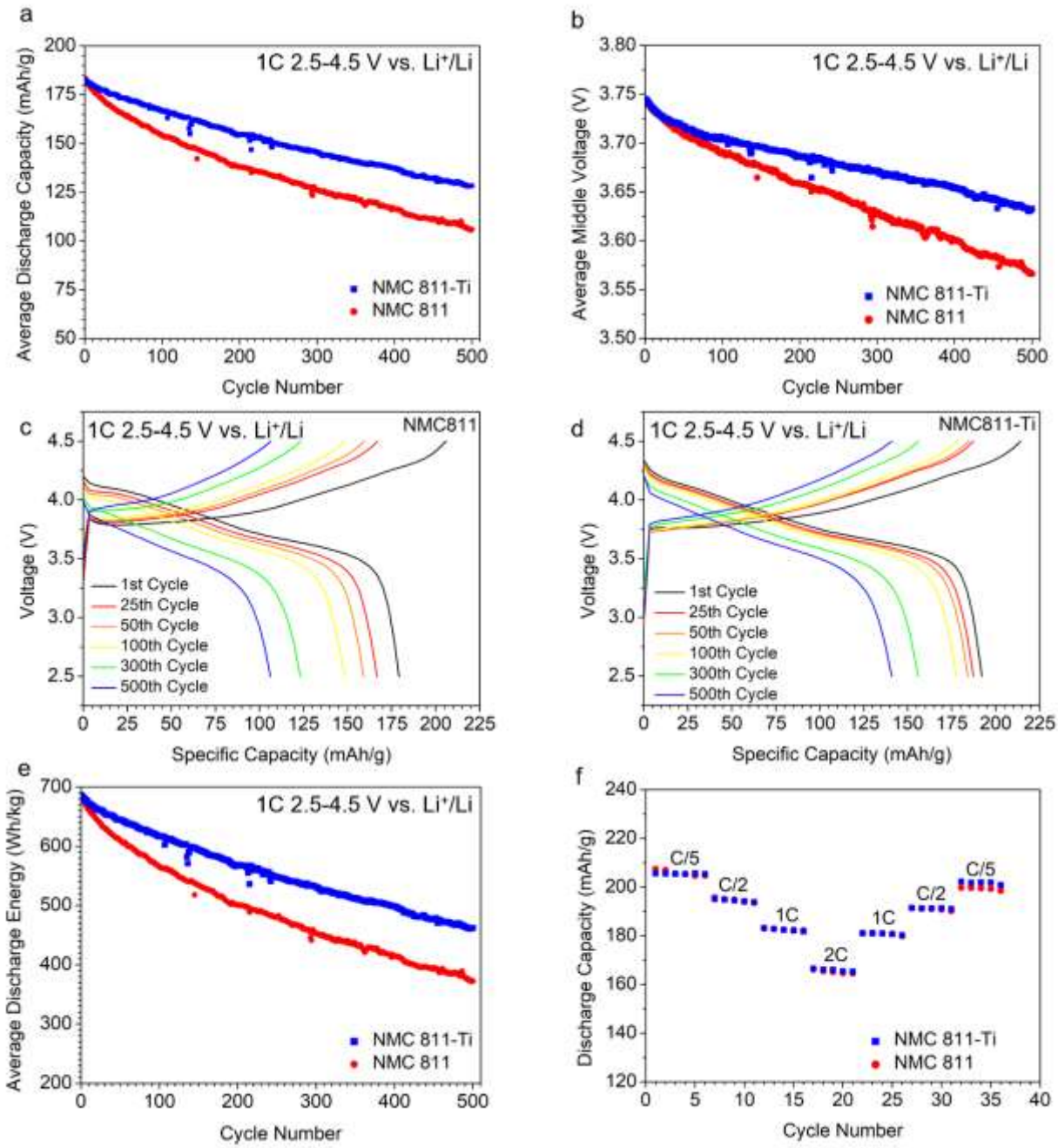

Figure 3-3. Electrochemical performance of cells containing pristine NMC811 and NMC811-Ti. (a) Discharge capacities for 500 cycles at 1C between 2.5-4.5 V vs. Li^+/Li. (b) The voltage for 50% of the discharge capacity (middle voltage) for 500 cycles. (c)

Charge-discharge curves for pristine NMC811. (d) Charge-discharge curves of NMC811-Ti. (e) specific energy for 500 cycles at 1C. (f) discharge capacities at various C rates.

We analyzed the electrochemical performances of our NMC811 and NMC811-Ti over 500 cycles at 1C between 2.5-4.5 V *versus* Li^+/Li to observe cycling stability of our compound (**Figure 3-3a-e**). Our synthesis methods were tested for 50 cycles and compared to pick our best material (**Figure 3-4**). Our results indicated a stabilization of our cathode material in all facets

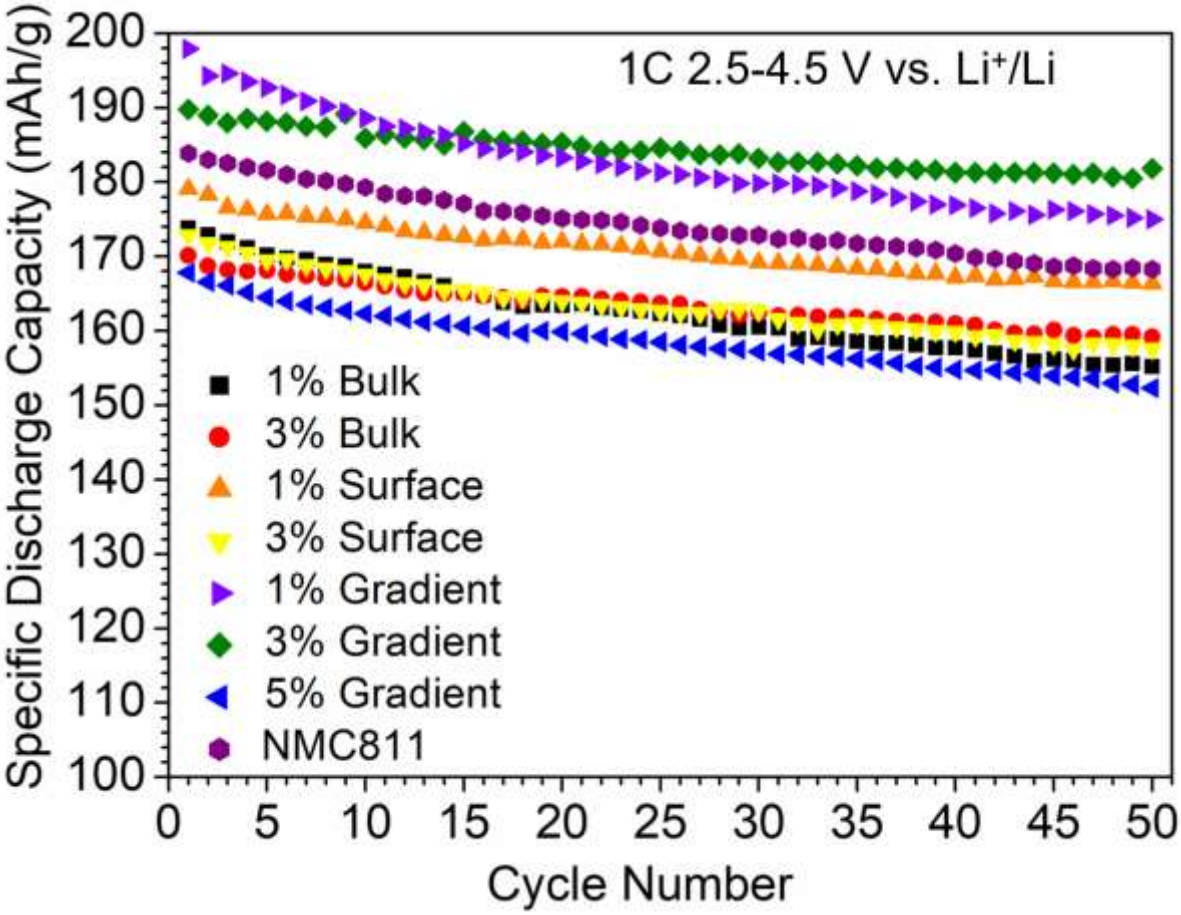

Figure 3-4. Electrochemical Cycling of varied Ti addition methods. Where bulk titanium was added directly to the transition metal solution initially and surface addition occurred after all transition metal solution was mixed with the base solution.

including energy density, discharge capacity, and voltage drop. The addition of titanium increased the capacity retention from 68.89% to 79.63% over 300 cycles, and from 57.81% to 70.27% over 500 cycles (**Figure 3-3a**). This could be attributed to the limited voltage drop seen in charge/discharge curves, indicating that less resistance has formed on the surface, due to less surface reconstruction after the addition of titanium (**Figure 3-3(b)-(d)**). The middle voltage of the material increased with the titanium and showed a drop of only 0.1125 V compared to 0.17415 V over 500 cycles (**Figure 3-3b**). Titanium also increased the energy density retention from 54.31% to 67.35% (**Figure 3-3e**). We performed a rate capability test using varied cycling rates to observe the effects on the cathode materials (**Figure 3-3e**). We observed that initially the C/5 rate for NMC811 was higher but maintained 95.71% of its capacity after harsh cycling, which resulted in a lower final capacity than the NMC811-Ti, which maintained 97.71% of its initial capacity. The electrochemical performance demonstrated the stabilization ability of titanium substitution.

3.3.3. Chemical and Structural Analysis During and After Cycling

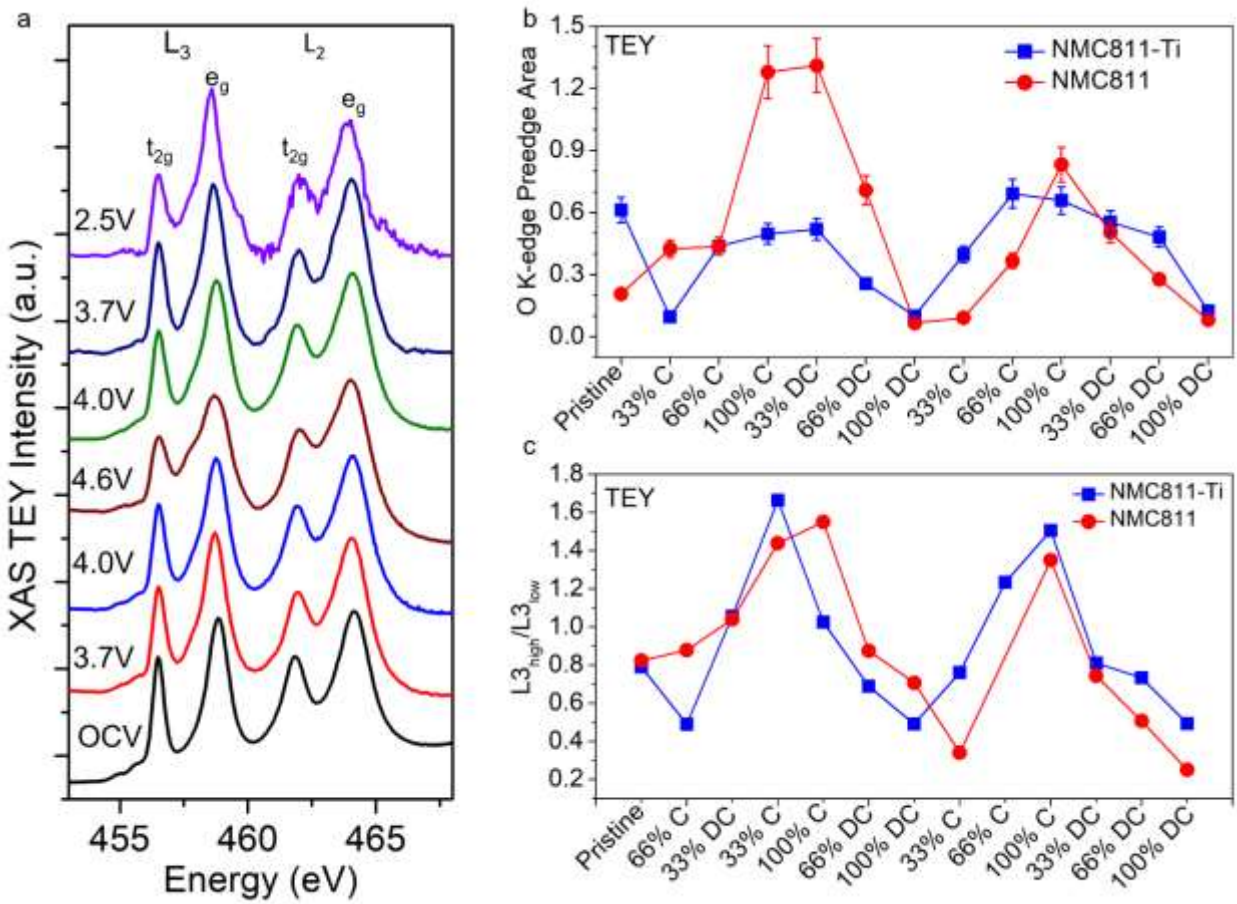

Figure 3-5. Soft XAS TEY quantification of (a) the first cycle of the titanium L-edge, (b) the oxygen K-edge with the integrated area of the pre-edge TM3d–O2p peak, and (c) nickel showing the ratio of the L_3 peaks.

To understand the structural reasons for this electrochemical stability, we used soft XAS to observe specific elemental changes during the first two cycles cycling. Our Ti L-edge TEY demonstrated a peculiar reversible phenomenon where a shoulder formed during charging that was indicative of a rutile titanium dioxide that reverses upon discharging (**Figure 3-5a**). This occurs in the second cycle as well (**Figure A-9a**). We

attributed this oscillation to a formation of pseudo-titanium dioxide upon delithiation that helps stabilize oxygen upon the oxidation of the transition metals, specifically nickel. For our O K-edge, we took the area of the preedge peak (**Figure A-10(a)-(e)**) to visualize the change in the hybridization during cycling. Notably, compared to the NMC811, the gradient addition of titanium deactivated and stabilized our oxygen and limited the overall hybridization intensification, which allowed for more reversible oxygen changes (**Figure 3-5b**). Conversely, for the Ni L-edge we compared the oxidation states by utilizing their L_3 height ratios. All our nickel soft XAS and samples of the peak heights are demonstrated in the Supporting Information (**Figure A-10(f)-(j)**). During cycling, the NMC811-Ti was able to achieve nickel oxidation states that was more reversible than pristine NMC811, which allowed for a more stable cycle life (**Figure 3-5c**). We theorized that titanium stabilized the oxygen atoms and limited release, while still allowing nickel to oxidize to provide high discharge capacities. When combined with the titanium soft XAS, we hypothesized oscillation between pseudo-TiO_2 phase stabilized oxygen that would normally activate with high nickel oxidation states, which allowed for the more stable cycling.

We performed the same analysis on the FY mode of soft XAS (**Figure A-9(b)-(c)**). The titanium addition stabilized oxygen to prevent the increase of the preedge area and limited deep oxygen loss. Comparably, the nickel oxidation states still achieved similar high points as pristine NMC811. Thus, the addition of titanium in our gradient method allowed nickel to achieve similar oxidation states and provide similar capacities. It also provided more stable oxygen, which helped inhibit the surface changes seen in

pristine NMC811. This stabilization, limited oxygen loss and nickel reduction led to strong capacity retention.

For cobalt and manganese, we focused on the TEY mode of the soft XAS. We noted for both materials, as in our pristine NMC811, there was no major change in the surface oxidation states of cobalt and manganese. This behaves as expected for our nickel-rich material as our surface changes seen in Pristine NMC811 were based on nickel, and now with titanium we are beginning to limit the nickel changes on the surface rather than manganese and cobalt. (**Figure A-11**).

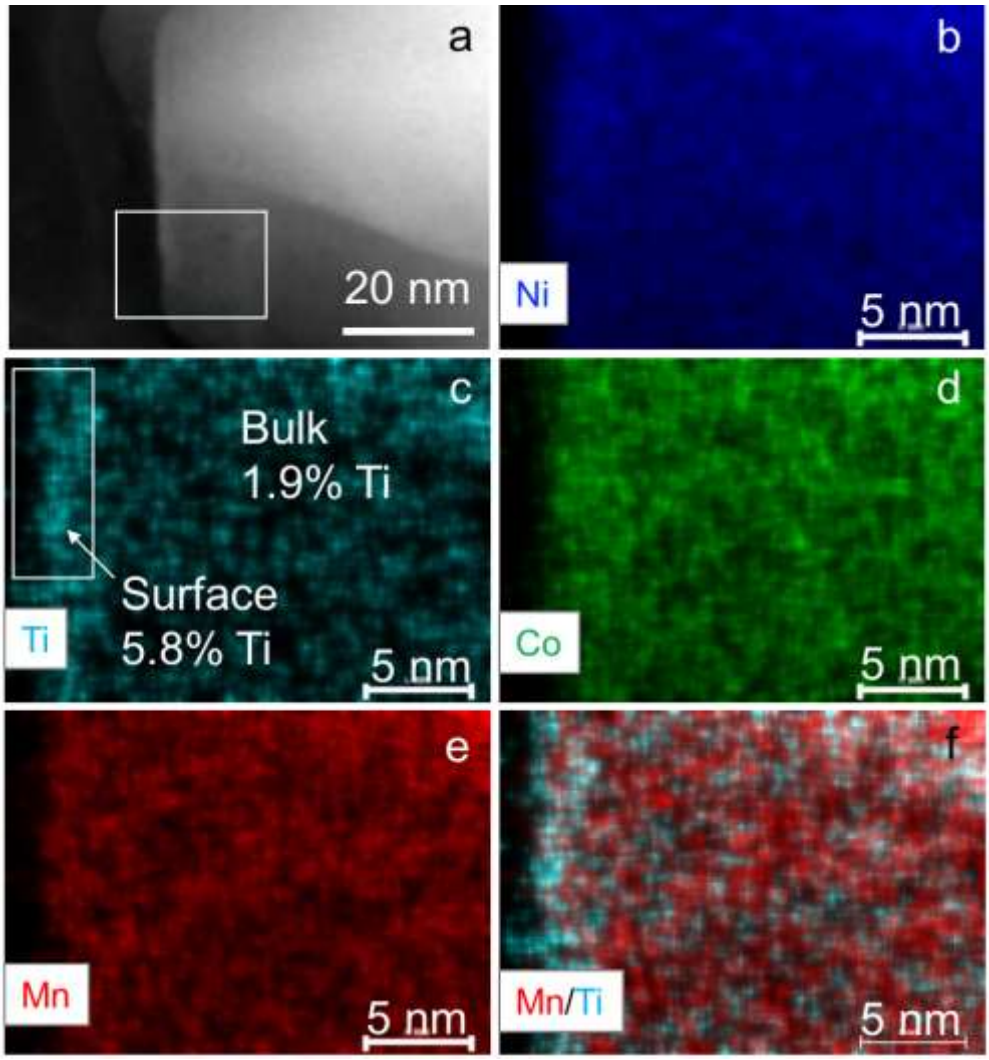

Figure 3-6. STEM-EDS mapping of the NMC811-Ti material after 300 cycles at 1C. (a) STEM image showing the studied region, (b) Ni, (c) Ti, (d) Co, (e) Mn, and (f) Mn/Ti

We then analyzed 300 cycle NMC-Ti to better understand the long-term stability of gradient titanium substitution. Our STEM-EDS data of a NMC811-Ti electrode after 300 cycles indicated that titanium remained segregated in a similar matter as the pristine material. (**Figure 3-6**). This demonstrated our gradient addition increased the titanium concentration from bulk to surface, and the titanium remained in place even after long-

term cycling. Additionally, our other transition metals maintained their expected distributions throughout the particle.

We compared X-ray absorption near edge structure (XANES) of NMC811 to NMC811-Ti, we observed that after 300 cycles, Nickel has oxidized in NMC811, while there has been almost no observable change with the addition of titanium, which confirmed our short-term stabilization seen in Soft XAS (**Figure 3-7(a)-(b)**).

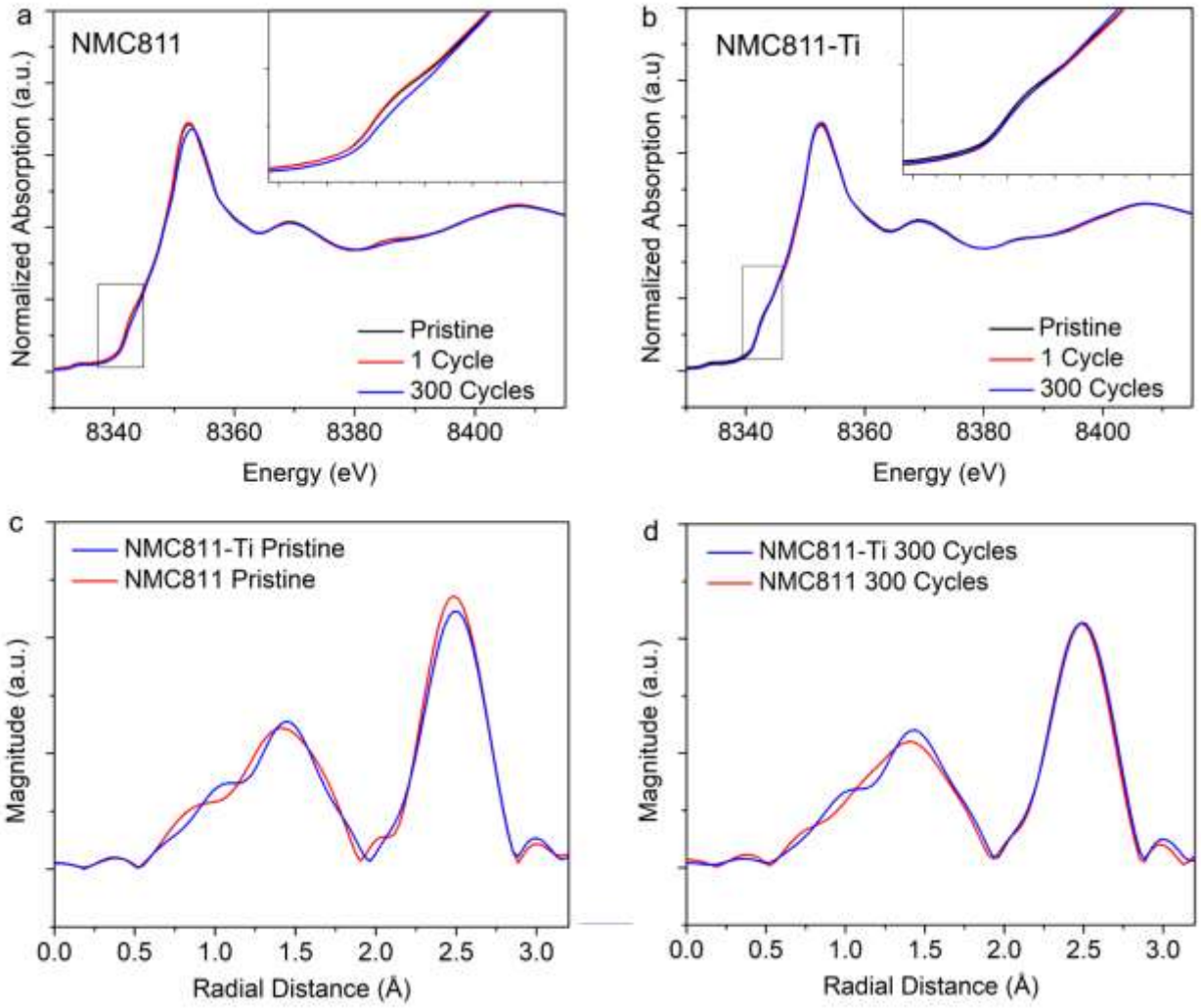

Figure 3-7. a. XANES of nickel for NMC811, b. XANES of nickel of NMC811-Ti, c. EXAFS comparing the pristine nickel of NMC811 and NMC811-Ti, d. EXAFS comparing nickel of NMC811 and NMC811-Ti after 300 cycles.

Additionally, the Extended X-ray fine structure (EXAFS) directly compared the NMC811 and NMC811-Ti pristine and 300 cycle electrodes (**Figure 3-7(c)-(d)**). The TM-O peak shifted to a longer bond length after the addition of titanium that remained there even after long term cycling. Higher oxidation states of nickel typically lead to oxygen loss due to an increase in the covalent relationship of the bond. By adding titanium, we limited the nickel-oxygen covalency, which resulted in less oxygen loss and coincided with our results of oxygen stabilization in the soft XAS of the O K-edge. Thus, the titanium addition provided a means to stabilize the nickel-oxygen relationship in nickel-rich cathodes and provided a more stable cycle life for the battery. We further provided the direct comparisons of these cycles in the Appendix to show all possible methods to observe this phenomenon. (**Figure A-12**).

We also analyzed the cobalt and manganese oxidation states using hard XAS. Our analysis of the XANES of cobalt (**Figure A-13**) demonstrated that the titanium addition did not have a major effect on the cobalt oxidation state changes over 300 cycles. Both samples had a slight reduction of cobalt, which indicated that the stability increase does not come from a change in cobalt, but also demonstrated that titanium does not alter the local environment of cobalt in NMC811 structures. We analyzed the EXAFS (**Figure A-14**) for any bond changes as observed in nickel. For cobalt, there was no discernable shifts in bond lengths of either TM-O or TM-TM for cobalt, which further indicated that titanium addition altered nickel's environment, while leaving the cobalt local environment in a similar condition to pristine NMC811.

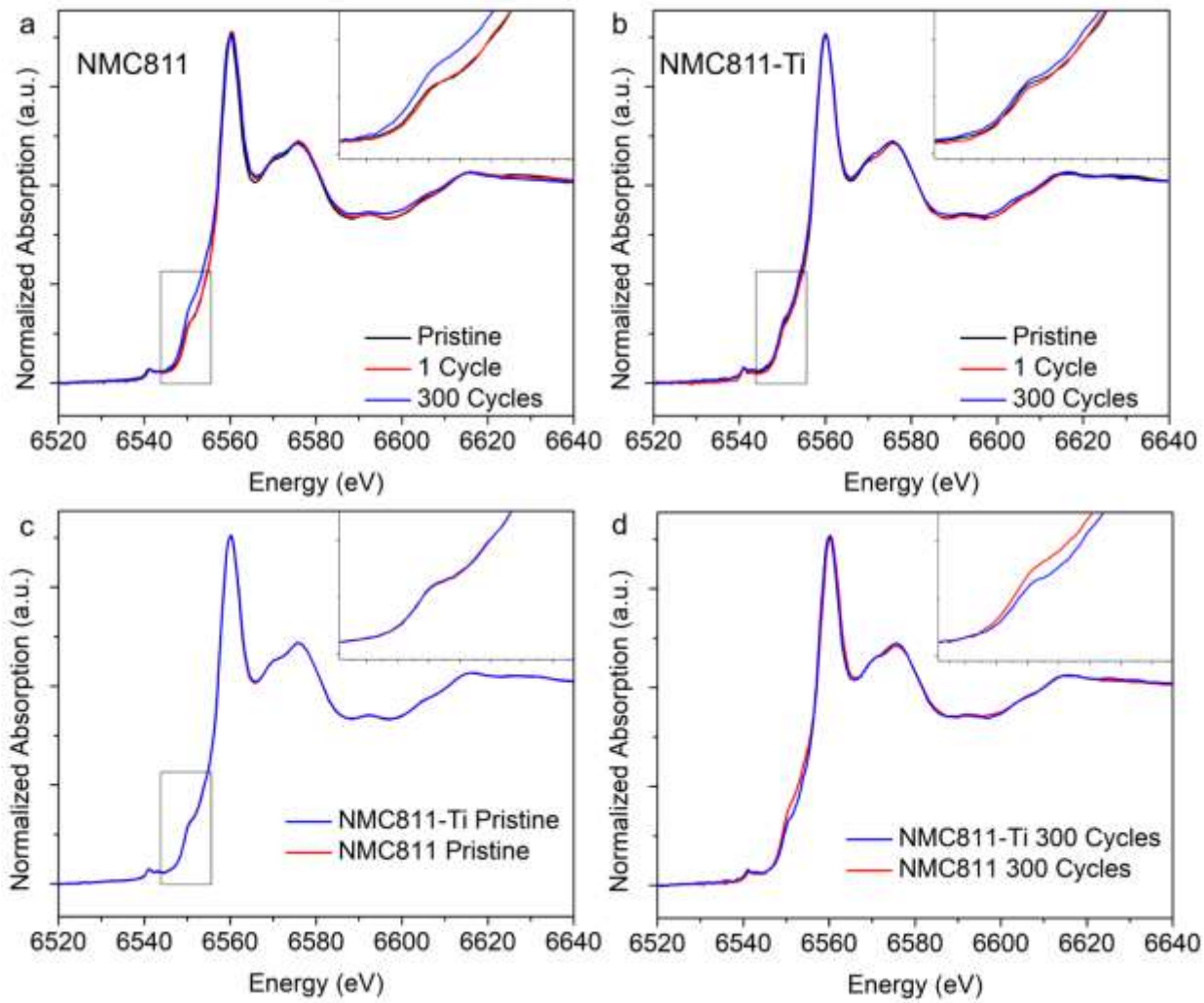

Figure 3-8. XANES of manganese for a. NMC811, b. NMC811-Ti, c. comparing the pristine state, and d. comparing after 300 cycles

For manganese, we analyzed our XANES changes (**Figure 3-8**). Notably, the addition of titanium stabilized manganese in the same manner as nickel. In this case, pristine NMC811 had a reduction of manganese over long term cycling, likely compensating for the high nickel oxidation states. With the addition of titanium, we limit this manganese reduction. Based on this data, our titanium provided the compensation stability during cycling that manganese typically provided in NMC cathodes. After 300

cycles, we can additionally see that titanium stays on the surface and limits manganese surface exposure (**Figure 3-6f**).

To further confirm our analysis of the bond changes, we performed Finite Difference Method Near Edge Structure (FDMNES) and Density-Function State (DFT) calculations for our materials to calculate potential changes in the system. The calculations relied on the fact that as lithium is removed, first the surface ions delithiate, then further into the bulk. The calculations also considered the soft XAS of our titanium as it indicated the changing Ti-O bonds within the lattice. The DFT calculations initially confirm that delithiation causes strain upon the delithiation path that can be a cause of typical phase transformation. They indicated that the addition of titanium increased the lattice size, which limited phase transformation and strain upon delithiation, and provided better reversibility. This result from DFT confirms the XRD and cycling conclusions. XRD confirmed the calculations of expanded lattice in the c direction and the cycling data showed greater reversibility with less surface resistance than pristine NMC811. Thus, our experimental behavior confirmed our theoretical data that titanium will stabilize the surface in a way to limit degradation of the cathode.

Our FDMNES calculations provide support for the bond length argument discussed during experimentation. Our soft XAS indicated a reversible peak broadening that we indicated made a pseudo-TiO_2 compound. This broadening was analyzed to look at area and the Full Width Half Maximum (FWHM) of the peaks (**Figure 3-9**). The peaks' FWHM and area were then compared to calculated bond length to show trends upon the delithiation in conjunction with the broadening seen in our experimental soft XAS (**Figure 3-10**).

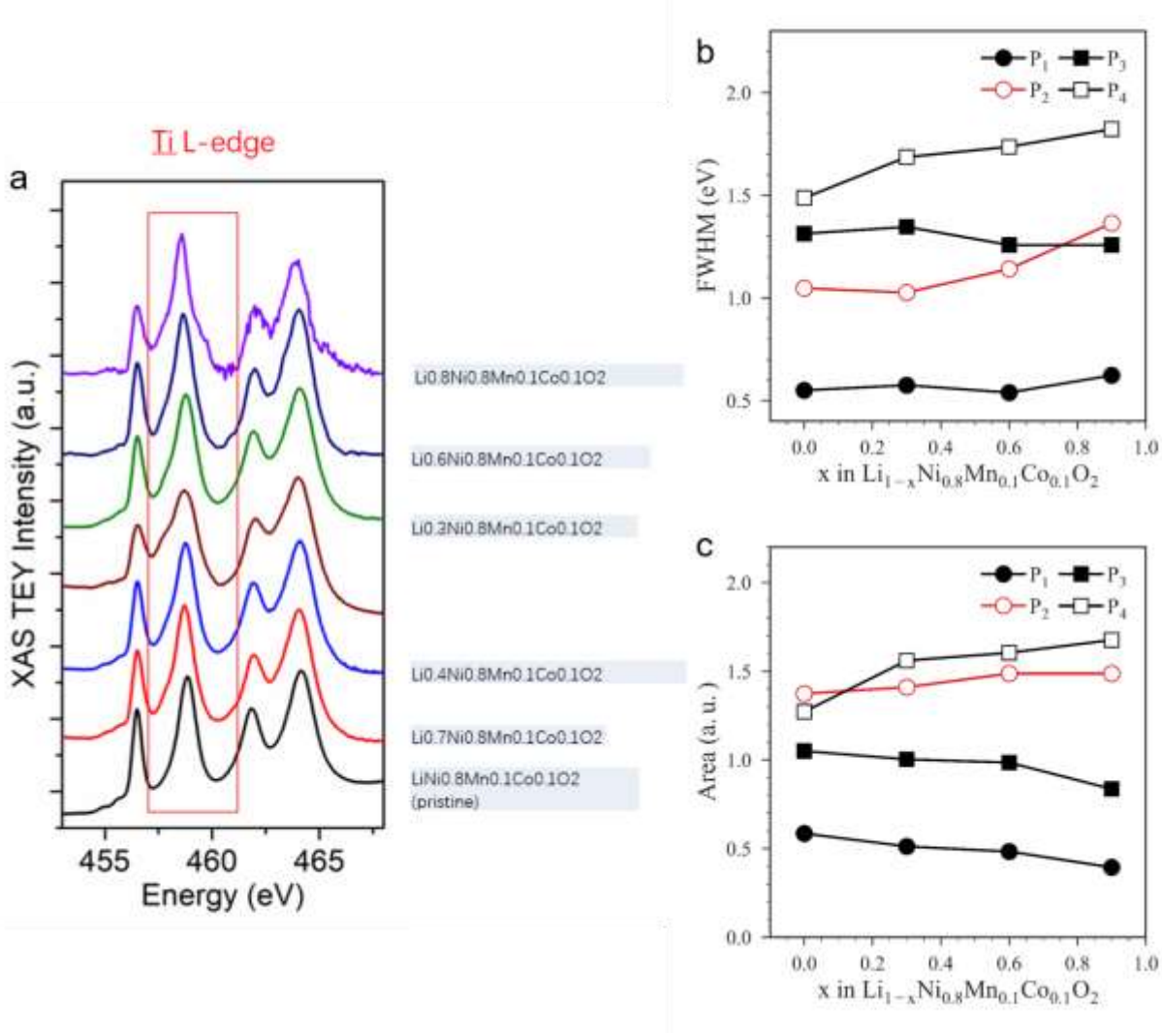

Figure 3-9. a. Soft XAS for first cycle indicating the peak analyzed for broadening. b. Full Width Half Maximum versus degree of delithiation for each peak. c. Area of peak versus degree of delithiation.

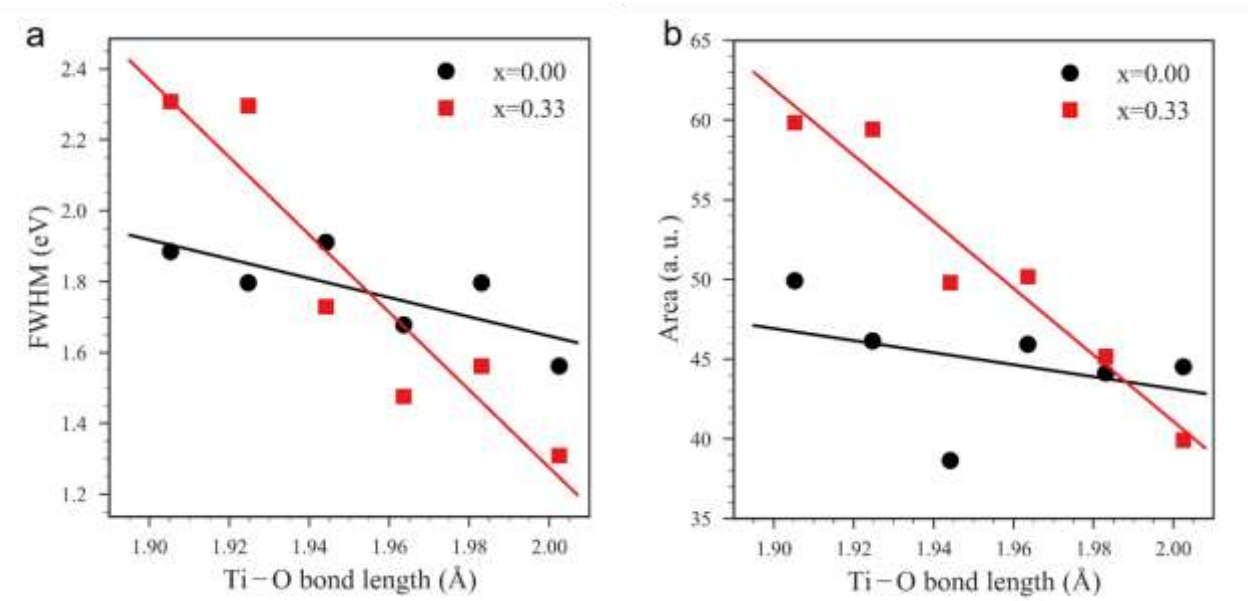

Figure 3-10. Comparison of the peak 2 using a. FWHM versus bond length and b. Area versus bond length

The calculations indicated a change in bond length of Ti-O during charging and discharging. Specifically, the bond length will shorten upon charge and lengthen about discharge. The shorter bond length implies a stronger Ti-O bond that confirms our conclusions in our XANES and EXAFS. That is, that the titanium stabilized the oxygen in the lattice through this Ti-O_2 formation upon nickel oxidation. This would lead to stronger Ti-O bonds upon delithiation, which is confirmed by our FDMNES. This information was crucial as it indicated the method of how titanium stabilized oxygen as well as limited phase changes. Thus, the addition of titanium provided the lattice with stabilization with the increased slab distance and the creation of pseudo-TiO_2 during cycling.

3.4. Conclusion

Nickel-rich NMCs, especially NMC811, are prone to low cycle retention due to surface reconstruction and other degradation from strain in the lattice. Our gradient titanium addition provided a unique synthesis approach that drastically increased the stability of NMC811. We used specific surface and bulk analysis to help analyze the chemical and bonding environment of our material. Our experimental results demonstrated a deactivation of oxygen that helped prevent typical oxygen loss seen in nickel-rich materials. Additionally, we indicated that a formation of pseudo-TiO_2 that helped limit the known covalency between Ni^{4+} and oxygen during cycling. These observations provided evidence of how stable titanium can limit cathode degradation overtime. Additionally, our findings were supported through theoretical calculations that show how titanium helps limit surface changes and creates stronger bonds to oxygen during cycling. Thus, this study provides a guideline for future research of metal substitutions to nickel-rich NMCs that could create breakthroughs to even more stable and safer cathode materials.

3.5. Experimental Methods

3.5.1. Synthesis Method

Our materials were synthesized using a slightly modified coprecipitation method. A transition metal solution of 0.8M $NiSO_4 \cdot 6H_2O$ (Sigma Aldrich, 99.99%), 0.1M $MnSO_4 \cdot H_2O$ (Sigma Aldrich, 99%) and 0.1M $CoSO_4 \cdot 7H_2O$ (Sigma Aldrich, 99%) were dissolved in 100 mL of DI water with a concentration of 1M. A base solution of 2M NaOH and 1.67M $NH_3 \cdot H_2O$ was diluted to 100 mL in DI water. Each solution was stored in its own Kimble bottle and the base solution was under N_2 gas. A third titanium solution was made using a titanium oxysulfate solution (Sigma Aldrich, 15 wt% in dilute sulfuric acid).

0.03 moles of titanium in the solution were used then diluted to 50 mL. This titanium solution was stored in its own Kimble bottle. 1M NaOH and 0.83M $NH_3 \cdot H_2O$ was diluted to 160 mL in DI water and then placed into the reaction flask. The flask was heated to 50 °C, protected with N_2 gas, stirred continuously starting at 600 RPM, and adjusted so that the pH value was approximately10.5. The transition metal solution and base solution were pumped into the reaction flask at approximately 2 mL/min. Once the pumping began, a third pump was used to start pumping the titanium solution directly into the transition metal solution at 2 mL/min. The temperature and nitrogen protection were maintained throughout the reaction, and the base pumping was tuned to maintain a pH of 10.5±0.1. The stirring rate was gradually increased to maintain a consistent vortex in solution as volume increased. The precipitate was collected using vacuum filtration and was, washed with 400 mL DI water and then 400 mL of isopropanol. The precipitate was dried in a vacuum oven overnight at 100 °C. The precursor and LiOH were mixed thoroughly and calcined under pure oxygen flow at 0.5 L/min. The calcination procedure involved heating at 5 °C/min to 460 °C and holding for 1 hour. Then heating at 5 °C/min to 725 °C and holding for 6 hours. Finally, it was cooled5 °C/min to 25 °C under constant oxygen flow to obtain the final powder.

3.5.2. Electrode Preparation:

90% active material, 5% polyvinylidene fluoride, and 5% acetylene carbon black in N-methyl-2-pyrrolidone were cast onto carbon coated aluminum foil current collectors. The electrodes were dried under vacuum at 120 °C and had a loading capacity of approximately 4.3 ± 0.1 mg/cm^2. The cathode and lithium metal anode were separated CR2032-type coin cell with a glass fiber separator, which was soaked with an electrolyte

of 1 M $LiPF_6$ dissolved in a 3:7 ratio of EC/EMC with 2wt% VC. A LAND battery testing system was used to perform electrochemical testing, where 1C was considered the rate of charging for one hour with a specific capacity of 200 mAh/g. The same rate was used for discharging the cathode.

3.5.3. Materials characterization:

A PANalytical Empyrean X-ray diffractometer with a Cu K_α (λ=1.54 Å) x-ray source and Bragg-Brentano HD divergent beam optic with an energy resolution of about 450 eV was used to collect powder XRD. The incident beam path included a 0.02 rad Soller slit, 10 mm beam mask, fixed antiscatter slit (1/2°) and fixed divergence slit (1/8°). Dry samples were loaded individually onto 32 mm low-background Si wafer samples holders with 0.2 mm wells (Panalytical) and rotated in place during the analysis. Diffracted intensities were collected from 10 to 80° 2θ in approximately 0.0018° increments using a GaliPIX^{3D} area detector system operating in line mode (501 active channels). The exposure time was approximately 28 sec/point. A 0.02 rad Soller slit was used in the diffracted beam path. The 31-pole wiggler beamline 10-1 at Stanford Synchrotron Radiation Lightsource (SSRL) using a ring current of 350 mA and a 1000 $l \cdot mm^{-1}$ spherical grating monochromator with 20 μm entrance and exit slits, providing ~10^{11} ph·s-1 at 0.2 eV resolution in a 1 mm^2 beam spot was used to collect soft XAS data. Total electron yield (TEY) was acquired using a single load at room temperature in an ultrahigh vacuum (10^{-9} Torr), and fluorescence yield (FY), where a silicon diode (IRD AXUV-100) was used to collect the FY positioned near the sample surface. Our scanning transmission microscopy (STEM), electron energy loss spectroscopy (EELS), and Energy Dispersive Spectroscopy (EDS) were acquired on a JEOL 2100 S/TEM operated at 200 keV. Beamline 20-BM-B of

the Advanced Photon Source (APS) at Argonne National Laboratory was used to collect hard XAS measurements (XANES and EXAFS of Ni, Mn, and Co K-edge). A Si(111) fixed-exit, double-crystal monochromator was the incident beam that was used. Ni, Mn, Co XANES spectra were collected simultaneously from metal foils that were used with their first derivative maximum to perform energy calibration for each spectrum used in this paper.

3.5.4. FDMNES Calculation Details

The time-dependent density functional theory (TDDFT) was performed based x-ray absorption calculation for our A1-xMO2(A=Li, Na) Ti-rich cluster model, as implemented in Finite Difference Method Near Edge Structure (FDMNES) package [4]. Within the TDDFT method, we could describe the partly localized edges (L23 edges of transition metal Ti) quite correctly beyond the most common density functional theory (DFT). All calculations were performed on clusters containing 66 atoms and the convolution widths used are 1.2eV for L2 and L3 edge.

3.5.5. DFT Calculation Details

First-principles plane-wave calculations were performed based on density-functional theory (DFT), as implemented in Quantum Espresso simulation package, for total-energy and electronic-structure of NaxMn1-yTiyO2.The calculations made use of the spin-dependent generalized gradient approximation of Perdew, Burke, and Ernzerhof (PBE) [2]. The wave functions were expanded in a plane wave basis set using ultra-soft pseudopotentials with an energy cutoff above 680 eV. The Γ-centered k-point mesh of 8x8x4 for the Brillouin zone sampling are used for unit cell in our calculation respectively.

3.6. References

References

(1) Noorden, R. Van. The Rechargeable Revolution: A Better Battery. *Nature* **2014**, *507*, 26–28.

(2) Dunn, B.; Kamath, H.; Tarascon, J.-M. Electrical Energy Storage for the Grid: A Battery of Choices. *Science* **2011**, *334* (6058), 928–935.

(3) Myung, S.-T.; Maglia, F.; Park, K.-J.; Yoon, C. S.; Lamp, P.; Kim, S.-J.; Sun, Y.-K. Nickel-Rich Layered Cathode Materials for Automotive Lithium-Ion Batteries: Achievements and Perspectives. *ACS Energy Lett.* **2017**, *2* (1), 196–223.

(4) Zheng, J.; Kan, W. H.; Manthiram, A. Role of Mn Content on the Electrochemical Properties of Nickel-Rich Layered $LiNi_{0.8-x}Co_{0.1}Mn_{0.1+x}O_2$ ($0.0 < x < 0.08$) Cathodes for Lithium-Ion Batteries. *ACS Appl. Mater. Interfaces* **2015**, *7* (12), 6926–6934.

(5) Lin, F.; Nordlund, D.; Markus, I. M.; Weng, T.-C.; Xin, H. L.; Doeff, M. M. Profiling the Nanoscale Gradient in Stoichiometric Layered Cathode Particles for Lithium-Ion Batteries. *Energy Environ. Sci.* **2014**, *7*, 3077–3085.

(6) Yoon, W. S.; Balasubramanian, M.; Chung, K. Y.; Yang, X. Q.; McBreen, J.; Grey, C. P.; Fischer, D. A. Investigation of the Charge Compensation Mechanism on the Electrochemically Li-Ion Deintercalated $Li_{1-x}Co_{1/3}Ni_{1/3}Mn_{1/3}O_2$ Electrode System by Combination of Soft and Hard X-Ray Absorption Spectroscopy. *J. Am. Chem. Soc.* **2005**, *127* (49), 17479–17487.

(7) Dixit, M.; Markovsky, B.; Schipper, F.; Aurbach, D.; Major, D. T. Origin of Structural Degradation during Cycling and Low Thermal Stability of Ni-Rich Layered Transition Metal-Based Electrode Materials. *J. Phys. Chem. C* **2017**, *121* (41), 22628–22636.

(8) Steiner, J.; Mu, L.; Walsh, J.; Rahman, M. M.; Zydlewski, B.; Michel, M.; Xin, H. L.; Nordlund, D.; Lin, F. Accelerated Evolution of Surface Chemistry Determined by Temperature and Cycling History in Nickel-Rich Layered Cathode Materials. *ACS Appl. Mater. Interfaces* **2018**, acsami.8b06399.

(9) Mu, L.; Lin, R.; Xu, R.; Han, L.; Xia, S.; Sokaras, D.; Steiner, J. D.; Weng, T.-C.; Nordlund, D.; Doeff, M. M.; et al. Oxygen Release Induced Chemomechanical Breakdown of Layered Cathode Materials. *Nano Lett.* **2018**, *18* (5), 3241–3249.

(10) Kam, K. C.; Mehta, A.; Heron, J. T.; Doeff, M. M. Electrochemical and Physical Properties of Ti-Substituted Layered Nickel Manganese Cobalt Oxide (NMC) Cathode Materials. *J. Electrochem. Soc.* **2012**, *159* (8), A1383–A1392.

(11) Wilcox, J.; Patoux, S.; Doeff, M. Structure and Electrochemistry of LiNi[Sub 1⁄3]Co[Sub 1⁄3−y]M[Sub y]Mn[Sub 1⁄3]O[Sub 2] (M=Ti, Al, Fe) Positive Electrode Materials. *J. Electrochem. Soc.* **2009**, *156* (3), A192.

(12) Markus, I. M.; Lin, F.; Kam, K. C.; Asta, M.; Doeff, M. M. Computational and Experimental Investigation of Ti Substitution in Li1(NixMnxCo1-2x-YTiy)O2 for Lithium Ion Batteries. *J. Phys. Chem. Lett.* **2014**, *5* (21), 3649–3655.

(13) Lin, F.; Markus, I. M.; Nordlund, D.; Weng, T.-C.; Asta, M. D.; Xin, H. L.; Doeff,

M. M. Surface Reconstruction and Chemical Evolution of Stoichiometric Layered Cathode Materials for Lithium-Ion Batteries. *Nat. Commun.* **2014**, *5*, 3529.

Chapter 4. **Summary**

The preceding reports from this thesis detail the idea of degradation and stabilization of nickel-rich NMC materials. Importantly this work has demonstrated the degradation pathways of NMC811 upon cycling and at varying temperatures. This provides important insights into how NMC811 begins to degrade over time and allows researchers to begin focusing on the key issues seen in nickel-rich cathodes.

Beyond the degradation methods, our novel substitution method demonstrated a strong method to stabilize our NMC811. With the addition of titanium, we were able to provide a longer lasting battery and additionally study different chemical lattice aspects that provide important information on how substitution affects the cathodes lattice. This information can lead to future breakthroughs in cathode chemistry.

This work established that the stabilization of nickel-rich cathodes can be possible, and that one of the key ways to achieve this will be to limit the Ni-O covalent bonding to help deactivate oxygen. Future work can expand on this concept through substitution with other metals or possibly incorporating titanium into the lattice in varying ways to stabilize the lattice further. Beyond that, further surface protection is an option to help prevent even more degradation of the cathode. This current work provides the groundwork to delve deeper into the stabilization of nickel-rich cathode materials.

Chapter 5. Appendix

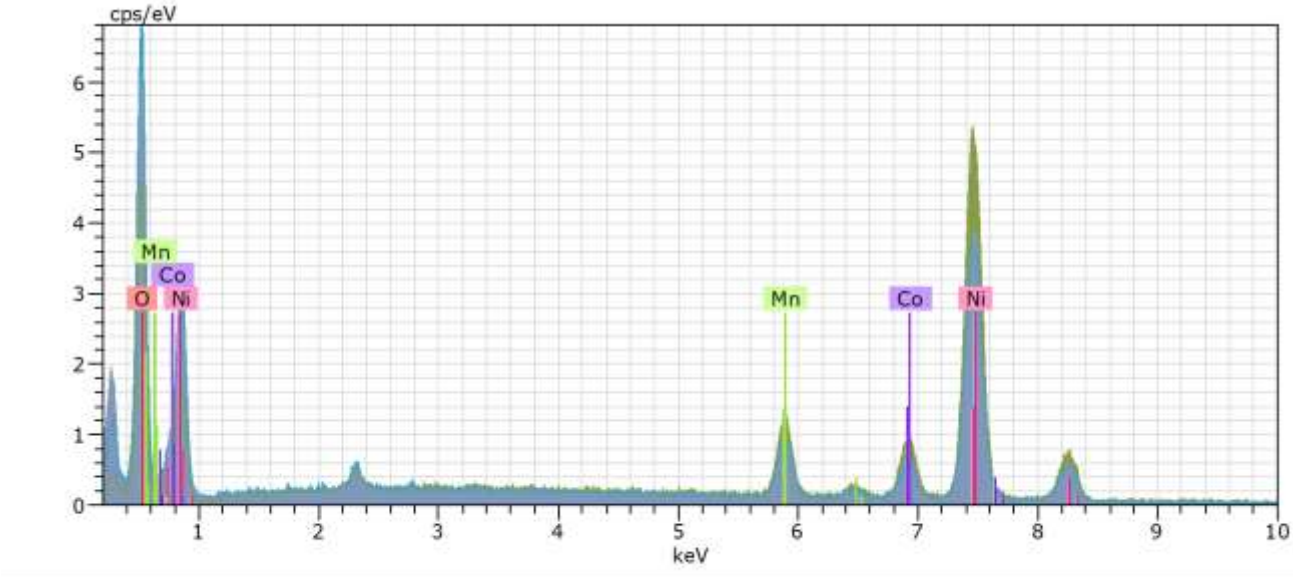

Molar Percent

Metal	Mole Percent
Ni	0.8
Mn	0.09
Co	0.1

Figure A-1. EDS of pristine NMC811, which shows an average of three sections of particles in the powder, which allows for a molar ratio of our material. The EDS was taken in conjunction with SEM of pristine NMC811. The results demonstrated that there was a ratio of $Ni_{0.8}Mn_{0.09}Co_{0.1}$, which indicated that the composition of the particles was essentially the expected NMC811.

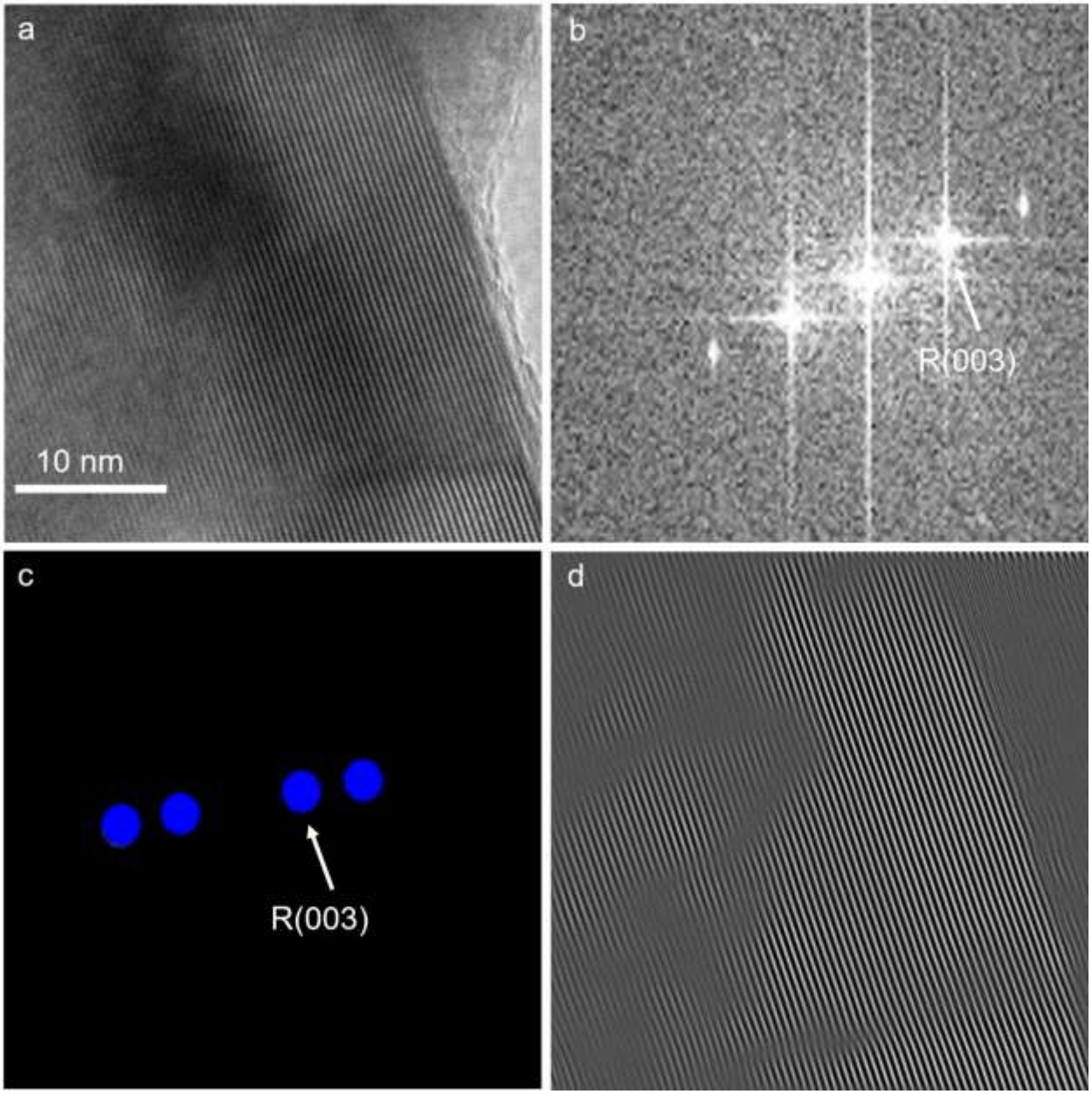

Figure A-2. (a) TEM image of pristine NMC811 powder. (b) The fast Fourier Transform (FFT) of the TEM image. (c) Masked image of the FFT showing the layered R$\bar{3}$m phase. (d) Inverse FFT of the TEM image showing the layered phase.

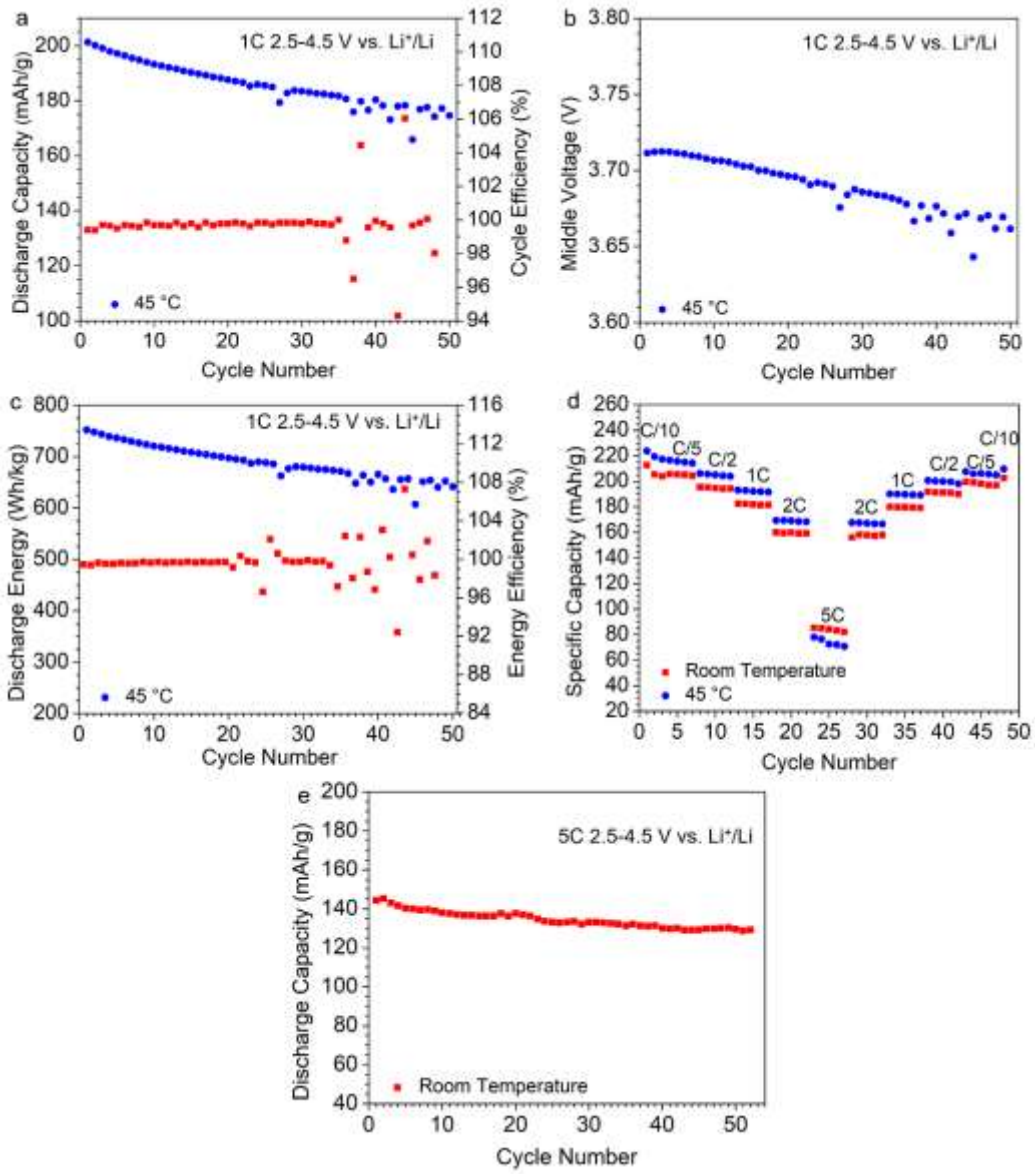

Figure A-3. Electrochemical performance of cells containing NMC 811 at 45 °C of (a) Discharge capacities and Cycle efficiencies for 50 cycles at 1C between 2.5-4.5 V vs. Li^+/Li, (b) The voltage for 50% of the discharge capacity (middle voltage) for 50 cycles at 1C, (c) specific energy and energy efficiency for 50 cycles. The specific capacity in this figure refers to specific discharge capacity, (d) Rate capability cycling of NMC811 at Room Temperature and 45 °C, and (e) discharge capacity as a function of cycle number

at 5C. Note that the cycling at 45 °C experienced performance fluctuation after 35 cycles.

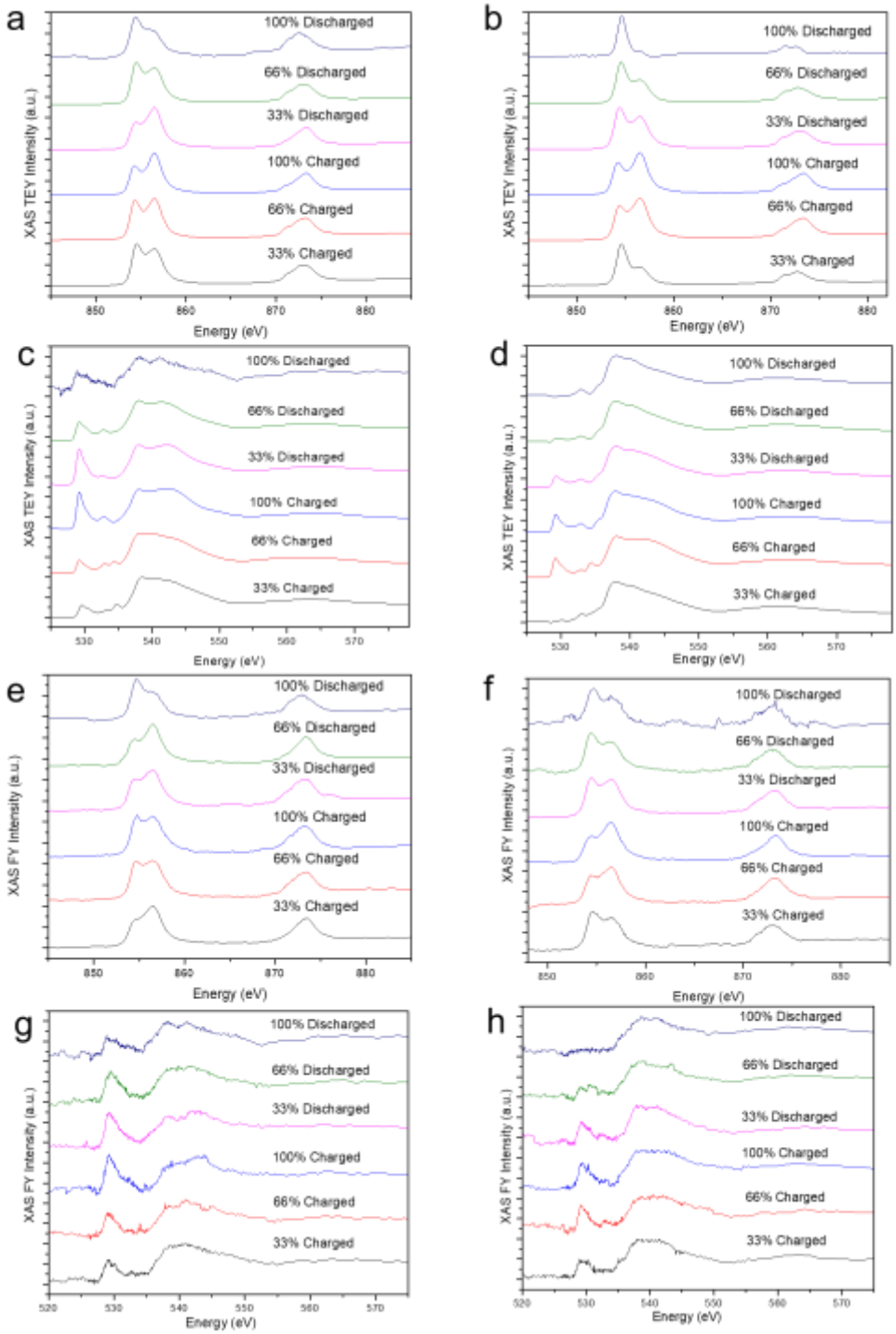

Figure A-4. Soft XAS data for (a) TEY of the Room Temperature first cycle Ni-Ledge, (b) TEY of the 45 °C Ni L-edge, (c) TEY of the Room Temperature first cycle O K-edge, (d) TEY of the 45 °C O K-edge, (e) FY of the Room Temperature first cycle Ni L-edge,

(f) FY of 45 °C Ni L-edge, (g) FY of the Room Temperature first cycle O K-edge, (h) FY of 45 °C O K-edge. We quantified our nickel XAS data by taking the two L3 edge peaks and making a ratio of the height high energy peak over the height of the low energy peak. We the graphed the ratio vs. the state of charge of the battery. For oxygen we took the area of the pre-edge peak at around 530 eV. We then graphed the areas according to the state of charge of the cell.

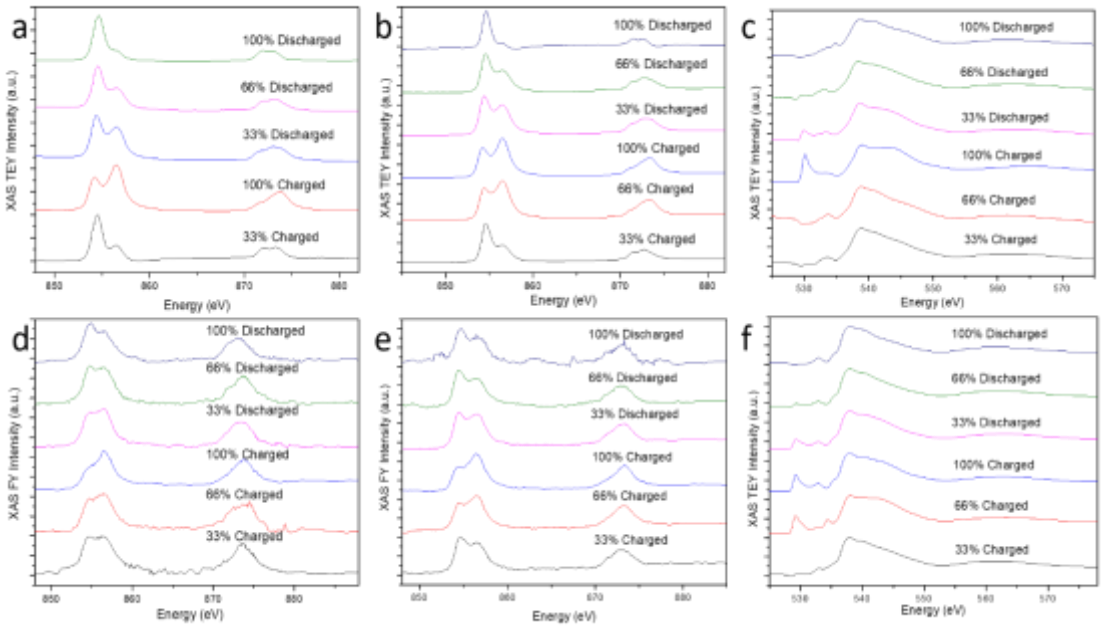

Figure A-5. Soft XAS data for (a) TEY of Room Temperature second cycle Ni L-edge, (b) TEY of the 45 °C first cycle Ni L-edge, (c) TEY of the Room Temperature second cycle O K-edge, (d) FY of the Room Temperature second cycle Ni L-edge, (e) FY of the 45 °C first cycle Ni L-edge, (f) TEY of the 45 °C first cycle O K-edge. We quantified our nickel XAS data by taking the two L3 edge peaks and making a ratio of the height high energy peak over the height of the low energy peak. We the graphed the ratio vs. the SOC of the battery. For oxygen we took the area of the pre-edge peak at around 530

eV. We then graphed the areas according to the state of charge of the cell. The XAS spectra at 45 °C are shown here again for direct comparison with those at the second cycle at room temperature.

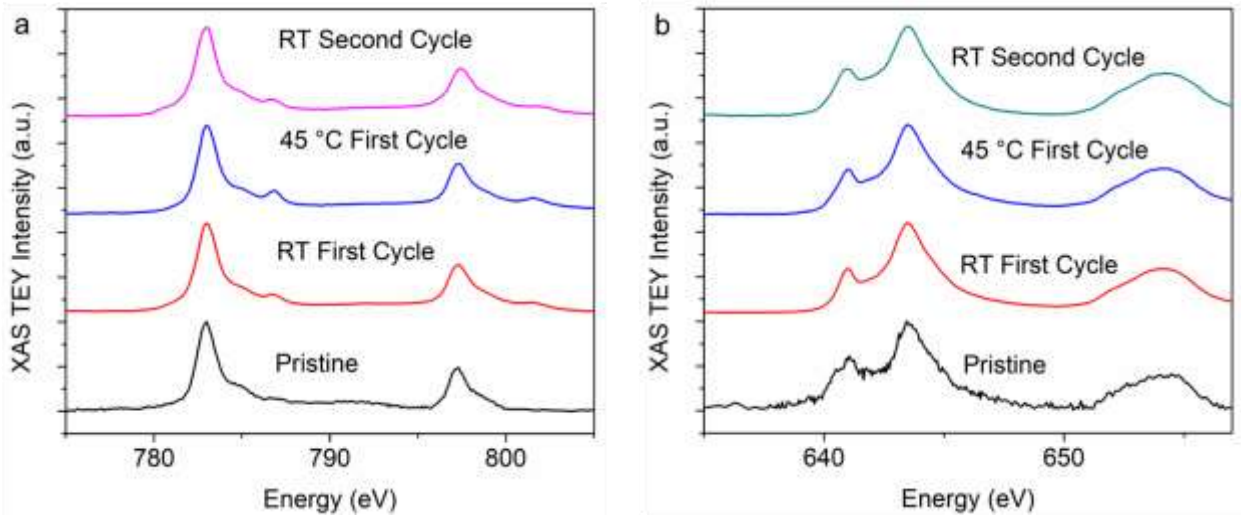

Figure A-6. Soft XAS showing the TEY data for (a) Co L-edge (b) Mn L-edge at the 100% charged state during the first cycle at RT, the first cycle at 45 ºC, and the second cycle at RT, where the pristine Co L-edge and Mn L-edge are shown for direct comparison.

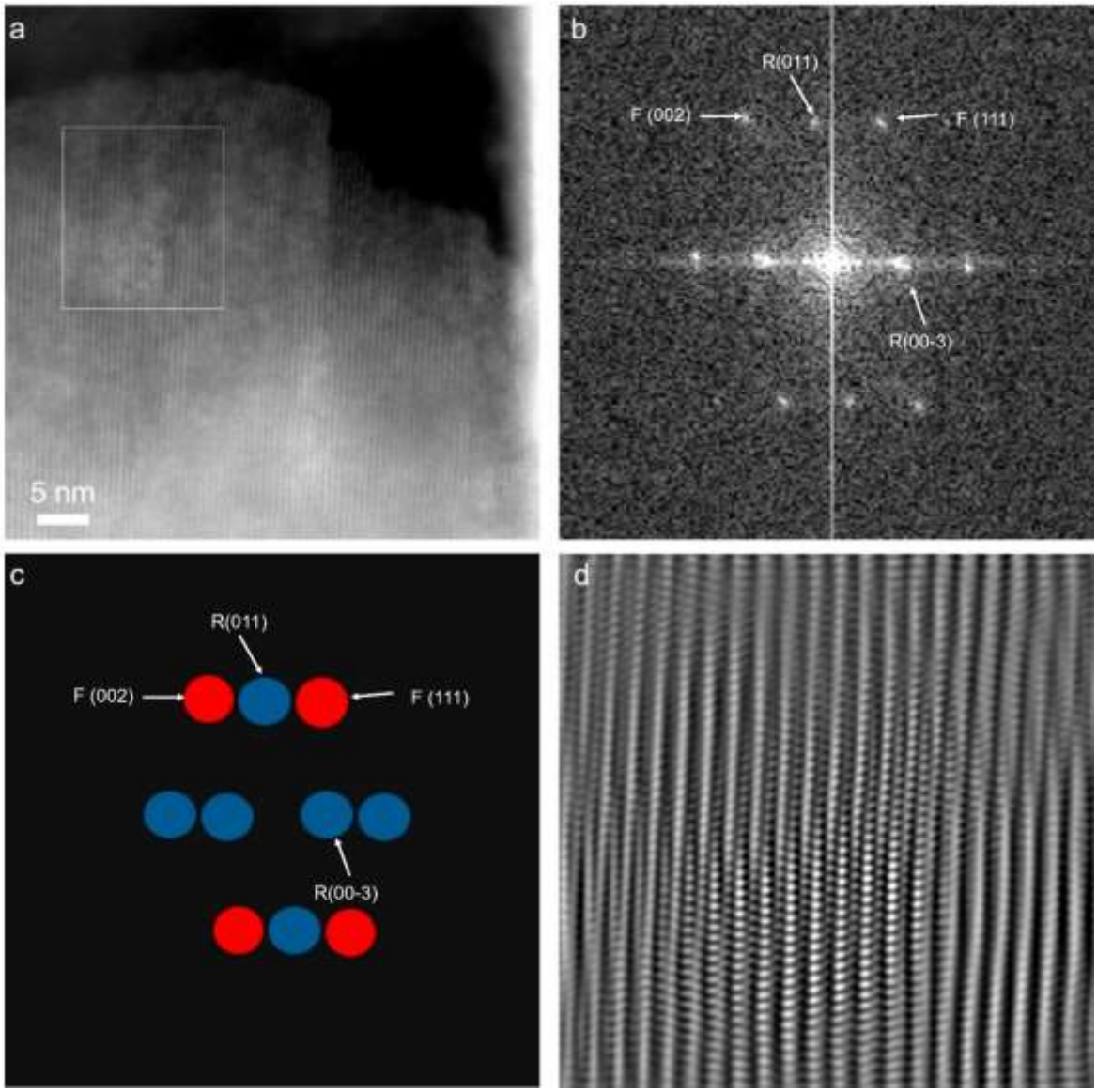

Figure A-7. (a) STEM image of a fully discharged 45 °C NMC811 particle after one cycle. (b) FFT of the indicated area of (a) indicating a mixture of a layered R$\bar{3}$m phase and a rock-salt Fm$\bar{3}$m phase. (c)Masked image of the FFT indicating the layered (blue) and rock-salt (red) phases. (d) Inverse FFT of the STEM image indicating the layered and rock-salt phases.

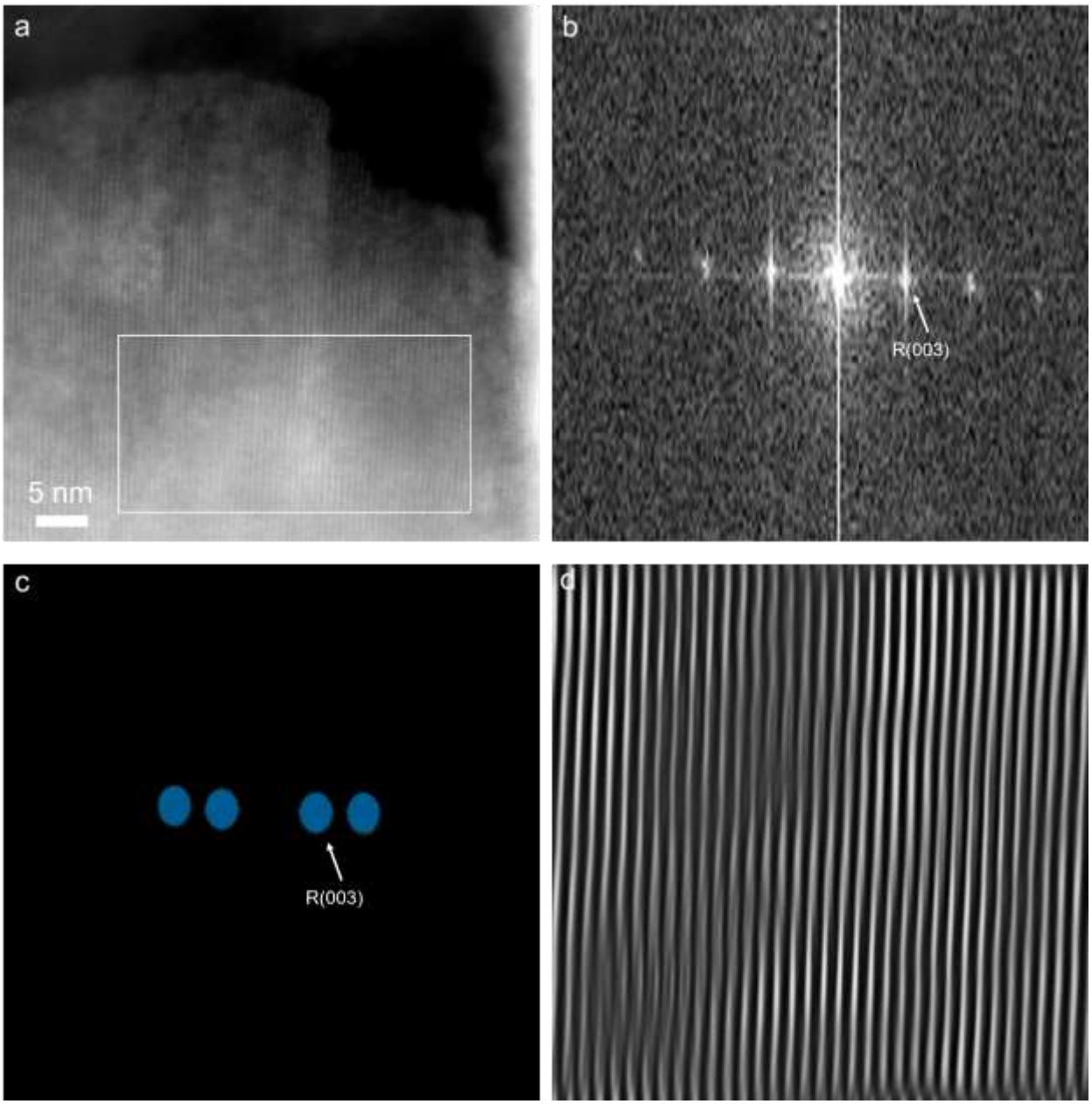

Figure A-8. (a) STEM image of a fully discharged 45 °C NMC811 particle after one cycle. (b) FFT of the indicated area of (a) indicating a mixture of a layered R$\bar{3}$m phase. (c)Masked image of the FFT indicating the layered (blue) phase. (d) Inverse FFT of the STEM image indicating the layered phase.

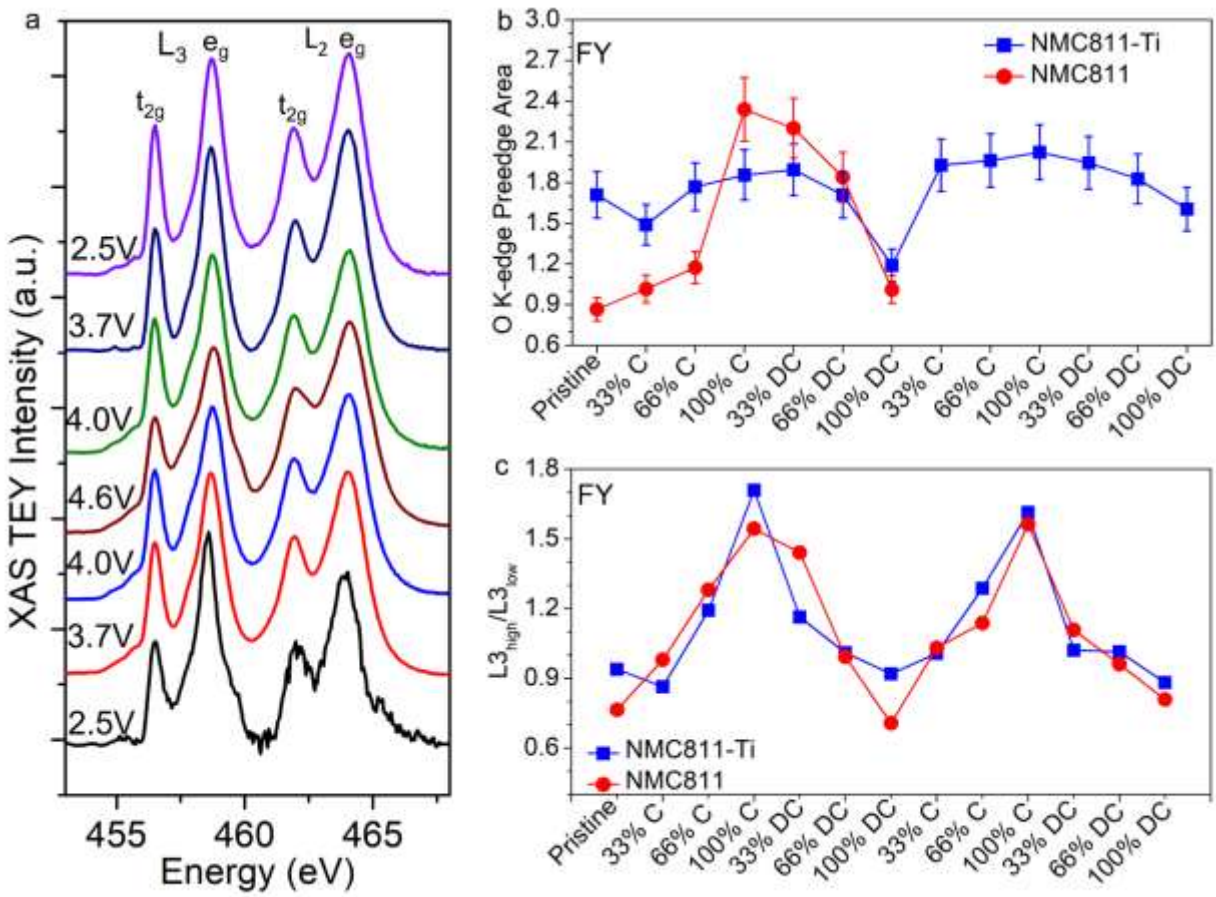

Figure A-9. a. Soft XAS TEY quantification of the first cycle of the titanium L-edge, (b) the FY of the oxygen K-edge with the integrated area of the pre-edge TM3d–O2p peak, and (c) the FY of nickel showing the ratio of the L_3 peaks.

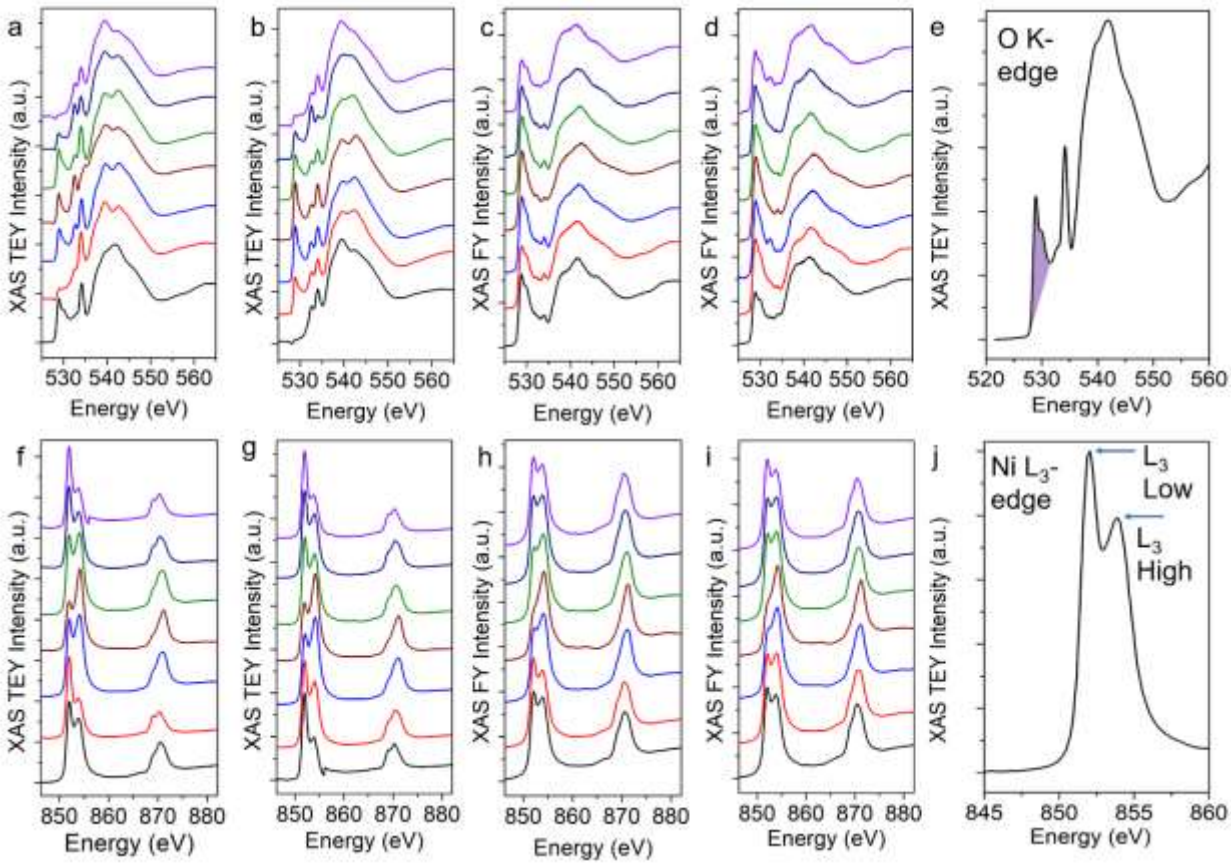

Figure A-10. Soft XAS of NMC811-Ti a. the TEY of the first cycle of the O K-edge, b. the TEY of the second cycle of the O K-edge, c. the FY of the first cycle O K-edge, d. the FY of the second cycle of the O K-edge, e. representation of quantification of the pre-edge peak of the O K-edge, f. the TEY of the first cycle of the Ni L-edge, g. the TEY of the second cycle of the Ni L-edge, h. the FY of the first cycle of the Ni L-edge, i. the FY of the second cycle of the Ni L-edge, and j. the representation of L_3 peaks used for our ratios. The first and second cycle states of charge mimic those shown in Figure 3a and S3a respectively.

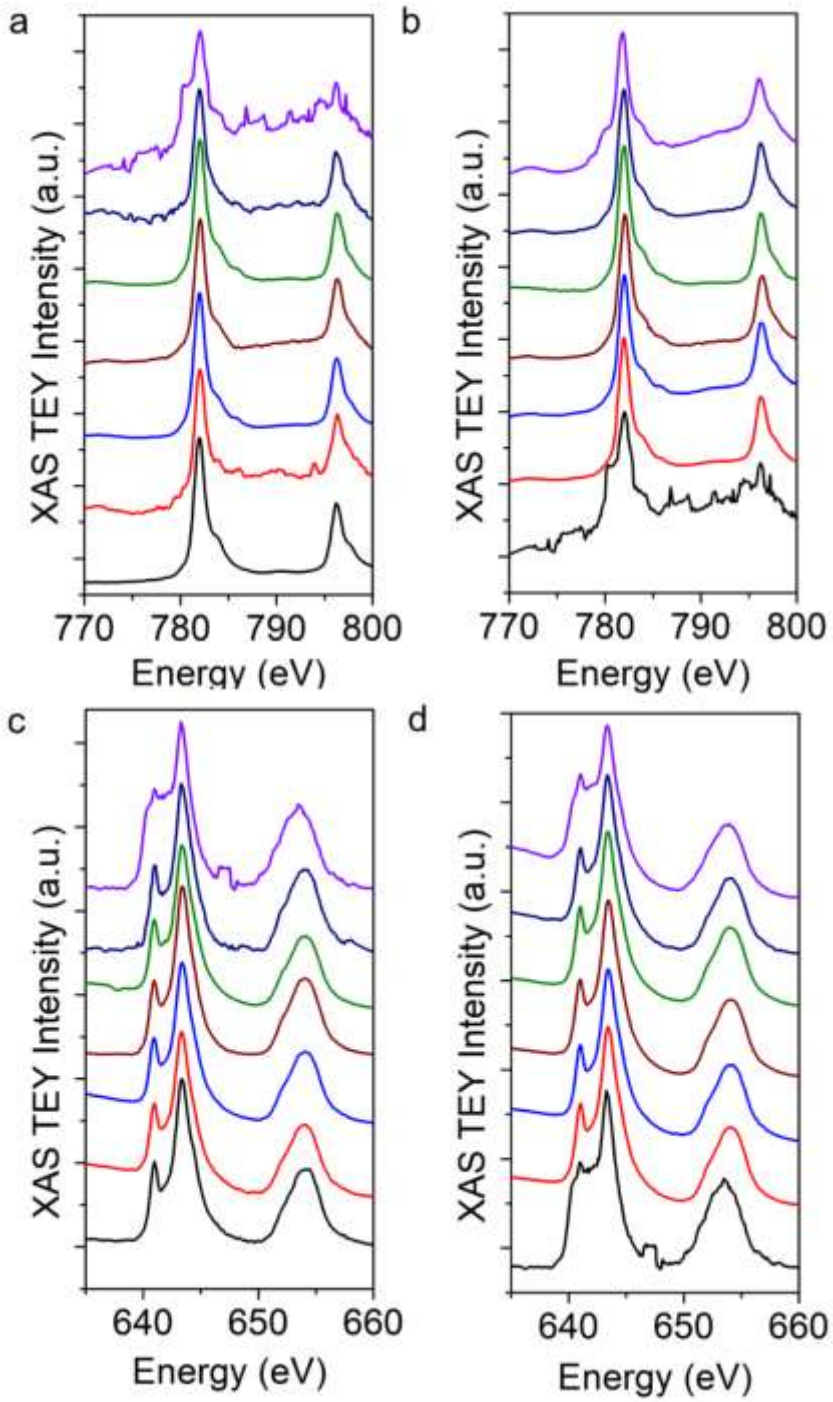

Figure A-11. The soft XAS TEY of a. the first cycle Co L-edge, b. the second cycle Co L-edge, c. the first cycle Mn L-edge, and d. the second cycle Mn L-edge. The first and second cycle states of charge mimic those shown in Figure 3a and S3a respectively.

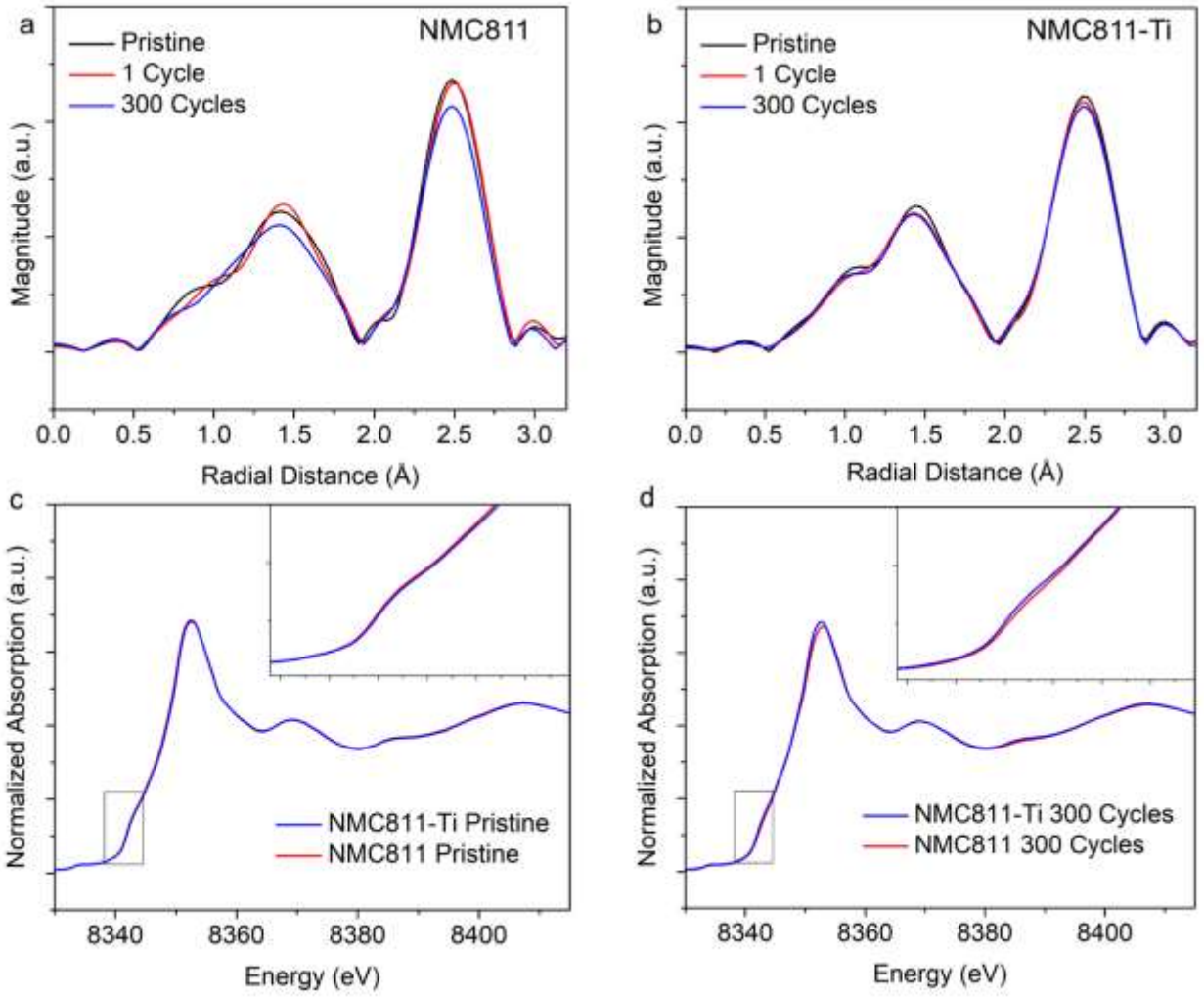

Figure A-12. a. EXAFS of nickel for NMC811, b. EXAFS of nickel for NMC811-Ti, c. XANES comparing pristine nickel, and d. XANES comparing nickel after 300 cycles.

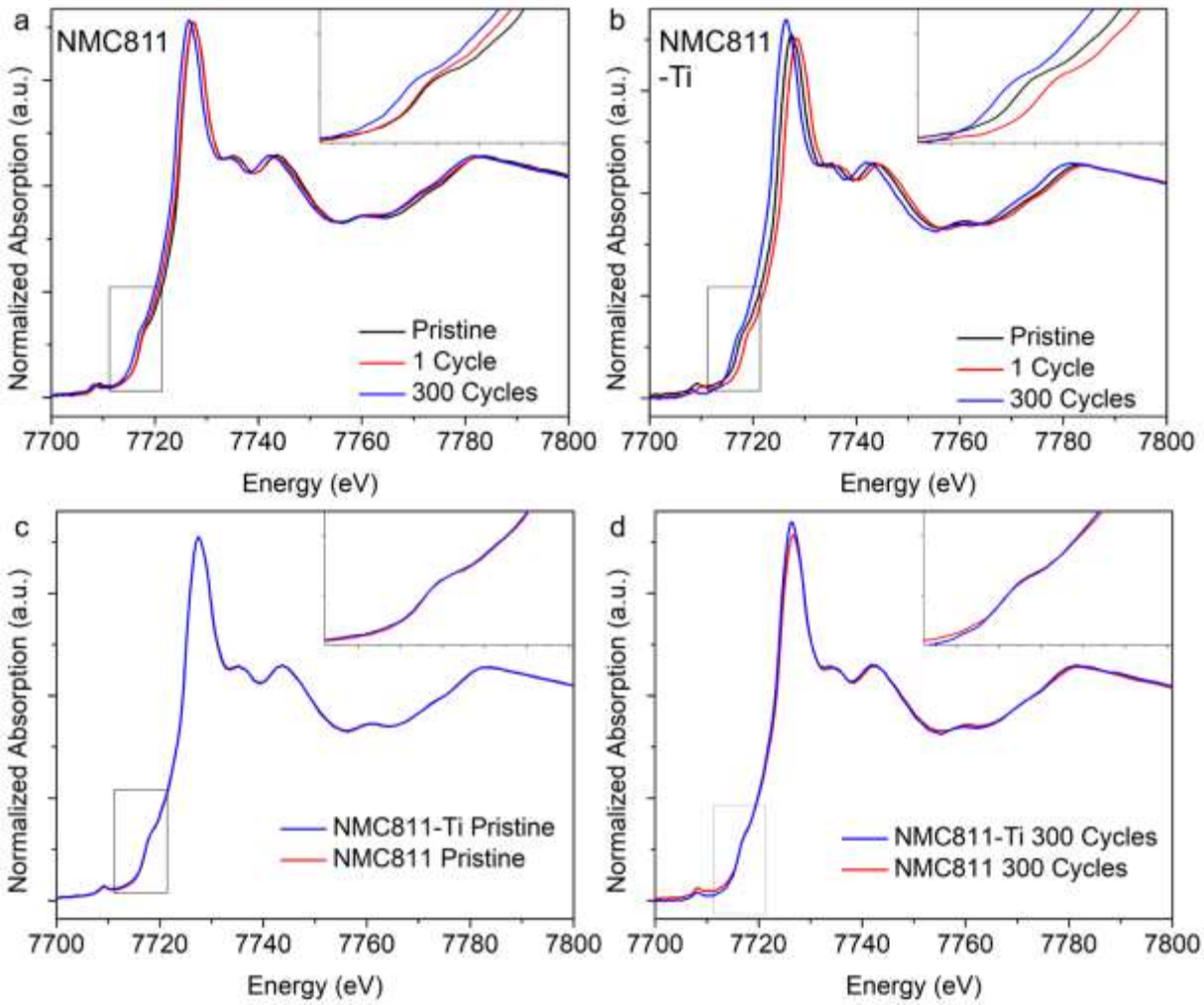

Figure A-13. XANES of cobalt for a. NMC811, b. NMC811-Ti, c. comparing the pristine state, and d. comparing after 300 cycles

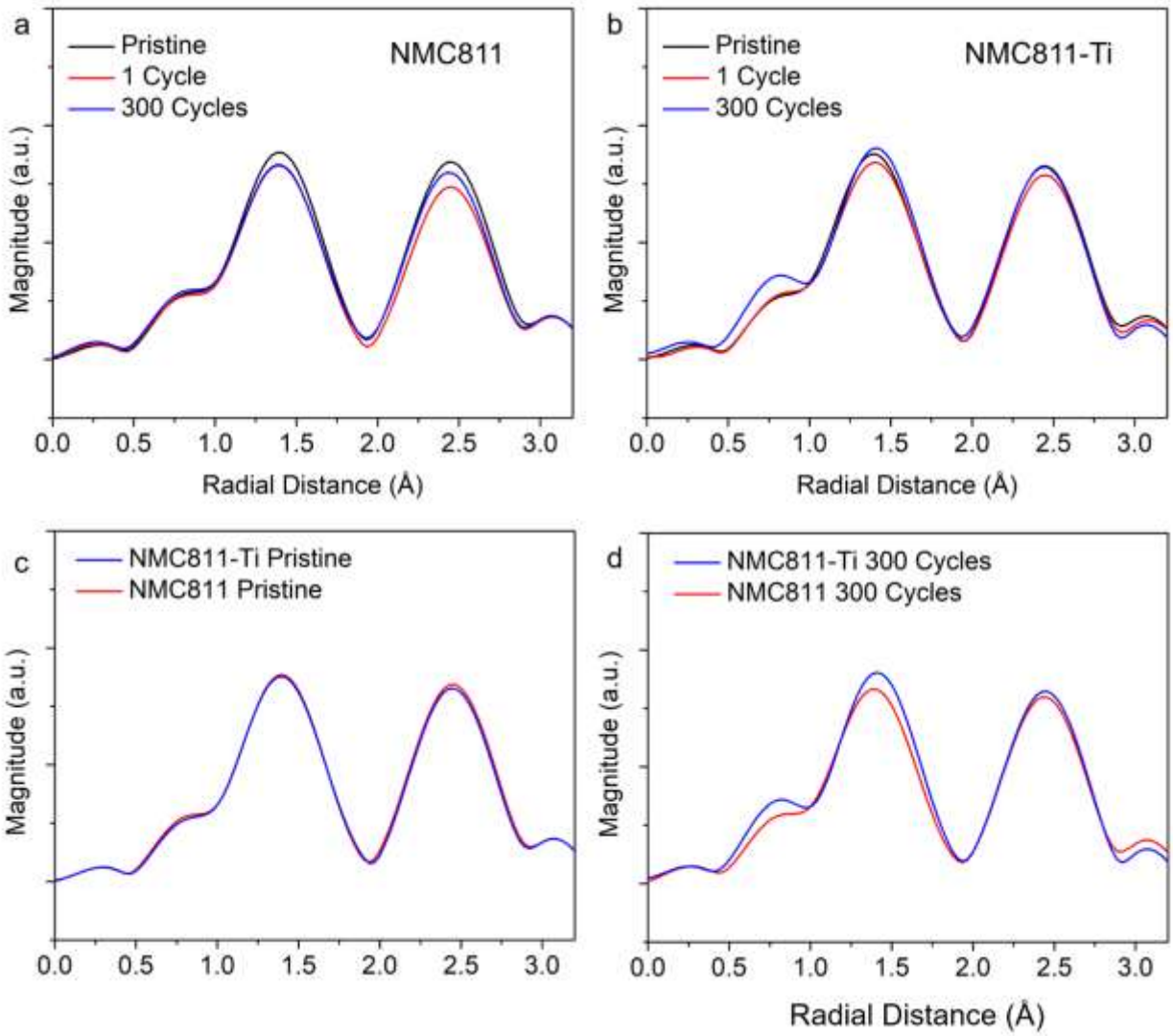

Figure A-14. EXAFS of cobalt for a. NMC811, b. NMC811-Ti, c. comparing the pristine state, and d. comparing after 300 cycles.